2018

Petrology and Geochemistry of the Tasse Mantle Xenoliths of the Canadian Cordillera: A Record of Archean to Quaternary Mantle Growth, Metasomatism, Removal, and Melting

Ali Polat
University of Windsor

Robert Frei
University of Copenhagen

Fred J. Longstaffe
The University of Western Ontario, flongsta@uwo.ca

Derek J. Thorkelson
Simon Fraser University

Eyal Friedman
Univeristy of Windsor

Petrology and geochemistry of the Tasse mantle xenoliths of the Canadian Cordillera: A record of Archean to Quaternary mantle growth, metasomatism, removal, and melting

Ali Polat[1], Robert Frei[2], Fred J. Longstaffe[3], Derek J. Thorkelson[4], and Eyal Friedman[1]

[1]Department of Earth and Environmental Sciences, University of Windsor, Windsor, ON, Canada N9B 3P4

[2]Department of Geosciences and Natural Resource Management, University of Copenhagen, Geology Section, 1350 København K, Denmark

[3]Department of Earth Sciences, The University of Western Ontario, London, ON, N6A 5B7, Canada

[4]Department of Earth Sciences, Simon Fraser University, Burnaby, BC, Canada V5A 1S6

Submitted to Tectonophysics

*Corresponding author (polat@uwindsor.ca)

ABSTRACT

Mantle xenoliths hosted by the Quaternary Tasse alkaline basalts in the Canadian Cordillera, southeastern British Columbia, are mostly spinel lherzolite originating from subcontinental lithospheric mantle. The xenoliths contain abundant feldspar veins, melt pockets and spongy clinopyroxene, recording extensive alkaline metasomatism and partial melting. Feldspar occurs as veins and interstitial crystal in melt pockets. Melt pockets occur mainly at triple junctions, along grain boundaries, and consist mainly of olivine, cpx, opx and spinel surrounded by interstitial feldspar.

The Nd, Sr and Pb isotopic compositions of the xenoliths indicate that their sources are characterized by variable mixtures of depleted MORB mantle and EM1 and EM2 mantle components. Large variations in εNd values (–8.2 to +9.6) and Nd depleted mantle model ages (T_{DM} = 66 to 3380 Ma) are consistent with multiple sources and melt extraction events, and long-term (>3300 Ma) isolation of some source regions from the convecting mantle. Samples with Archean and Paleoproterozoic Nd model ages are interpreted as either have been derived from relict Laurentian mantle pieces beneath the Cordillera or have been eroded from the root of the Laurentian craton to the east and transported to the base of the Cordilleran lithosphere by edge-driven convection currents.

The oxygen isotope compositions of the xenoliths (average $\delta^{18}O$ = +5.1±0.5‰) are similar to those of depleted mantle. The average $\delta^{18}O$ values of olivine (+5.0±0.2‰), opx (+5.9±0.6‰), cpx (+6.0±0.6‰) and spinel (+4.5±0.2‰) are similar to mantle values. Large fractionations for olivine-opx, olivine-cpx and opx-cpx pairs, however, reflect disequilibrium stemming from metasomatism and partial melting.

Whole-rock trace element, Nd, Sr, Pb and O isotope compositions of the xenoliths and host alkaline basalts indicate different mantle sources for these two suites of rocks. The xenoliths were derived from shallow lithospheric sources, whereas the alkaline basalts originated from a deeper asthenospheric mantle source.

Key words: Canadian Cordillera; mantle xenoliths; alkaline basalt; melt pocket; mantle metasomatism; lithospheric delamination; slab window

1. Introduction

Mantle xenoliths in continental alkaline volcanic rocks are the main source of information on the origin and evolution of the subcontinental lithospheric mantle (SCLM) (Menzies, 1990; Griffin et al., 2003; Carlson et al., 2005; Pearson et al., 2005; Pearson and Witting, 2008; Francis et al., 2010; Artemieva, 2011; Aulbach et al., 2017). Such xenoliths have been found in numerous locations on Earth and their petrogenesis has been extensively studied (Carlson et al., 2005; Pearson et al., 2005; Canil and Lee, 2009). These studies have provided important insights into the geodynamic and petrological processes that generated the SCLM (Wiechert et al., 1997; Bernstein et al., 1998; Abraham et al., 2001; Peslier et al., 2002; Canil, 2004; Carlson et al., 2005; Pearson and Witting, 2008; Canil and Lee, 2009; Herzberg and Rudnick, 2012; Rocco et al., 2012; Mundl et al., 2016). Petrographic and geochemical studies have shown that the sources of mantle xenoliths have commonly experienced multiple events of melt extraction, and melt- and fluid-driven metasomatism (Canil and Scarfe, 1989; Ionov et al., 1995; Kopylova and Russell, 2000; Carlson et al., 2004; Shaw et al., 2006; Simon et al., 2007; Temdjim, 2012; Martin et al., 2013; O'Reilly and Griffin, 2013; Scott et al., 2016). In addition, studies of mantle xenoliths and host alkaline volcanic rocks have provided new constraints on the mechanism of delamination of the SCLM beneath both Archean cratons and younger orogens (Gao et al., 2002; Zhu and Zheng, 2009; Xu et al., 2013; Carlson et al., 2005).

The alkaline volcanic rocks in the Canadian Cordillera contain abundant, fresh mantle xenoliths that have been the subject of numerous studies of the composition, origin and evolution of the underlying SCLM (Fujii and Scarfe, 1982; Nicholls et al. 1982; Ross, 1983; Brearley et al., 1984; Canil et al., 1987; Canil and Scarfe, 1989; Sun and Kerrich, 1995; Peslier et al., 2000, 2002; Harder and Russell, 2006; Francis et al., 2010; Greenfield et al., 2013; Friedman et al., 2016). Recent studies have made important contributions to our understanding of the composition, origin and evolution of the lithospheric mantle beneath the Canadian Cordillera (Francis et al., 2010; Hyndman, 2010; Hyndman and Currie, 2011; Morales and Tommasi, 2011; Greenfield et al., 2013; Bao et al., 2014; Gu et al., 2015). Nonetheless, several outstanding questions remain: (1) How did the SCLM form? (2) When did it form? (3) Why is it thinned or delaminated? (4) What caused metasomatism?

In this study, we present detailed Scanning Electron Microscope-Back Scattered Electron (SEM–BSE) image analyses and Scanning Electron Microscope-Energy Dispersive

Spectroscopy (SEM-EDS) major element data, and report new whole-rock Nd, Sr and Pb isotope, and whole-rock and mineral olivine, orthopyroxene (opx), clinopyroxene (cpx), and spinel O isotope data for mantle xenoliths hosted by the Tasse alkaline basalts (Tasse mantle xenoliths hereafter) in the property of mineral exploration Barkerville Ltd in southeastern British Columbia, Canada (Fig. 1) (Friedman et al., 2016). We also present new O isotope data for the host alkaline basalts. This study reports, for the first time, the presence of widespread, well-preserved metasomatic feldspar veins, frozen melt pockets and spongy and resorption textures in the mantle xenoliths of the Canadian Cordillera. The SEM analyses indicate that these textures stemmed from chemical reactions between mantle minerals and percolating low-silica alkaline melts and/or fluids. The new and existing petrographic and geochemical data are used to address the questions listed above and to revisit hypotheses previously proposed to explain the origin and delamination of the SCLM beneath the Canadian Cordillera in southeastern British Columbia. Major and trace element data for the studied samples were presented in Friedman et al. (2016).

2. Regional geology and tectonic setting

The Canadian Cordillera is one of the largest accretionary orogenic belts in the world. The geological history of the region began with the accretion of Paleoproterozoic terranes onto an evolving, Archean-cored landmass termed Laurentia (Ross, 2002). During the Late Paleoproterozoic to the Early Mesoproterozoic, northwestern Laurentia was involved in a series of compressional and extensional tectonic events including collisions with Australia, Antarctica, intervening arc terranes, and possibly South China (Ross et al., 1992; Thorkelson and Laughton, 2016; Zhao et al, 2004). Activity in the Late Mesoproterozoic to Early Neoproterozoic led to magmatism, metamorphism and isotopic resetting of the mantle in western and southern Laurentia (Peslier et al., 2000; Milidragovic et al., 2011). All of these events were broadly concurrent with Proterozoic activity in western and southern Laurentia, particularly the Paleoproterozoic Labradorian, Yavapai and Mazatzal orogenies, and the Mesoproterozoic to Neoprotoerozoic Grenville orogeny (Rivers and Corrigan, 2000; Snyder et al., 2009; Karlstrom et al., 2001). By approximately 1.0 Ga, western Laurentia was juxtaposed with Australia and other landmasses as part of the supercontinent Rodinia (Moores, 1991; Li et al., 2008).

Toward the end of the Precambrian and into the Early Paleozoic, Laurentia rifted and then drifted from its western conjugates, and western Laurentia evolved into an Atlantic-type margin

(Gabrielse et al., 1991; Cook and Erdmer, 2005) with a prominent continental slope. With the exception of an interval of arc magmatism and collision in the Devonian-Mississippian, western Laurentia remained as a mainly Atlantic-type margin until the Triassic when it began to collide with large oceanic terranes in the proto-Pacific basin (Coney et al., 1980; Monger and Price, 2002; Colpron and Nelson, 2009). Mesozoic accretion of terranes such as Quesnellia, Stikinia, Wrangellia and the Cache Creek terrane deformed the strata deposited on the Atlantic-type margin and produced the tectonic collage that characterizes the Canadian Cordillera today. Additional plates and complex evolution were recently proposed by Sigloch and Mihalynuk (2017). Major terrane accretions were complete by the Cenozoic, with the notable exception of collisions with Siletzia mostly in Washington and Oregon (Eddy et al., 2017) and the Yakutat terrane in southeast Alaska (Mazzotti and Hyndman, 2002).

During the Cenozoic, most of the Canadian Cordillera was affected by eastward subduction of oceanic plates in the Pacific basin, namely the Kula, Resurrection, and Farallon (Haeussler et al., 2003). Arc magmatism, modified by ridge subduction and slab window formation, and convective removal of lithospheric mantle, led to a broad magmatic field throughout much of the region (Madsen et al., 2006; Currie et al., 2008; Francis et al., 2010; Bao and Eaton, 2015).

The Cenozoic magmatic history of the Canadian Cordillera can be divided into two discrete intervals: the Paleocene to Oligocene, and the Miocene to Quaternary (Dostal et al., 2008). The earlier interval is characterized by mafic to felsic magmatism with predominantly arc-like (subduction-related) compositions. During this interval, the Farallon plate subducted in the southern part of the region, and the Kula/Resurrection plates subducted in the north (Haeussler et al, 2003; Kusky et al., 2003). By the Oligocene, the remnants of the Kula/Resurrection plates had either subducted or joined the Pacific plate, and the Farallon plate had been reduced to mainly the Juan de Fuca plate (Madsen et al., 2006). Most of the Cordillera experienced no magmatism during the Oligocene (Dostal et al., 2008). By the Early Miocene, subduction of the Juan de Fuca plate was restricted to southern British Columbia and the western United States, and the northern part of the Cordillera was flanked by the Pacific plate, which was moving in a northward, strike-slip manner along the Queen Charlotte fault (Fig. 1). This transition was accompanied by the formation of the Northern Cordilleran slab window, which progressively expanded and now extends from the Garibaldi (northern Cascade) arc in southern British Columbia to the Wrangell volcanic belt in the northern Cordillera (Alaska and western Yukon) (Fig. 1) (Thorkelson et al., 2011). In addition, the northern tip of the Juan de Fuca plate (called the Explorer plate), became detached in the Pliocene and is no longer subducting (Fig. 1) (Riddihough et al., 1980). The previously subducted Explorer part of the Juan de Fuca slab, as imaged tomographically by Audet et al. (2008) and Mercier et al. (2009), is tectonically stagnant (Riddihough 1980) and has undergone significant thermal erosion and physical degradation (Thorkelson et al., 2011).

The Oligocene transition from a subduction-dominated regime to a slab window-related system was followed by vigorous Miocene to Quaternary magmatism. Miocene to Quaternary volcanic rocks in British Columbia are dominated by mafic alkaline rocks, such as basalt, hawaiite and basanite, followed by trachyte in abundance (Nicholls et al., 1982; Stout and Nicholls, 1983; Souther, 1986; Edwards and Russell, 2000; Edwards et al., 2002; Kuehn et al., 2015). The volume of trachyte and peralkaline volcanic rocks reaches up to 30% in some volcanoes (e.g., Mt. Edziza; Souther, 1992). There are, however, no known examples of intermediate volcanic rocks (e.g., andesite) in the Miocene to Quaternary volcanic sequences of British Columbia. Prominent divisions of the post-Oligocene volcanic field include the Northern Cordilleran volcanic province (NCVP), the Anahim volcanic belt (VB), the Chilcotin lavas and the Wells Gray lavas (Fig. 1) (Bevier et al., 1979; Bevier, 1983; Hickson and Souther, 1984; Edwards and Russell, 2000). These volcanic fields differ significantly from the pre-Oligocene volcanic rocks in three main ways. First, the younger rocks are significantly more mafic. Second, they are more alkaline and typically display ocean-island-like trace element enrichments (such as elevated Nb). Third, they host abundant mantle xenoliths. In British Columbia, only the Garibaldi arc, and its precursor, the Pemberton volcanic belt, shows characteristic effects of subduction-metasomatism; however, the Garibaldi arc also displays a notable non-arc asthenospheric component (Mullen and Weis, 2015). As such, the post-Oligocene influence of subduction on the overall magmatic evolution of the Canadian Cordillera is modest and, at the present day, is almost nil. Accordingly, the interpreted sources for most of the Miocene to Quaternary lavas are lithospheric mantle and asthenospheric mantle (Francis et al., 2010; Thorkelson et al., 2011) rather than a subduction-modified mantle wedge. Subduction-hydrated peridotite must have occupied the mantle wedge and back-arc regions beneath much of the Canadian Cordillera prior to the Oligocene, as it was the clearly the source for the dominantly arc-type Eocene-Paleocene magmatic field (Breitsprecher et al., 2003; Ickert et al., 2009). The near-absence of a subduction-modified mantle reservoir beneath the Cordillera from Miocene onwards is consistent with displacement of the former mantle wedge by uprising anhydrous asthenosphere during slab window formation (Thorkelson et al., 2011), possibly augmented by small-cell mantle circulation (Currie and Hyndman, 2006) and Eocene detachment of lithospheric mantle (Bao et al., 2014).

The pre- and post-Oligocene magmatic divisions broadly coincide with major changes in tectonic processes in the Canadian Cordillera. During the Paleocene and Early Eocene, the Canadian Cordillera was under northwest-directed compressional stress from tractions generated by subduction (Gibson et al., 2008). This interval represents the final stage of mountain building in the Cordillera. Compression gave way to transtension in the Middle Eocene as a consequence of changing relative plate motions (Haeussler et al., 2003; Parrish et al., 1998). The transtension was manifested as a combination of dextral strike-slip faulting, pull-apart basin development and core-complex formation (Ewing, 1980; Gibson et al., 2008). By the end of the Eocene, transtensional deformation was over, the Pacific plate had taken position along much of the continental margin, and the Canadian Cordillera, except for coastal regions, fell into a state of relative stability. The Pacific plate moved slowly and evenly along the west coast, dragging orogenic float along with it, and driving the Yakutat terrane northward into southeastern Alaska (Mazzotti and Hyndman, 2002). The interior regions of the Cordillera, however, bear few signs of deformation after ca. 45 Ma (Bevier et al., 1979; Edwards and Russell, 2000). As such, the Miocene to Quaternary mafic volcanism was generated during an interval of tectonic quiescence and was produced mainly by mantle processes rather than plate-driven crustal thickening or thinning.

Our study area is located near Quesnel Lake, close to the settlement of Likely, British Columbia (Fig. 1). The mantle xenoliths in the study area were transported to the surface by feeders to the Tasse alkaline basalts (Friedman et al., 2016) at approximately 700 ka (Kuehn et al., 2015). Volcanic rocks in the study area were interpreted to be the easternmost manifestation of the hypothetical Anahim mantle plume (Souther, 1986; Kuehn et al., 2015).

The Tasse alkaline basalts were erupted onto the Kootenay terrane in southeastern British Columbia (Gabrielse and Yorath, 1991; Colpron and Nelson, 2009). The Kootenay terrane consists of metamorphosed Proterozoic to Upper Triassic sedimentary and volcanic rocks and is tectonically overlain by the Quesnellia terrane (Gabrielse and Yorath, 1991; Monger and Price, 2002; Moynihan and Pattison, 2013). The Kootenay terrane is composed mainly of high-grade

Neoproterozoic and Paleozoic sedimentary and volcanic rocks that were deposited in shallow to deep marine environments proximal to the western edge of the Laurentian craton (Gabrielse et al., 1991; Gabrielse and Yorath, 1991; Monger and Price, 2002; Monger, 2014). It is part of the Omineca belt that includes Paleoproterozoic continental crust, and accreted oceanic terranes of Late Paleozoic to Early Jurassic ages. The region also hosts Cenozoic continental volcanic and sedimentary assemblages, and Paleozoic to Eocene granites (Monger and Price, 2002).

The Kootenay terrane is flanked by accreted terranes of the Intermontane belt to the west and the Foreland belt to the east. In southern British Columbia, the Intermontane belt is mainly composed of Quesnellia, Stikinia and the Cache Creek terrane which together represent the obduction of ocean floor rocks and island arcs of Devonian to Jurassic age. These terranes were accreted in the Early Jurassic (ca. 180 Ma; Coney et al., 1980; Gibson et al., 2008). The Foreland belt is consists mainly of clastic and carbonate strata ranging from Mesoproterozoic to Early Cenozoic age with minor Paleozoic to Tertiary granitic intrusions. The rocks were folded and thrusted eastward in the Late Jurassic and Early Cenozoic, forming a classical foreland-thrust belt.

3. Main geophysical characteristics of the Canadian Cordillera

The Canadian Cordillera has been investigated using a range of geophysical methods that collectively provide a comprehensive framework for geological studies, including the origin and significance of mantle xenoliths. Information from deep seismic refraction, reflection and tomography, heat flow, electrical conductivity, magnetism and gravity have been used to characterize the crust, the lithospheric mantle and the underlying asthenosphere (Lewis et al. 1992, 2003; Clowes et al., 1995; Cook, 1995a, 1995b; Hyndman and Lewis,1999; Hammer and Clowes, 2004; Currie and Hyndman, 2006; Currie et al., 2008; Hyndman et al., 2009, 2010; Hyndman and Currie, 2011; Bao et al., 2014; Gu et al., 2015; Zaporozan et al., 2018). The crust has been interpreted, from east to west, as Paleoproterozoic craton overlain by deformed continental-margin strata and overthrust by accreted terranes. The thickness of the crust changes from approximately 40 km near the eastern limit of Cordilleran deformation (eastern extent of the Foreland belt) to approximately 33 km beneath the Intermontane belt. The thickness of the lithosphere undergoes a similar and more pronounced increase, with a change from >200 km to <70 km (Frederiksen et al., 2001, Hyndman, 2010; Bao et al., 2014). The change in thicknesses is abrupt, occurring near the Foreland/Omineca boundary and defining an abrupt effective edge to the thick Laurentian craton.

The changes in lithospheric thickness coincide with changes in heat flow and seismic velocity. Heat flow increases from 40–60 mW m^{-2} in the craton to 70–80 mW m^{-2} beneath the Omineca and Intermontane belts. Correspondingly, seismic velocities (P_n) in the underlying mantle decrease from about 8.2 km s^{-1} beneath craton to 7.8 km s^{-1} to the west. Interpreted temperatures at the base of the crust vary from 400-500 ºC beneath the craton to 800-900 ºC below the Intermontane belt (Hyndman, 2010; Harder and Russell, 2006; Greenfield et al., 2013). Mineral geothermometry for the mantle xenoliths confirm that temperatures beneath the Cordilleran interior are higher than below the adjacent craton (Fujii and Scarfe, 1982; Nicholls et al. 1982; Brearley et al., 1984; Canil et al., 1987; Peslier et al., 2002; Francis et al. 2010; Greenfield et al., 2013). Collectively, these trends reflect the presence of a hotter, thinner lithospheric mantle layer beneath the central and western Cordillera and a colder, thicker mantle root beneath the eastern Cordillera and Laurentian craton (Frederiksen et al., 2001; Van der Lee and Frederiksen, 2005; Currie and Hyndman, 2006; Zaporozan et al., 2018).

4. Sampling and field descriptions

Our samples were collected from xenoliths in the Tasse alkaline basalts (Friedman et al., 2016), which occur in six volcanic centres in the Tasse property of Barker Minerals Ltd. on the northwestern shore of Quesnel Lake, southeastern British Columbia (See Friedman et al., 2016, for GPS coordinates and locations of volcanic centres). The sizes of the xenoliths range from 1 to 25 cm. Xenolith shapes vary from angular to rounded (Fig. 2). The xenoliths are predominantly spinel lherzolite, with minor spinel-bearing dunite and pyroxenite (Fig. 2). Some xenoliths show centimetre-scale layers consisting mainly of pyroxene and spinel (Fig. 2).

In the field, samples TA-2012-8, TA-2012-10, TA-2012-18, TA-2012-44, TA-2012-45, TA-2012-48, and TA-2012-49 were classified as olivine-pyroxene-spinel dunite (see Friedman et al., 2016). On the basis of microscopic observations, these samples are reclassified as olivine-pyroxene-spinel peridotite (spinel lherzolite) because their olivine contents vary between 80 and 90% (see Tables 1–4).

5. Analytical methods

A Scanning Electron Microscope-Energy Dispersive X-ray Spectroscopy (SEM–EDS) equipped with a Back Scattered Electron (BSE) imaging unit, located at the University of Windsor, Ontario, was used to identify the minerals and obtain BSE images. We analysed more than 650 spots on olivine, cpx, opx, feldspar (feld) and spinel in 44 polished, 30 μm thick, thin sections using EDS. The method for SEM–EDS analyses is given in Price (2012).

Only a short summary of the geochemical analytical methods is given here because details were presented in our previous publications. For Sm–Nd, Pb and Sr isotope analyses, and for O isotope analyses, the reader is referred to Wu et al. (2016) and Polat and Longstaffe (2014), respectively.

5.1. Sm–Nd, Pb and Sr isotope analyses

Fifteen samples were analysed for Sm–Nd, Pb and Sr isotopic compositions using a VG Sector 54 IT Thermal Ionization Mass Spectrometer (TIMS) at the Geological Institute, University of Copenhagen, Denmark. Sample selection was designed to obtain radiogenic isotope data from the least- to most-depleted samples using a combination of chondrite-normalized REE patterns and Mg-numbers.

A spike of $^{150}Nd/^{147}Sm$ was mixed with the samples before the digestion process. Concentrated HNO_3, HCl and HF acids were used to dissolve the samples in Savillex^{TM} beakers on a hotplate at 130ºC for three days. Strontium and REE were separated using chromatographic columns charged with 12 ml AG50W-X 8 (100–200 mesh) cation resin. Neodymium and Sm were further separated using smaller chromatographic columns containing Eichrom's^{TM} LN resin SPS (Part#LN-B25-S). A standardized 3M HNO_3-H_2O elution procedure applying self-made disposable mini-extraction columns, including mesh 50–100 SrSpec™ (Eichrome Inc.) resin, was used for purification of Sr fractions. Conventional glass and miniature glass stem anion exchange columns containing 1 ml and 200 µl of 100–200 mesh Bio-Rad AG 1×8 resin, respectively, were used for separation of Pb.

Samarium and Nd isotopes were collected in a static multi-collection mode and in a multi-dynamic routine, respectively, using a triple Ta-Re-Ta filament assembly. Mass bias correction of the measured Nd isotope ratios was made using the $^{146}Nd/^{144}Nd$ ratio of 0.7219. The JNdi standard measurements yielded a mean value of $^{143}Nd/^{144}Nd = 0.512095\pm11$ (2σ; $n = 6$) during the period of analyses. Precision for $^{147}Sm/^{144}Nd$ ratios is better than 2% (2σ).

Lead isotopes were measured in a static multi-collection-mode and fractionation was controlled by repeated analysis of the NBS 981 standard (using values of Todt et al. 1993). The total procedural blank for the analyses was <200 pg Pb, which could affect the common lead isotope ratios only below the third significant digit.

Hundred ng loads of the NBS 987 Sr standard yielded $^{87}Sr/^{86}Sr = 0.710243 \pm0.000016$ (n = 7, 2σ). The $^{87}Sr/^{86}Sr$ values of the samples were corrected for the offset relative to the certified NIST SRM 987 value of 0.710250. $^{87}Rb/^{86}Sr$ ratios were calculated using Rb and Sr concentrations obtained by ICP–MS analyses.

5.2.Oxygen isotope analyses

Ten whole-rock samples and thirty mineral separates, including eight olivine, eight cpx, eight opx and six spinel separates, were analyzed for their oxygen isotope compositions. Four whole-rock alkaline basalt samples were also analysed for comparison with the mantle xenoliths. The xenolith samples were selected on the basis of their sizes and modal mineralogical compositions in order to obtain olivine, opx, cpx, and spinel separates in sufficient amounts that representative $\delta^{18}O$ values could be obtained for each mineral group. Minerals were separated at the University of Windsor. Crushed-samples were cleaned with distilled water and grains were hand-picked using a reflected binocular microscope (see Polat and Longstaffe 2014).

Samples were analysed for oxygen isotopes at the Laboratory for Stable Isotope Science, The University of Western Ontario, Canada. Approximately 8 mg of sample powder were placed into spring-loaded sample holders, evacuated overnight at ca. 150 °C, and then moved to nickel reaction vessels and heated *in vacuo* at 300 °C for further 3 hours to remove surface water (see Polat and Longstaffe 2014; Zhou et al. 2016). The samples were then reacted overnight at ca. 580 °C with ClF_3 to release silicate-bound oxygen (Borthwick and Harmon, 1982) following Clayton and Mayeda (1963). The oxygen was converted to CO_2 over red-hot graphite, followed by isotopic measurement using a Micromass Optima II dual-inlet, stable-isotope-ratio mass-spectrometer. Olivine and spinel separates were pretreated with 50 mm Hg of BrF_5 at room temperature for 12 hours, prior to liberation of oxygen using a Merchantek Mir 10-25 CO_2 laser-BrF_5 line (Sharp 1990, 1995). Oxygen was then purified using cryogenic traps and heated KCl, condensed on a liquid nitrogen-cooled 13x molecular sieve, and NF_3 removed by cryogenic separation following Clayton and Mayeda (1983) and Miller et al. (1999). The oxygen isotope measurements for the oxygen gas were obtained using a Thermo Scientific Delta V Plus mass spectrometer in dual-inlet mode.

The oxygen isotopic data are reported as δ-notation in parts per thousand (‰) relative to Vienna Standard Mean Ocean Water (VSMOW). Average reproducibility for whole-rock samples analyzed using the conventional ClF_3 method was ±0.19‰ (0.02–0.37‰, n = 2). During these analyses, laboratory standard CO_2 had $\delta^{18}O$ = +10.30±0.04‰ (1σ, n = 6; accepted, +10.30‰), laboratory standard quartz had $\delta^{18}O$ = +11.48±0.14‰ (n = 2; accepted, +11.5‰) and laboratory standard basalt had $\delta^{18}O$ = +7.44±0.26‰ (n = 2; accepted, +7.5‰). Reproducibility for duplicate analyses of olivine and spinel produced using BrF_5 and laser heating was ±0.02±0.01‰ (1σ, n = 4). The UWG-2 garnet standard had $\delta^{18}O$ = +5.75±0.08‰ (1σ, n = 4), compared to its suggested value of +5.8‰ and uncorrected value of +5.74±0.15‰ (1σ, n>1000) reported by Valley et al. (1995).

6. Petrography and BSE image analyses

The mantle xenoliths have a coarse-grained granular texture consisting of 60–90% olivine, 10–20% opx, 10–20% cpx and 3–6% spinel (Figs. 3, 4). Many samples display ~120º triple junctions at olivine-olivine-olivine and olivine-olivine-pyroxene contacts (Figs. 3a, b, c). Melt pockets are abundant in some samples (Figs. 3f, 4a, b). The olivine locally displays deformation lamellae and undulose extinction (Figs. 3d, e). The orthopyroxene is mainly enstatite, whereas the cpx is predominantly diopside (see section 7.5). A small proportion of cpx grains host exsolution lamellae of opx. Most cpx grains have a spongy texture with a distinct core-rim structure (Figs. 4c, d). The spinel grains are typically anhedral with reaction rims and a sieve texture (Fig. 4b). Many samples exhibit multiple generations of trails of melt/fluid inclusions within cpx, olivine and opx, but these inclusions also cross the grain boundaries (Figs. 3f, 4a, e, f).

SEM–EDS analyses and BSE images reveal the presence of abundant 5–40 μm thick feldspar veins and 20–900 μm long melt pockets in some samples (Figs. 5–7). Feldspar also occurs at triple junctions, between grains (intergranular), and as interstitial material in the melt pockets (Figs. 6–8). On the basis of EDS analyses, four compositional types of feldspar are recognized (see section 7.5). Type-1 is an anorthoclase feldspar consisting of an albite-orthoclase solid solution. Type 2 feldspar is plagioclase (andesine) feldspar with an albite-anorthite solid solution. Type 3 and Type 4 feldspars are variable mixtures of Type 1 and Type 2 feldspars. Type 3 feldspar is a Na- and K-rich feldspar with a minor anorthite content, whereas Type 4 feldspar is a Na- and Ca-rich feldspar with a minor orthoclase component. Some interstitial feldspar grains display a perthitic texture. EDS analyses of over 250 spots indicate that Type 1 (38%) and Type 4 (39%) feldspars are more abundant than Type 2 (9%) and Type 3 (15%) feldspars.

In spongy cpx grains, the cores are composed of homogeneous high-Al, Na-bearing diopside (Type 1 cpx), whereas the rims are characterized by an intergrowth of 70–90 % Na-free, low-Al diopside (Type 2 cpx) and 5–20% vermicular feldspar (Figs. 5d, 8, 9) (see section 7.5). The thickness of the rims varies from 5 to 150 μm. The feldspar in the rims is composed mainly (>60%) of Type 2 and Type 4 feldspars with lesser amounts of Type 1 and Type 3 feldspars. Feldspar intergrowths in the spongy texture exhibit irregular shapes, including forked, dendritic and eye-drop shapes (Figs. 8, 9). In some samples the cpx is characterized entirely by a spongy texture, without any distinct-core structure and Type 1 cpx (Figs. 8e, f). The spongy texture developed where cpx is surrounded mostly by olivine and opx (Figs 8, 9). The spongy cpx grains typically display serrated and embayed boundaries that are connected to the melt pockets and to other spongy cpx grains by intergranular feldspar (Figs. 7a, 8, 9). In rare cases, the spongy cpx and the melt pockets are connected by the feldspar veins. The spongy texture also occurs rarely at the expense of opx.

The melt pockets display irregular shapes and occur mainly at triple junctions, along grain boundaries, in the feldspar veins, and around spinel grains (Figs. 5–7). The melt pockets vary from 20 to 900 μm in length and consist mainly of anhedral to euhedral olivine (30–80%), cpx (20–50%), opx (5–10%) and spinel (1–3%) crystals enclosed by interstitial feldspar (Figs. 5–7, 9). In some melt pockets, the olivine is typically characterized by a skeletal texture (Figs. 6a, c, f, 7b–e). The relative abundance of minerals in the melt pockets varies from sample to sample and within each sample. The olivine in the melt pockets varies from euhedral to vermicular in shape and is compositionally similar to the mantle olivine in the host xenoliths. In the melt pockets, the cpx is typically composed of Type 2 cpx, and replaces olivine and interstitial feldspar (Figs. 5c, d, f, 7f, 9c, e). The amount of the interstitial feldspar in the melt pockets ranges from 20 to 60%.

The melt pockets commonly contain small semi-circular vugs constituting up to 20% of the pockets (Figs. 5d, 7f). Some vugs contain euhedral minerals growing from the wall to the center. The melt pockets have complex relationships with the neighbouring minerals, displaying serrated and embayed contacts (Figs. 6, 7).

Most samples have a sharp contact between the xenoliths and host alkaline basalt, and do not display any reaction rim (Figs. 10a, b). Some samples, however, display a 20–100 μm wide, gradational bright zone in which brightness increases from the xenolith to the basalt (Figs. 10c–f). Along this zone, a thin layer (20–50 μm) of olivine grains has grown at the xenolith wall with a chemical composition similar to those in the basalt. Olivine crystals in the host basalt are less magnesian than those in the xenoliths. In contrast, plagioclase crystals in the host basalt are more calcic than those in the melt pockets and the spongy textures of the xenoliths.

7. Results

7.1. Sm–Nd isotopes

The mantle xenoliths exhibit large variations in $^{147}Sm/^{144}Nd$ (0.1006–1.1927) and $^{143}Nd/^{144}Nd$ (0.512217–0.513132) ratios, yielding a wide range of present-day εNd (0) values (–8.2 to +9.6) and depleted mantle model ages (T_{DM} = 66 to 3377 Ma) (Table 1). In contrast, the host alkaline basalts have more restricted ranges of $^{147}Sm/^{144}Nd$ (0.1093−0.1117) and $^{143}Nd/^{144}Nd$ (0.512834−0.512922) ratios than the xenoliths, yielding homogeneous positive εNd (+3.8 to +5.5) values and younger depleted mantle model ages (T_{DM} = 338 and 474 Ma.) (Table 1).

On a $^{87}Sr/^{86}Sr$ versus $^{143}Nd/^{144}Nd$ diagram (Fig. 11a), the majority of the samples plot at the intersection of the DMM (Depleted MORB mantle), EM1 (Enriched mantle-1), EM2 (Enriched mantle-2) fields. Samples TA-2012-3 and TA-2012-1 plot in the EM1 and EM2 fields, respectively, and sample TA-2012-16, with the highest $^{87}Sr/^{86}Sr$ and lowest $^{143}Nd/^{144}Nd$ ratio, plots outside the designated fields (Fig. 11a). Most xenolith and all alkaline basalt samples also plot close to the HIMU (high-μ, with $\mu = {}^{238}U/^{204}Pb$) field (Fig. 11a) on the $^{87}Sr/^{86}Sr$ versus $^{143}Nd/^{144}Nd$ diagram. Similarly, on the $^{206}Pb/^{204}Pb$ versus $^{143}Nd/^{144}Nd$ diagram (Fig. 11b), most xenolith samples plot at the intersection of the DMM, EM1, and EM2 fields, whereas the alkaline basalts plot between the EM2 and HIMU fields, but closer to the EM2 field.

7.2. Pb isotopes

The xenoliths have lower $^{206}Pb/^{204}Pb$ (18.405–19.172 versus 19.404−19.575), $^{208}Pb/^{204}Pb$ (38.128–38.674 versus 38.994−39.139) and $^{207}Pb/^{204}Pb$ (15.495–15.659 versus 15.568−15.599) ratios than the host alkaline basalts (Table 2). The $^{207}Pb/^{204}Pb$ and $^{208}Pb/^{204}Pb$ ratios have narrower ranges than the $^{206}Pb/^{204}Pb$ ratios (Table 2). On the $^{206}Pb/^{204}Pb$ versus $^{87}Sr/^{86}Sr$ diagram (Fig. 11c), the xenoliths lie at the intersection of the DMM, EM1 and EM2 fields, whereas on the $^{206}Pb/^{204}Pb$ versus $^{208}Pb/^{204}Pb$ diagram (Fig. 11d), they plot in the DMM field trending towards the EM2 field.

7.3. Sr isotopes

The xenoliths display a wide range of $^{87}Rb/^{86}Sr$ (0.056–0.241) and $^{87}Sr/^{86}Sr$ (0.703177–0.708121) ratios (Table 3). Samples with Archean (T_{DM} = 2944–3377 Ma) and Paleoproterozoic (T_{DM} = 2075 Ma) Nd depleted mantle model ages have much higher $^{87}Sr/^{86}Sr$ (0.704522–0.708121 versus 0.703177–0.703924) ratios than samples with Neoproterozoic (574–957 Ma) and Phanerozoic (66–466 Ma) model ages. The Sr isotopic compositions of the xenoliths with Neoproterozoic and Phanerozoic Nd depleted mantle model ages are similar to those of the host alkaline basalts ($^{87}Sr/^{86}Sr$ = 0.703177–0.703924 versus 0.703346−0.703591). The alkaline basalts plot at the intersection of the DMM and EM2 and lie close to the HIMU field on the $^{87}Sr/^{86}Sr$ versus $^{143}Nd/^{144}Nd$ diagram (Fig. 11b). On the $^{206}Pb/^{204}Pb$ versus $^{87}Sr/^{86}Sr$ diagram (Fig. 11c), the alkaline basalts lie at the intersection of the DMM and EM2 fields and trend towards the HIMU field.

7.4. Oxygen isotopes

Whole-rock oxygen isotope data for the mantle xenoliths and alkaline basalts are presented in Table 4. The xenoliths have lower $\delta^{18}O$ (+4.5 to +6.0‰; average = +5.1±0.5‰; 1σ, n = 11) than the alkaline basalts ($\delta^{18}O$ = +6.0 to +6.8‰; average = +6.3±0.3‰, 1σ, n = 4).

Spinel (sp) has the lowest $\delta^{18}O$ (+4.3 to +4.7‰; average = +4.5±0.2‰; 1σ, n = 6) followed by olivine (ol) ($\delta^{18}O$ = +4.7 to +5.3‰; average = +5.0±0.2‰; 1σ, n = 8) (Table 5). For olivine, sample TA-2012-3 has the lowest $\delta^{18}O$ (+4.7‰), whereas for spinel, sample TA-2012-62 has the lowest $\delta^{18}O$ (+4.3‰). Orthopyroxene ($\delta^{18}O$ = +4.6 to +6.4‰; average = +5.9±0.6‰, 1σ, n = 8) and cpx ($\delta^{18}O$ = +5.0 to +6.8‰; average = +6.0 ± 0.6‰; 1σ, n = 8) have similar oxygen isotope compositions (Table 5). The $\Delta_{ol\text{-}sp}$ values vary from +0.25 to +0.95‰. Both $\Delta_{opx\text{-}ol}$ (+0.7 to +1.6‰, excluding sample TA-2012-19), and $\Delta_{cpx\text{-}ol}$ (+0.3 to +1.5‰) values are positive, whereas the $\Delta_{opx\text{-}cpx}$ (–1.1 to +1.3‰) values range from negative to positive.

7.5. Summary of the SEM-EDS mineral analyses

We analyzed olivine (n = 219), opx (n = 77), cpx (n = 95), spinel (n=34), and feldspar (n = 251) for major elements in 44 polished thin sections from 32 samples of the Tasse mantle xenoliths (Appendices A–E). Given that EDS has poorer detection limits and accuracy than data produced using the Electron Microprobe (EMP), mineral results reported in Appendices A–E are not considered as high-quality data. Accordingly, these data are used only for mineral identification and evaluation of the compositional variations in the analysed minerals. We note, however, that the major element compositions of the olivine, opx, cpx, and spinel in the Tasse mantle xenoliths are comparable to those reported from the Rayfield River and Big Timothy Mountain (southeastern B.C.) xenoliths that were analyzed using EMP (Greenfield et al., 2013).

On the basis of Mg-numbers, the olivine in the Tasse xenoliths can be divided into two types. Type 1 olivine includes high-magnesian (Mg-number = 88–95; average = 93) grains and occurs in all samples but sample TA2012-22 (Appendix A). Type 2 olivine is characterized by lower-magnesian values (Mg-number = 79–82; average = 81) and occurs only in sample TA2012-22 (Appendix A). Primary mantle olivine grains and olivine crystals in the melt pockets have similar compositions. The opx is mainly Al-bearing enstatite (MgO = 27.4–35.4 wt.%; FeO = 5.4–13.7 wt.%; SiO_2 = 51.6–55.8 wt.%; Al_2O_3 = 3.5–7.2 wt.%) (Appendix B). The cpx is predominantly diopside (Appendix C) but augite occurs in several samples. We report only the diopside data. Compositionally, the diopside is divided into two types. Type 1 cpx (cpx1; n = 65) represents the core of the spongy Al- and Na-bearing cpx (MgO = 13.2–18.4 wt.%; CaO = 19.9–24.0 wt.%; SiO_2 = 51.5–54.2 wt.%; Al_2O_3 = 3.7–9.7 wt.%; Na_2O = 0.8–3.4 wt.%) (Appendix C). Type 2 cpx (cpx2, n = 30) occurs in the rims of the spongy cpx and in the melt pockets, and is characterized by a Na-free, low-Al composition (MgO = 14.7–19.6 wt.%; CaO = 21.9–25.7 wt.%; SiO_2 = 49.6–55.9 wt.%; Al_2O_3 = 1.3–8.7 wt.%) (Appendix C). Spinel has variable Mg, Al, Cr and Fe concentrations (MgO = 19.9–22.5 wt.%; Al_2O_3 = 47.2–59.7 wt.%; Cr_2O_3 = 6.6–20.9 wt.%; FeO = 9.5–12.7 wt.%). On the basis of Ca, K, and Na contents, four types of feldspar are recognized in the Tasse mantle xenoliths. Type-1 feldspar (n = 95) is an anorthoclase solid solution (Na_2O = 6.3–11.5 wt.%; K_2O = 2.1–9.1 wt.%; SiO_2 = 61.8–68.7 wt.%; Al_2O_3 = 17.3–23.9 wt.%). Type 2 feldspar (n = 22) is represented by an albite-anorthite solid solution (Na_2O = 4.9–12.1 wt.%; SiO_2 = 50.2–62.0 wt.%; Al_2O_3 = 22.6–30.7 wt.%; CaO = 3.3–14.1 wt.%). Type 3 feldspar (n=37) is a Na- and K-rich feldspar with small contents of Ca (Na_2O = 9.0–10.9 wt.%; K_2O = 2.5–5.5 wt.%; SiO_2 = 61.9–64.4 wt.%; Al_2O_3 = 20.5–22.7 wt.%; CaO = 0.8–2.7 wt.%) and is characterized by K_2O>CaO and Na_2O>CaO. Type 4 feldspar is a Na- and Ca-rich feldspar with small K concentrations (Na_2O = 6.0–12.3 wt.%; CaO = 2.0–11.3; K_2O = 0.3–2.9 wt.%; SiO_2 = 52.6–63.1 wt.%; Al_2O_3 = 21.6–29.5 wt.%) and has Na_2O>K_2O and CaO>K_2O.

8. Discussion

8.1. Petrogenetic significance of the textures in the Tasse mantle xenoliths

Like mantle xenoliths from other locations in British Columbia (e.g., Littlejohn and Greenwood 1974; Greenfield et al., 2013), those from the Tasse property display both equilibrium and disequilibrium textures (Figs. 3, 4). An equilibrium texture is characterized by smooth and straight grain boundaries and triple junctions with ca. 120° angles (Figs. 3a–c), whereas a disequilibrium texture is represented by indented or serrated boundaries, reaction rims, spongy textures and vermicular intergrowths (Figs. 3–9). Veins, grain boundaries, and trails of melt likely acted as channels for the migration of melts (Figs. 4–9). As the melts percolated in the lithosphere, they resorbed the minerals at their edges (Figs. 3–9). The transmitted light microscopic observations and SEM–BSE images indicate that some samples underwent low degrees (1–3%) of partial melting in response to the infiltration of alkaline melts and/or fluids (Figs. 3–7).

Melt pockets and spongy textures in SCLM xenoliths have been reported from many locations around the world (Ionov et al. 1995, 1999, 2006; Bonadiman et al., 2005; Wiechert et al., 1997; Carpenter et al., 2002; Arai and Ishimaru, 2008; Su et al., 2011; Liu et al. 2017; Ntaflos et al., 2017; Rocco et al., 2017); however, they have only been rarely documented in mantle xenoliths of the Canadian Cordillera (Brearley et al., 1984). Studies of melt pockets, veins and spongy texture can provide significant new insights into the melting and metasomatism of the SCLM beneath the Canadian Cordillera (see Ionov et al., 1999, 2006; Wiechert et al., 1997; Shaw and Klügel, 2002; Bonadiman et al., 2005; Shaw et al., 2006; Su et al., 2011; Liu et al., 2017; Rocco et al., 2017).

8.2. Origin of the feldspar veins and mantle metasomatism

SEM–EDS analyses reveal the presence of four compositional types of feldspars (Figs. 5–9). Type 1 (anorthoclase) and Type 2 (andesine plagioclase) feldspars constitute two endmembers, and Type 3 and Type 4 feldspars are variable mixtures of Type 1 and Type 2 feldspars. Type 1 feldspar occurs mainly as veins and interstitial crystals in the melt pockets, whereas Type 2 feldspar occurs mainly as vermicular intergrowths at the rims of the spongy cpx grains (Figs. 5-9). On the basis of petrographic observations and compositional (SiO_2 = 57–69 wt.%; average (n = 96) SiO_2 = 65 wt.%) characteristics, we propose that Type 1 feldspar was generated by reactions between opx and externally-derived, low-silica alkaline melts and/or fluids through $Mg_2Si_2O_6$ + low-silica melt → Mg_2SiO_4 + SiO_2 reaction. Silica (SiO_2) released by the reaction combined with Na, K and Al in the alkaline melts to precipitate anorthoclase [$(Na,K)AlSi_3O_8$] solid solution. In contrast, as discussed in detail below, the origin of Type 2 feldspar (SiO_2 = 50–62 wt.%; average (n = 22) SiO_2 = 56 wt.%) is attributed to the melting of Type 1 cpx during formation of the spongy texture (Figs. 8, 9). The melts and fluids that precipitated Type 1 feldspar in the xenoliths may have also played a major role in the generation of the melt pockets through melting of olivine, opx, cpx and spinel, and in the metasomatism of the lithospheric mantle. The amount of melting decreases from spinel, through cpx and opx, to olivine. Following their melting, some spinel grains turned into relict islands in the core of the melt pockets (Fig. 6e).

What is the source of the low-silica, alkaline (K- and Na-rich) melts and fluids? The high silica content (SiO_2 = 65 wt.%; Appendix E) in Type 1 feldspar suggests that it could not have been derived directly from partial melting of the lithospheric mantle. Most Cenozoic alkaline volcanic rocks in the Canadian Cordillera have low SiO_2 (40–50 wt.%) contents (Francis and Ludden, 1995; Edwards and Russell, 1999; Abraham et al., 2001, 2005; Friedman et al., 2016). To the best of our knowledge, none of these volcanic rocks contain anorthoclase feldspar. Experimental studies suggest that silica-rich melts can form in the mantle through opx dissolution when a silica-undersaturated alkaline melt and mantle interact (Shaw et al., 1998). Formation of olivine through the dissolution of opx is a widespread process in the Tasse mantle xenoliths (Figs. 5d, f, 6c, e, 7a b, f, 9c, e, f), indicating that some SiO_2 was released when opx was transformed to olivine as the alkaline melt and opx interacted, leading to formation of Type 1 feldspar.

A low degree of partial melting of asthenospheric or lithospheric mantle sources results in the generation of silica-undersaturated (SiO_2 = 40–48 wt.%) volcanic rocks such as basanite, hawaiite, and alkaline basalt (Pilet et al., 2008; Gill, 2012). These melts likely interact with peridotite as they flow upward through the mantle.

Peslier et al. (2002) modeled the alkaline melt and peridotite interaction for the mantle xenoliths in the Canadian Cordillera. They showed that the major and trace element compositions of augite-bearing xenoliths can be explained by reaction between low-silica (SiO_2=45–49 wt.%) alkaline melts and peridotites. The presence of multiple generations of melt and/or fluid inclusions in the Tasse mantle xenoliths (Figs. 4e, f) is consistent with extensive melt and/or fluid-rock interaction. Microscopic observations indicate that the melts and fluids migrated mainly along veins and grain boundaries and reacted with olivine, opx, cpx and spinel to generate melt pockets (Figs. 5–9). The composition of these melts and/or fluids, however, is unknown. No hydrous minerals (e.g., amphibole and phlogopite) were encountered during SEM and transmitted light microscopy of our samples, indicating that the metasomatizing melts and fluids were mainly anhydrous.

Partial melting in mantle xenoliths from Summit Lake, British Columbia, was interpreted to have taken place during entrainment and transportation by the host alkaline lava (Brearley et al., 1984). To assess the possible role of the host alkaline basalt in the melting and metasomatism of the Tasse xenoliths, we studied the contacts between the xenoliths and host alkaline basalt (Fig. 10). Most samples do not show any chemical interaction between the xenoliths and their host alkaline basalt (Figs. 10a, b). Some samples, however, display a 20–100 μm wide, bright zone in BSE images at the contacts (Figs. 10c–f). These zones are interpreted as the product of pyrometamorphism. In addition, a thin layer of olivine grains grew on the xenolith walls as the xenoliths were incorporated into the basaltic melt (Figs. 10c–f). These olivines are compositionally different from those in the xenoliths and melt pockets but are similar to those in the basalt, suggesting derivation from the basaltic melts. BSE images indicate that the melt pockets and spongy textures in the xenoliths are overprinted by the pyrometamorphism (Figs. 10d–f). This feature implies that the alkaline metasomatism and melt formation in the xenoliths likely took place before the xenoliths were entrained by the alkaline basalts. In addition, the olivine, cpx and plagioclase that crystallized in the melt pockets of the xenoliths are compositionally different from those in the alkaline basalts, suggesting that the melt pockets and metasomatism in the xenoliths did not result from infiltration of the host alkali melts. Generation of a thin layer of melt at xenoliths-basalt contacts during their entrainment and transportation to the surface cannot be totally ruled out, but formation of the melt pockets and spongy texture in the interior of the xenoliths during that process seems unlikely. Accordingly, we propose that the alkaline melts originated in the asthenospheric mantle, infiltrated the SCLM before the xenoliths were brought up the surface, and led to metasomatism and melting of the SCLM.

SEM–EDS and BSE image analyses suggest that two stages of metasomatism took placed in the Tasse mantle xenoliths. Stage 1 is characterized by formation of feldspar veins and melt pockets in response to the alkaline melt-peridotite interaction (Figs. 5–9). Stage 2 is represented by the replacement of olivine and interstitial feldspar in the melt pockets by Type 2 cpx (Na-free, low-Al cpx) (Figs. 5d, f, 7f, 9c, e, f; Appendix C). As discussed below, we attribute the origin of Stage 2 metasomatism to dissolution of Type 1 cpx (Na-bearing, high-Al cpx) during spongy-texture formation. Calcium and Mg released during spongy-texture formation were transported to the melt pockets where they transformed the olivine crystals and interstitial feldspar to Type 2 cpx.

8.3. Significance of the melt pockets

Partial melting of the mantle is mainly inferred from volcanic rocks, melt inclusions and glasses in mantle-derived minerals and xenoliths, and experimental studies. Direct evidence of mantle melting is, however, rare. Harder and Russell (2006) reported textures showing the break-down of spinel grains that are surrounded by olivine in samples from the Northern Cordilleran Volcanic Province, British Columbia (Fig. 1). Given the similarity between textures reported by Harder and Russell (2006) and textures recorded in our samples, we think that these features from the Northern Cordilleran Volcanic Province might represent melt pockets. The presence of well-preserved melt pockets in the Tasse mantle xenoliths (Figs. 3–9) provide direct evidence for melting of the lithospheric mantle beneath the Canadian Cordillera, which opens a new window into understanding melt-mineral interactions in the mantle.

Partial melting in the Tasse mantle xenoliths occurred primarily at triple junctions and along grain boundaries. It involved melting of various proportions of spinel, cpx, opx and olivine that produced 20 to 900 μm long melt pockets with most in the range of 100–400 μm (Figs. 3–7). Mineral grains in the melt pockets are composed mainly of olivine, cpx and minor opx. Interstitial material consists typically of feldspar. The olivine grains in the melt pockets vary from 5 to 150 μm in length and contain feldspar inclusions, suggesting syn-crystallization of both minerals. The melts interacted with the mantle olivine, opx, cpx and spinel, resulting in their partial dissolution. Contacts between the melt pockets and mantle olivine commonly contain abundant resorbed olivine. In some samples the melt pockets occur as clusters and are connected by feldspar through grain boundaries or by veins. Trails of melt and/or fluid inclusions are more abundant near the melt pockets, suggesting a genetic relationship between melting of the xenoliths and percolation of the melts and fluids. The timing of the melting event, however, is unknown. The strength of the SCLM is controlled mainly by its thermal history and chemical composition, the presence of fluids, and pre-existing discontinuities (Şengör et al., 2018). The presence of melts in the lithospheric mantle can also significantly affect its strength, facilitating its removal and delamination (see Hyndman and Lewis, 1999; Hyndman, 2010; Wang et al., 2015).

8.4. Origin of the spongy cpx texture

Spongy cpx textures have been reported in SCLM xenoliths from many locations around the world (e.g., Ionov et al., 1995, 2006; Wiechert et al., 1997; Bonadiman et al., 2005; Liu et al. 2017; Rocco et al., 2013, 2017). The origin of these textures has been attributed to either metasomatic reactions (Shaw et al., 2006; Rocco et al., 2013) or decompressional partial melting (Su et al., 2011).

Spongy cpx texture is widespread in the Tasse mantle xenoliths and is characterized predominantly by a distinct core and rim structure that reflects the partial melting of the rims (Figs. 4, 8, 9). In some samples, entire grains display a spongy texture, and have lost their core structure (Figs. 8e, f). Some of the spongy cpx occur as isolated grains, whereas other grains are interconnected to each other and the neighbouring melt pockets through either intergranular feldspar or vein feldspar (Figs. 7a, 9). The feldspar in the rims displays complex, irregular morphologies including dendritic branching, and Y-, U-, V-forked and eye drop-shaped patterns (Figs. 8, 9). These features are interpreted as drainage channels that transported melts and fluids.

SEM–EDS and BSE image analyses of numerous grains indicate that the spongy cpx cores consist of Al- and Na-bearing diopside (Type 1 cpx), whereas the rims are made of an intergrowth of 80–95 % Na-free, Al-bearing diopside (Type 2 cpx) and 5–20 % vermicular feldspar (Figs. 8, 9; Appendix C). The cpx in the cores is 30–50 % more aluminous than the cpx in the rims. The feldspar in the rims is dominated by Type 2 feldspar (plagioclase). Type 1, Type 3 and Type 4 feldspars are less abundant.

The feldspars in the rims are interpreted as products of melt crystallization rather than exsolution from other minerals, because of their irregular shapes and spatial relationship with melt/fluid trails. The feldspar in the rims does not occur along a certain plane or follow a regular pattern like those observed for exsolved opx in cpx. Rather, the feldspar in the rims presents a chaotic pattern that is dendritic in appearance (Figs. 8, 9). We suggest that Type 2 feldspar (andesine plagioclase) and Type 2 cpx formed in response to partial melting of Type 1 cpx [cpx1 (Na, high-Al) → cpx2 (low-Al) + feld2 (Na, Ca)] in the core during decompression. Melts bearing Na and Al, plus Ca, were removed from cpx1 to form plagioclase (feld2), leaving behind Na-free and low-Al cpx (cpx2) (Appendices C, E).

This melting process generated 5–20% plagioclase and 80–95% Type 2 cpx. Some of these melts were drained from the spongy cpx and transported along the grain boundaries and veins to form interstitial Type 2 feldspar (plagioclase) in the melt pockets. They merged and mixed with Type 1 feldspar (anorthoclase) to form Type 3 and Type 4 feldspars (feldspars with K, Na and Ca in solid solution) (Appendix E).

The presence of K-bearing feldspar (Type 1, 3 and 4 feldspars) in the rims, however, indicates that not all feldspar types in the spongy cpx grains of the Tasse mantle xenoliths can be explained by partial melting. We propose that the K-bearing feldspar intergrowths in the rims originated from alkaline melts and and/or fluids that interacted with opx. These melts percolated along the grain boundaries and mixed with, or replaced, plagioclase melts in the rims, leading to formation of Type 1, Type 3 and Type 4 feldspars (Appendix E). We do acknowledge that formation of the spongy texture containing Type 1 feldspar solely by alkaline melt-cpx interaction cannot be totally ruled out. In summary, we conclude that the spongy texture in the Tasse mantle xenoliths has a complex origin, including partial melting that gave rise to Type 2 cpx and Type 2 feldspar, and to mixing between melts of Type 1 and Type 2 feldspars.

8.5. Origin and modification of the lithospheric mantle beneath the Canadian Cordillera

A large section of the SCLM of the Canadian Cordillera likely formed in the Paleoproterozoic at approximately the same time as the cratonal crust in the region (largely 1.8-2.0 Ga; Hoffman, 1989; Ross, 2002). Since then, the SCLM underwent a series of changes involving thickness, temperature and composition. Some of these changes may be attributed to Paleoproterozoic to Early Paleozoic tectonic events including mantle delamination, rifting, continental separation, magmatism, and orogenesis (Ross, 2002; Cook et al., 2005; Furlanetto et al., 2016). Late Mesoproterozoic osmium isotope model ages from mantle xenoliths underscore the likelihood of Proterozoic modification of the SCLM (Peslier et al., 2000). Mid-Paleozoic rifting and Mesozoic terrane accretion (Colpron and Nelson, 2009) may also have affected the SCLM. During the Early Cenozoic, additional terrane accretions and orogenic shortening were followed by widespread extension, dextral translation and abundant arc magmatism (Ewing, 1980; Armstrong and Ward, 1991; Monger and Price 1992; Gibson et al., 2008; Eddy et al., 2017; Sigloch and Mihalynuk, 2013, 2017). For much of the Mesozoic and Early Cenozoic, eastward subduction, as inferred from widespread arc magmatism, occurred beneath the evolving Canadian Cordillera. In the Late Cenozoic, ocean plate subduction was progressively replaced by ridge subduction and slab window formation (Thorkelson and Taylor, 1989; Madsen et al., 2006). Accordingly, arc magmatism in western Canada is now limited to the northern end of the Cascade (Garibaldi) belt (Fig. 1). Cenozoic processes that may have affected the SCLM include mantle delamination or convective dripping (Houseman and Molnar, 1997; Bao et al., 2014) and thermal erosion from asthenospheric upwelling (Gough, 1984; Thorkelson et al., 2011; Hyndman and Currie, 2011; Hardebol et al., 2012).

The presence of pargasitic amphibole and phlogopite in some mantle xenoliths (Brearley and Scarfe, 1984; Canil and Scarfe, 1989) suggests that subduction zone processes likely played an important role in the formation of the lithospheric mantle beneath the Canadian Cordillera. Similarly, the depletion of some xenoliths in HFSE (high field strength elements) is consistent with the involvement of subduction zone processes (Peslier et al., 2002; Friedman et al., 2016). The isotopic data collected in our study provide further constraints on the history of past subduction and SCLM modification.

8.5.1. Constraints from Nd–Sr–Pb isotopes

The mineralogical and major element compositions of the Tasse mantle xenoliths are similar to those reported from other locations in the Canadian Cordillera, consisting predominantly of spinel lherzolite with minor dunite and pyroxenite (Appendices A-E; Francis et al., 2010; Greenwood et al., 2013, and references therein). The absence of hydrous minerals (e.g., amphibole, phlogopite) in our samples is consistent with a relatively dry source(s). On the other hand, the trace element systematics of the Tasse mantle xenoliths are consistent with formation within, or modification above, a sub-arc mantle wedge above a subduction zone (Figs. 13, 14) (Friedman et al., 2016) and might, therefore, be expected to be hydrous. Depletion of HFSE in mantle xenoliths collected from other parts of the Cordillera has also been attributed to subduction zone processes (Peslier et al., 2002). Interaction with alkaline melts cannot explain the trace element composition of the xenoliths because neither the Tasse alkaline basalts nor alkaline volcanic rocks in other parts of the Canadian Cordillera (Francis and Ludden, 1995; Edwards and Russell, 2000; Kuehn et al., 2015) are particularly depleted in HFSE (Nb, Zr, and Ti) (Fig. 14b). Therefore, the subduction zone signatures in the Cordilleran mantle xenoliths must have been acquired prior to Late Cenozoic magmatism and, in particular, the alkaline metasomatism documented in this study.

The whole-rock Sm–Nd isotope data for the Tasse mantle xenoliths yield Mesozoic to Paleoarchean model ages (66 to 3377 Ma) (Table 1). The Sm–Nd isotopic compositions of cpx separates from the West Kettle River mantle xenolith locality near Kelowna, British Columbia, yielded Proterozoic to Eoarchean (1390–3630 Ma) model ages (Xue et al., 1990). These Nd model ages imply that depletion of the mantle beneath the Canadian Cordillera, at least for some parts, began as early as 3600 Ma and record a long geologic history. Samples with large positive εNd (+4.4 to +9.6) values (Table 1) were derived from mantle source(s) that underwent long-term, extensive partial melting (>15%), resulting in depletion of incompatible elements including Rb, Ba, Th, U, K, Nb, Ta, LREE, Pb, Sr, Zr, and Ti. The trace element patterns of these samples (Figs. 13, 14a), however, indicate that incompatible element depletion event was followed by the enrichment of these samples in Rb, Ba, Th, U, K, LREE, Pb, and Sr, relative to Nb, Ta and Ti, consistent with subduction zone metasomatic processes. Samples (e.g., TA2012-1, TA2012-16) with small positive (+0.9) and large negative (–6.7 to –8.2) εNd values and Archean depleted mantle model ages (2900-3380 Ma) are consistent with isolation of some parts of the mantle source from the convecting asthenosphere since the Paleoarchean (Table 1). Enrichment of Rb, Ba, Th, U, K, LREE, Pb, and Sr, relative to Nb, Ta and Ti, in these samples (Fig. 13; Friedman et al., 2016) is also consistent with subduction zone metasomatic enrichment processes.

The large variations in the Nd, Pb and Sr isotopic compositions thus imply heterogeneous sources for the xenoliths beneath the Cordillera. The origin of these variations can be attributed to one or more of the following geological processes: (1) multiple melt extraction events in the Archean, Proterozoic and Phanerozoic; (2) resetting of the Sm–Nd, Th–U–Pb and Rb–Sr isotope systems during tectonothermal events that affected western Canada in the Proterozoic and Phanerozoic; (3) metasomatism of the depleted mantle (DM) by fluids and melts that were partly derived from subducted terrigenous sediments; and (4) mixing of DM, and EM1 and EM2 mantle reservoirs (Fig. 11). Samples with Proterozoic and Phanerozoic Nd model ages might have resulted from reworking of the Proterozoic mantle beneath the Cordillera during tectonothermal events. Samples TA-2012-1 and TA-2012-16 have Archean Nd model ages and also have higher $^{87}Sr/^{86}Sr$ (0.706237–0.708121 versus 0.703177–0.704522) ratios than the samples with Proterozoic and Phanerozoic model ages, suggesting that the former samples were derived from the Archean lithosphere underlying the Laurentian craton. Distinction between samples with Archean and post-Archean model ages, however, is not apparent in the Pb isotope ratios (Fig. 11; Table 2). On the basis of Nd and Sr isotopic compositions, we speculate the following two scenarios: (1) these samples originated from relict fragments of Archean lithospheric mantle beneath the Cordillera; and (2) the pieces of Archean xenoliths were plucked off from the lithosphere beneath the Laurentian craton to the east by vigorous edge-driven convection currents (Hyndman et al. 2009; Hardebol et al., 2012) and transported laterally to the west beneath the Cordillera (Fig. 15).

In summary, on the basis of trace element patterns (Figs. 13, 14) and Nd and Sr isotope data (Tables 1, 3), we argue that the SCLM beneath the Canadian Cordillera was generated at a convergent plate margin(s) since the Paleoarchean (cf., Canil, 2004; Carlson et al., 2005; Simon et al., 2007; Pearson and Witting, 2008; Young and Lee, 2009; Francis et al., 2010) and has been reworked by Proterozoic and Phanerozoic tectonothermal events. The mantle xenoliths and host alkaline basalts have different Nd, Sr, Pb and O isotope compositions (Tables 1–4), implying that the basalts were not derived from partial melting of the SCLM from which the xenoliths originated (see also Nicholls et al.,1982; Sun et al., 1991; Edwards and Russell, 2000).

8.5.2. Constraints from O isotopes

In contrast to the Nd, Sr and Pb isotopic compositions, the Tasse mantle xenoliths have a narrow variation in whole-rock O isotope compositions (δ^{18}O = +4.5 to +6.0‰; average = +5.1±0.5‰), which is similar to that of the depleted mantle (δ^{18}O = +5.5±0.5‰; see Ito et al., 1987; Mattey et al., 1994; Eiler 2001). This contrasts with the significantly higher values of the alkaline basalts (δ^{18}O = +6.0 to +6.8‰; average = +6.3±0.3‰). As predicted from theoretical studies (see Zheng et al., 1998; Eiler 2001), the δ^{18}O values in the Tasse mantle xenoliths decrease from pyroxene, through olivine, to spinel (Table 5). Olivine (ol), opx, cpx and spinel (sp) δ^{18}O values in our samples are close to their magmatic values and well in the range of those reported for SCLM xenoliths from other parts of the world (Kyser et al., 1981; Mattey et al., 1994; Viljoen et al., 1996; Chazot et al., 1997; Wiechert et al., 1997; Hao et al., 2015), suggesting a relatively homogeneous O isotopic composition for the SCLM. The variation in the δ^{18}O values of cpx is slightly higher than for opx, probably resulting from formation of the spongy texture in the samples.

Although the ol, cpx and opx δ^{18}O values in the Tasse mantle xenoliths lie within the range of those known for other mantle peridotites, the oxygen isotope separation between mineral pairs (Δ_{opx-ol}, Δ_{cpx-ol}, $\Delta_{opx-cpx}$) vary greatly. The oxygen isotope fractionation between olivine and spinel (Δ_{ol-sp} = +0.3 to +1.0‰) is close to the expected range for a magmatic system (Kyser et al., 1981). For $\Delta_{opx-cpx}$ under lithospheric mantle temperatures, by comparison, no large positive or negative fractionation is expected (Kyser et al., 1981; Chiba et al., 1989; Perkins et al., 2006). Assuming equilibrium, sample TA-2012-48, which has the smallest $\Delta_{opx-cpx}$ (0.04‰) value, yields a temperature of 1148°C using the Kyser et al. (1981) opx-cpx geothermometer. A generally larger range of $\Delta_{opx-cpx}$ values (–0.8 to +1.3‰), however, is attributed to formation of the spongy cpx through melting and alkaline metasomatism (see Perkins et al., 2006; Hao et al., 2015). Similarly, variably large values for Δ_{opx-ol} (–0.4 to +1.6‰) and Δ_{cpx-ol} (+0.3 to +1.5‰) pairs likely also resulted from partial melting and alkaline metasomatism (Fig. 12). In general, most samples plot farther away from the oxygen isotope mineral-pair equilibrium lines for mantle xenoliths (Fig. 12), consistent with disturbance of the oxygen isotope system in the Tasse mantle xenoliths. Collectively, the large variation in oxygen isotope separations between mineral pairs containing opx and/or cpx likely reflects disequilibrium arising from perturbation during partial melting and alkaline metasomatism (see Hao et al., 2015).

The higher $\delta^{18}O$ (+6.0 to +6.8‰) values in the alkaline basalts, as opposed to mantle-like values (+5.5±0.5‰), might have resulted from the following processes: (1) post-magmatic alteration; (2) crustal contamination; (3) mantle metasomatism; and (4) olivine fractionation. Field and petrographic observations do not reveal any evidence for alteration in the Tasse alkaline basalts (Friedman et al., 2016), indicating that the higher $\delta^{18}O$ values are unlikely to have been resulted from post-magmatic alteration. The presence of rare quartz and gneissic xenoliths in the alkaline basalts are consistent with crustal assimilation during their ascent to the surface. However, low SiO_2 (44.2−46.0 wt.%) contents, the absence of negative Nb (Nb/Nb*=1.0−1.2) and Eu (Eu/Eu*=1.0−1.1) anomalies, the absence of positive Pb anomalies (Pb/Pb*=0.9−1.0), large positive εNd (+3.8 to +5.5) values, and depleted mantle-like $^{87}Sr/^{86}Sr$ (0.703346−0.703591) ratios are collectively inconsistent with extensive crustal contamination (Friedman et al., 2016). Thus, crustal contamination alone cannot explain the higher $\delta^{18}O$ values in the alkaline basalts. Although the effect of mantle metasomatism on the oxygen isotope composition of the alkaline basalts cannot be ruled out, we cannot assess this effect in the absence of oxygen isotope data for the possible metasomatic agents (melts, fluids). Large variations in Mg-numbers (47−59), MgO (6.5−10.2 wt.%), Ni (120−320 ppm), and Cr (160−410 ppm) contents, and the presence of olivine phenocrysts (5–10%) in the alkaline lavas are consistent with olivine fractionation, suggesting that the higher $\delta^{18}O$ values in the alkaline basalts likely stemmed from olivine fractionation, or from a combination of olivine fractionation, crustal contamination and mantle metasomatism.

8.6. Cenozoic magmatism, tectonics and the evolution of the lithospheric mantle

The lithospheric mantle of the Canadian Cordillera can be divided into two general domains, one in the west and other in the east. The western mantle domain underlies the most westerly of the accreted terranes, mainly beneath the Coast and Insular belts (Fig. 15). It formed mainly in the Paleozoic and Mesozoic during growth of Cordilleran terranes in ocean floor and island arc environments prior to collision with Laurentia in the Mesozoic (Monger and Price 2002; Colpron and Nelson, 2009). The eastern domain consists of the SCLM of Laurentia which initially grew as the mantle substrate to Paleoproterzoic terranes of the western Laurentian craton, including the Nahanni, Fort Nelson, Nova, Wabamun and Hearne blocks of Hoffman (1989) and Ross (2002). The Laurentian crust and its SCLM are thought to thin westward, terminating along a feather edge near the Intermontane/Coast belt boundary. Westward tapering of the Laurentian lithosphere is likely due to break-up of the supercontinent Nuna (also called Columbia) in the Paleoprotoerozoic (Cook et al., 2005; Furlanetto et al., 2016), and dismemberment of the supercontinent Rodinia during the late Neoproterozoic to early Paleozoic (Moores, 1991; Ross et al., 1992; Li et al., 2008). Cordilleran terranes of the Omineca and Intermontane belts, such as the Slide Mountain terrane, Quesnellia and Stikinia, were largely stripped off their lithospheric mantle as they were obducted over the Laurentian margin in the Mesozoic (Cook et al., 1992).

By the end of the Paleocene, the Laurentian SCLM of the Canadian Cordillera had experienced at least two events of rift-generated thinning plus a range of other disturbances including Paleoproterozoic lithospheric delamination (Ross, 2002), a poorly understood but widespread late Mesoproterozoic event (Peslier et al., 2000), collision with oceanic terranes in the Jurassic, and arc magmatism in the Cretaceous (Armstrong and Ward, 1991). In the Eocene, the SCLM was subjected to widespread lithospheric extension, dextral translation and magmatism of mainly arc character (Ewing, 1980; Breitsprecher et al., 2003; Gibson et al., 2008), although derivation from melting of the SCLM has been demonstrated for some Eocene lavas in southern British Columbia (Dostal et al. 2003). During this interval, the SCLM was probably thinned further, and may have been torn during large-magnitude strike-slip faulting (Abraham et al., 2001). In southern British Columbia, seismic tomography of the upper mantle is consistent with delamination of part of the SCLM during the Eocene (Bao et al., 2014). By the Late Eocene, lithospheric conditions had stabilized, and magmatic activity above the Laurentian-floored part of the orogen was not renewed until the early Miocene (Dostal et al., 2008).

In the Miocene, volcanic activity flared up and mafic lavas began to be erupted in the interior parts of the Canadian Cordillera. The volcanism continued until the Late Quaternary (including eruption of the Tasse alkaline basalts) and the region remains potentially active. The resulting volcanoes and lava fields (Fig. 1) have intraplate geochemical compositions with Nb/La ratios typically greater than 1 (Thorkelson et al., 2011), and were sourced from both lithospheric and asthenospheric mantle (Francis et al., 2010). As such, this Late Cenozoic flare-up represents a pronounced compositional shift away from the subduction-dominated magmatism of the Eocene. The Late Cenozoic intraplate field is largely contemporaneous with the still-active Garibaldi arc in the southwestern corner of British Columbia (Mullen and Weis, 2015).

The intraplate field has been divided into four main volcanic belts, namely the Chilcotin Group, the Anahim belt, the Wells Gray volcanic field and the Northern Cordilleran Volcanic Province (Fig. 1) (Bevier et al., 1979; Souther, 1986; Hickson and Souther, 1984; Edwards and Russell, 2000). Each of these belts has been rationalized on the basis of distinct processes including back-arc circulation for the Chilcotin Group (Hyndman et al., 2005); a mantle hotspot track for the Anahim (Souther, 1986; Kuehn et al., 2015) and lithospheric extension for the Northern Cordilleran Volcanic Province (Edwards and Russell, 2000). The Tasse volcanics were erupted near the projected eastern end of the purported hotspot track. However, as noted earlier, a hotspot track origin for the Anahim belt remains uncertain, and if a mantle plume is indeed present, it must be small. Extension as a principal cause of volcanism is also questionable because there is a paucity of contemporaneous extensional structures in the Cordilleran interior (Bevier et al., 1979; Edwards and Russell, 2000). Back-arc circulation is an accepted mechanism and may be applicable to southern British Columbia, but not the rest of the intraplate field, where there is no commensurate arc, nor a subduction zone. Westward motion of North America over the subducting East Pacific Rise (Dickinson and Snyder, 1979) and associated widespread mantle upwelling beneath the Cordillera (Dixon and Farrar, 1980; Gough, 1984) and through the Northern Cordilleran slab window (Thorkelson and Taylor, 1989), is applicable to all of the volcanic belts. Craton edge-driven mantle flow and lithospheric delamination has been applied to the Eocene (Bao et al., 2014) and may also be relevant to the eastern parts of the Miocene to Recent field.

In all of the foregoing hypotheses, asthenospheric upwelling plays a critical role in magma genesis. Regardless of the cause, upwelling asthenosphere will tend to undergo partial melting, particularly where the lithospheric mantle is thin and adiabatic decompression to shallow depths is possible (Mckenzie and Bickle, 1988; White and Mckenzie, 1989). In response, the lithospheric mantle will receive significant advective heat from upflowing asthenosphere and rising mafic melts, and may undergo a range of responses (Fig. 15) from gradual thermal erosion and partial melting (Francis et al., 2010; Thorkelson et al., 2011) to mantle dripping (cf., Houseman and Molnar, 1997; Jones et al., 2014), and intact-layer delamination and foundering (Bao at el., 2014; Fig. 15).

Asthenospheric upwelling is likely to have caused significant thinning of the SCLM during the Cenozoic, with notable pulses in the Middle Eocene and from the Miocene to the present.

How thick the SCLM was at the onset of the Cenozoic is unknown, but considering the abundance of tectonic and magmatic activity along the Laurentian margin since the Paleoproterozoic, we suggest that the SCLM would have been substantially thinner than in more inboard areas of Laurentia (where it is currently ~150 km-thick). As such, it is difficult to quantify the amount of SCLM that was removed between the Paleocene and the present to yield its current thickness of ca. 30 km (Harder and Russell, 2006).

The presence of metasomatic veins in the xenoliths is consistent with infiltration of asthenospheric alkaline melts and fluids into the lithospheric mantle. Melts and fluids percolating into the lithosphere may have contributed to its weakening and possible delamination (Bao et al., 2014; Bao and Eaton, 2015; Zhu and Zheng, 2009; Wang et al., 2015; Wang et al., 2016).

The origin of Archean and early Paleoproterozoic mantle beneath the eastern Cordillera, as documented in this study, is uncertain. Archean crustal blocks are present in the craton to the east, notably the Hearne province in the south and the Nova domain (possibly a displaced sliver of the Slave province) to the north (Ross, 2002). Both of these domains project geophysically in the subsurface from Alberta to the eastern Canadian Cordillera beneath British Columbia; their possible continuation farther west is obscured by the effects of Cordilleran tectonism (Lemieux et al., 2000). It is conceivable for these ancient regions to continue westward to the Omineca belt beneath the Tasse alkaline basalt and xenolith locality. These Archean crustal blocks may be underlain by Archean and Paleoproterozoic mantle, which could have been the source for the mantle xenoliths with early Paleoproterozoic and Archean model ages.

Another possibility is that the ancient mantle xenoliths were derived from lozenges of SCLM that were dislodged from Archean mantle domains of the Laurentian craton and transported westward to beneath the Cordillera by lateral asthenospheric flow. Liu et al. (2015) suggested that pieces of buoyant, viscous Archean lithospheric mantle can survive in a convecting mantle for billions of years and then can be added to the SCLM forming beneath Phanerozoic orogens (Fig. 15; King and Anderson, 1998; Hardebol et al., 2012). In our case, such fragments could have become re-attached to the SCLM beneath the Tasse locality, perhaps during the Cenozoic.

9. Conclusions

The following conclusions reflect integration of new petrographic, and Nd, Pb, Sr and O isotopic data with regional geological and geophysical information.

1. The Tasse spinel lherzolite xenoliths are hosted by the Quaternary Tasse alkaline basalts in the southeastern Canadian Cordillera of British Columbia, Canada. The Cordillera is a complex orogen that formed from nearly 2 billion years of tectonic and magmatic activity ranging from Proterozoic rifting to Mesozoic terrane collisions and Early Cenozoic extension. The Tasse basalts are part of an extensive intraplate field that erupted in the Late Cenozoic in a regime of widespread mantle upflow and probable thinning of the lithospheric mantle.
2. The xenoliths contain abundant feldspar veins, interconnected melt pockets and spongy cpx textures that record alkaline mantle metasomatism and partial melting. Formation of the melt pockets may have reduced the strength of the lithosphere, facilitating thinning and possible delamination.
3. Feldspar occurs as veins, interstitial crystals in the melt pockets, thin layers along grain boundaries and networks at triple junctions that connect the melt pockets and spongy cpx grains. Four types of feldspar solid solution have been recognized: Type 1, anorthoclase feldspar (Na-K solid solution); Type 2, plagioclase feldspar (Na-Ca solid solution); Type 3, alkali-dominated feldspar (Na-K-Ca solid solution; $Na_2O>K_2O>CaO$); and Type 4, plagioclase-dominated feldspar (Na-Ca-K solid solution; $Na_2O>K_2O$ and $CaO>K_2O$). Type 1 and Type 2 feldspars constitute two endmembers. Type 3 and 4 are variable mixtures of Type 1 and Type 2. Type 1 feldspar is interpreted to be the product of the reaction between low-silica alkaline melts and opx, through opx + melt → olivine + SiO_2. Silica (SiO_2) released by this reaction combined with K, Na and Al to form alkaline feldspar. Type 2 feldspar originated from partial melting of Na- and Al-bearing diopside in the xenoliths.
4. The melt pockets occur at triple junctions, along grain boundaries, and in feldspar veins. The pockets are composed mainly of olivine and cpx with minor opx and spinel, and are enclosed by interstitial feldspar, suggesting that the melt pockets originated through reaction of alkaline melts and fluids with the lithospheric mantle. Reactions between the melts and mantle minerals produced widespread resorption textures at the edges of olivine, cpx, opx and spinel. The amount of melting decreases from spinel, through cpx and opx, to olivine.
5. Spongy cpx texture is characterized by a core-rim structure. The core is composed of Na- and Al-bearing diopside (Type 1 cpx), whereas the rim consists of vermicular intergrowths of Na-free, low-Al diopside (Type 2 cpx) and feldspar (mainly Type 2 feldspar). Partial melting of

Type 1 cpx gave rise to Type 2 cpx and Type 2 feldspar. In some grains, feldspar in the rim partly to entirely comprises alkaline feldspars (Type 1 and Type 3), suggesting that alkaline melts also played a role in spongy cpx formation.

6. The xenoliths record two stages of metasomatism. Stage 1 is represented by infiltration of low-silica alkaline melts, melt pockets and formation of feldspar veins. Stage 2 is characterized by replacement of olivine and interstitial feldspar by Type 2 cpx in melt pockets and veins.
7. Neodymium, Sr and Pb isotope compositions indicate that the lithospheric mantle beneath the Canadian Cordillera contains variable contributions from DMM, EM1 and EM2 reservoirs. The xenoliths have Cretaceous to Paleoarchean Nd model ages (66–3380 Ma), depleted to enriched εNd (-8.2 to +9.6) values, and therefore record multiple melt extraction events and – for some samples – long-term isolation from the convecting mantle.
8. The trace element and Sr, Nd, Pb and O isotope compositions of the xenoliths and host alkaline basalts suggest that they were derived from different mantle sources. The xenoliths were derived from a shallow lithospheric source, whereas the alkaline basalts were derived from a deeper asthenospheric source.
9. Whole-rock oxygen isotope (average $\delta^{18}O$= +5.1±0.5‰) compositions of the xenoliths are similar to that of depleted mantle ($\delta^{18}O$=5.5±0.5‰). Although the $\delta^{18}O$ values of olivine, pyroxene and spinel follow typical pattern of mantle values for these minerals, decreasing from pyroxene, through olivine, to spinel, large fractionations between olivine-opx, olivine-cpx and opx-cpx pairs indicate isotopic disequilibrium. These fractionations are attributed to mantle metasomatism and partial melting.
10. Samples with Archean and Paleoproterozoic model ages are interpreted to have been derived from in situ SCLM located beneath the westward continuation of the Hearn province or Nova domain of the Laurentian craton. Another possibility is that the ancient mantle xenoliths were derived from lozenges of the SCLM that were dislodged from the craton and transported to the base of the Cordillera by asthenospheric flow.
11. Formation of the melt pockets may have reduced the strength of the lithosphere, facilitating its delamination.

12. We suggest that convergent plate margins characterized by accretionary orogens are not only sites of lithospheric construction, but also locations of lithospheric destruction through thinning and delamination.

Acknowledgements

This study was supported through an NSERC-Engage Grant (NSERC/EGP/433818-2012) to A. Polat and NSERC Discovery Grants to A. Polat, F.J. Longstaffe and D. Thorkelson. Field work was supported by Barker Minerals Ltd. We thank two anonymous reviewers for providing constructive and insightful comments. We acknowledge Barker Minerals Ltd for providing logistical support for the field work. Sharon Lackie is acknowledged for assisting with the SEM analyses. We thank Iain Samson for helpful discussion on the petrography. David Symons is acknowledged for providing helpful comments on the initial draft of the manuscript. We thank Toby Leeper and Toni Larsen for their assistance with Nd, Sr, and Pb isotope analyses, Andrea Prentice and Kim Law for their help with the oxygen isotope analyses, and John Valley for provision of the UWG-2 garnet standard. This paper is a contribution to IGCP 648 and is the University of Western Ontario Laboratory for Stable Isotope Science Contribution # 359.

References

Abraham, A.C., Francis, D., Polve, M., 2001. Recent alkaline basalts as probes of the lithospheric mantle roots of the Northern Canadian Cordillera. Chemical Geology 175, 361–386.

Abraham, A.C., Francis, D., Polvé, M., 2005. Origin of Recent alkaline lavas by lithospheric thinning beneath the northern Canadian Cordillera. Canadian Journal of Earth Sciences 42, 1073–1095.

Arai, S., Ishimaru, S., 2008. Insights into petrological characteristics of the lithosphere of mantle wedge beneath arcs through peridotite xenoliths: a review. Journal of Petrology 49, 665–695.

Armstrong, R.L., Ward, P., 1991. EvolvingG eographic patterns of Cenozoic magmatism in the North American Cordillera: The temporal and spatial association of magmatism and metamorphic core complexes. Journal of Geophysical Research 96, B8, 13,201-13,224.

Artemieva, I.M., 2011. The Lithosphere: An Interdisciplinary Approach. Cambridge University Press, 794 pp.

Audet, P., Bostock, M.G., Mercier, J.-P., Cassidy, J. F., 2008. Morphology of the Explorer–Juan de Fuca slab edge in northern Cascadia: Imaging plate capture at a ridge-trench-transform triple junction. Geology 36, 895–898.

Aulbach, S., Massuyeau, M., Gaillard, F., 2017. Origins of cratonic mantle discontinuities: A view from petrology, geochemistry and thermodynamic models. Lithos 268–271, 364–382.

Bao, X., Eaton, D.W., 2015. Large variations in lithospheric thickness of western Laurentia: Tectonic inheritance or collisional reworking? Precambrian Research 266, 579–586.

Bao, X., Eaton, D.W., Guest, B., 2014. Plateau uplift in western Canada caused by lithospheric delamination along a craton edge. Nature Geoscience 7, 830–833.

Bernstein, S., Kelemen, P.B., Brooks, C.K., 1998. Depleted spinel harzburgite xenoliths in Tertiary dykes from East Greenland: Restites from high degree melting. Earth and Planetary Science Letters 154, 221– 235.

Bevier, M.L., 1983. Implications of Chemical and Isotopic Composition for Petrogenesis of Chilcotin Group Basalts, British Columbia. Journal of Petrology 24, 207-226.

Bevier, M.L., Armstrong, R.L., Souther, J.G., 1979. Miocene peralkaline volcanism in west-central British Columbia—Its temporal and plate-tectonics setting. Geology 7, 389-392.

Bonadiman, C., Beccaluva, L., Coltorti, C., Siena, F., 2005. Kimberlite-like metasomatism and 'garnet signature' in spinel-peridotite xenoliths from Sal, Cape Verde Archipelago: relics of a subcontinental mantle domain within the Atlantic oceanic lithosphere? Journal of Petrology 46, 2465–2493.

Borthwick, J., Harmon, R.S., 1982. A note regarding ClF_3 as an alternative to BrF_5 for oxygen isotope analysis. Geochimica et Cosmochimica Acta 46, 1665–1668.

Breitsprecher, K., Thorkelson, D.J., Groome, W.G., J. Dostal, J., 2003. Geochemical confirmation of the Kula-Farallon slab window beneath the Pacific Northwest in Eocene time. Geology 31, 351–354.

Brearley, M., Scarfe, M., 1984. Amphibole in a spinel lherzolite xenolith: evidence for volatiles and partial melting in the upper mantle beneath southern British Columbia. Canadian Journal of Earth Sciences 21, 1067–1072.

Brearley M., Scarfe, C.M., Fujii, T., 1984. The petrology of ultramafic xenoliths from Summit Lake, near Prince George, British Columbia. Contributions to Mineralogy and Petrology 88, 53–63.

Canil, D., 2004. Mildly incompatible elements in peridotites and the origins of mantle lithosphere. Lithos 77, 375–393.

Canil, D., Brearley, M., Scarfe, C.M., 1987. Petrology of ultramafic xenoliths from Rayfield River, south-central British Columbia. Canadian Journal of Earth Sciences 24, 1679–1687.

Canil, D., Lee, C.-T.A., 2009. Were deep cratonic mantle roots hydrated in Archean oceans? Geology 37, 667–670.

Canil, D., Scarfe, C.M., 1989. Origin of phlogopite in mantle xenoliths from Kostal Lake, Wells Gray Park, British Columbia. Journal of Petrology 30, 1159–1179.

Carlson, R. W., Irving, A. J., Schulze, D.J., Hearn Jr, B. C., 2004. Timing of Precambrian melt depletion and Phanerozoic refertilization events in the lithospheric mantle of the Wyoming craton and adjacent Central Plains Orogen. Lithos 77, 453–472.

Carlson, R. W., Pearson, D. G., James, D. E., 2005. Physical, chemical, and chronological characteristics of continental mantle. Reviews in Geophysics 43, RG1001, doi:10.1029/2004RG000156.

Carpenter R.L., Edgar, A.D., Thibault, Y., 2002. Origin of spongy textures in clinopyroxene and spinel from mantle xenoliths, Hessian Depression, Germany. Mineralogy and Petrology 74, 149–162.

Chazot, G., Lowry, D., Menzies, M., Mattey, D., 1997. Oxygen isotopic composition of hydrous and anhydrous mantle peridotites. Geochimica et Cosmochimica Acta 61, 161–169.

Chiba H., Chacko T., Clayton R. N., and Goldsmith J. R. (1989) Oxygen isotope fractionation involving diopside, magnetite, and calcite: application to geothermometry. Geochimica et Cosmochimica Acta 53, 2985–2995.

Clayton. R.N., Mayeda, T.K., 1963. The use of bromine pentafluoride in the extraction of oxygen from oxides and silicates for isotopic analysis. Geochimica et Cosmochimica Acta 27, 43–52.

Clowes, R.M., Zelt, C.A., Amor, J.R., Ellis, R.M., 1995. Lithospheric structure in the southern Canadian Cordillera from a network of seismic refraction lines. Canadian Journal of Earth Sciences 32, 1485–1513.

Colpron, M., Nelson, J.L., 2009. A Palaeozoic Northwest Passage: incursion of Caledonian, Baltican and Siberian terranes into eastern Panthalassa, and the early evolution of the North

American Cordillera. In: Cawood, P. A., Kröner, A. (Eds), Earth Accretionary Systems in Space and Time. The Geological Society, London, Special Publications, 318, 273–307.

Cook, F.A., 1995a. The reflection Moho beneath the southern Canadian Cordillera. Canadian Journal of Earth Sciences 32, 11520–11530.

Cook, F.A., 1995b. Lithospheric processes and products in the southern Canadian Cordillera: a Lithoprobe perspective. Canadian Journal of Earth Sciences 32, 1803–1824.

Cook, F.A., Erdmer, P., 2005. An 1800 km cross section of the lithosphere through the northwestern North American plate: lessons from 4.0 billion years of Earth's history. Canadian Journal of Earth Sciences 42, 1295–1311.

Cook, F.A., Varsek, J.L., Clowes, R.M., Kanasewich, E.R., Spencer, C.S., Parrish, R.R., Brown, R.L., Carr, S.D., Johnson, B.J., Price, R.A., 1992. Lithoprobe crustal reflection cross section of the southern Canadian Cordillera, 1, Foreland thrust and fold belt to Fraser River Fault. Tectonics 11, 12-35.

Coney, P.J., Jones, D.L., Monger, J.W.H., 1980. Cordilleran suspect terranes. Nature 288, 329–333.

Currie, C.A., Huismans, R.S., Beaumont, C., 2008. Thinning of continental backarc lithosphere by flow-induced gravitational instability. Earth and Planetary Science Letters 269, 436–447.

Currie, C.A., Hyndman, R.D. 2006. The thermal structure of subduction zone back arcs. J. Journal of Geophysics Research 111, B08404, doi:10.1029/2005JB004024.

DePaolo, D.J., 1981. Neodymium isotope geochemistry: An introduction. New York, Springer-Verlag, pp. 187.

Dickinson, W.R., Snyder, W.S., 1979. Geometry of triple junctions related to San Andreas transform. Journal of Geophysical Research 84 (NB2), 561–572.

Dixon, J.M., Farrar, E., 1980. Ridge subduction, education, and the Neogene Tectonics of southwestern North America. Tectonophysics 67, 81-99.

Dostal, J., Breitsprecher, K., Church, B.N., Thorkelson, D., Hamilton, T.S., 2003. Eocene melting of Precambrian lithospheric mantle: Analcime-bearing volcanic rocks from the Challis-Kamloops belt of south central British Columbia. Journal of Volcanology and Geothermal Research 126, 303-326.

Dostal, J., Keppie, J.D., Church, B.N., Reynolds, H., Reid, C.R., 2008. The Eocene-Oligocene magmatic hiatus in the south-Central Canadian Cordillera: a capture of the Kula plate by the Pacific plate? Canadian Journal of Earth Sciences 45, 69-82.

Eddy, M.P., Clark, K.P., Polenz, M., 2017. Age and volcanic stratigraphy of the Eocene Siletzia oceanic plateau in Washington and on Vancouver Island. Lithosphere, GSA Data Repository Item 2017232 https://doi.org/10.1130/L650.1.

Edwards, B.R. Russell, J.K., 1999. Northern Cordilleran volcanic province: A northern Basin and Range? Geology 27, 243–246.

Edwards, B.R., Russell, J.K., 2000. Distribution, nature, and origin of Neogene–Quaternary magmatism in the northern Cordilleran volcanic province, Canada. Geological Society of America Bulletin 112, 1280–1295.

Edwards, B.R., Russell, J.K., Anderson, R.G., 2002. Subglacial, phonolitic volcanism at Hoodoo Mountain volcano, northern Canadian Cordillera. Bulletin of Volcanology 64, 254–272.

Eiler, J.M., 2001. Oxygen isotope variations in basaltic lavas and upper mantle rocks. In: Valley J.W., Cole, D.R. (Eds.), Stable Isotope Geochemistry. Reviews in Mineralogy and Geochemistry, 43, Mineralogical Society of America, Washington, pp. 319–364.

Ewing, T.E., 1980. Paleogene Tectonic Evolution of the Pacific Northwest. The Journal of Geology 88, 619-638.

Francis, D., Ludden, J. 1995. The signature of amphibole in mafic alkaline lavas, a study in the northern Canadian Cordillera. Journal of Petrology 36, 1171–1191.

Francis, D., Minarik, W., Proenza, Y., Shi, L., 2010. An overview of the Canadian Cordilleran lithospheric mantle. Canadian Journal of Earth Sciences 47, 353–368.

Frederiksen, A.W., Bostock, M.G., Cassidy, J.F., 2001. S-wave velocity structure of the Canadian upper mantle. Physics of the Earth and Planetary Interiors 124, 175–191.

Friedman, E., Polat, A., Thorkelson, D.J. Frei, R., 2016. Lithospheric mantle xenoliths sampled by melts from upwelling asthenosphere: the Quaternary Tasse alkaline basalts of southeastern British Columbia, Canada. Gondwana Research 33, 200–230.

Fujii, T., Scarfe, C.M., 1982. Petrology of ultramafic nodules from West Kettle River, near Kelowna, southern British Columbia. Contributions to Mineralogy and Petrology 80, 297–306.

Furlanetto, F. Thorkelson, D.J., Rainbird, R.H., Davis, W.J., Gibson, H.D., Marshall, D.D., 2016. The Paleoproterozoic Wernecke Supergroup of Yukon, Canada: Relationships to orogeny in northwestern Laurentia and basins in North America, East Australia, and China. Gondwana Research 39, 14–40.

Gabrielse, H., Monger, J.W.H., Wheeler, J.O., and Yorath, C.J., 1991. Part A. Morphogeological belts, tectonic assemblages, and terranes. In: Gabrielse, H., and Yorath, C. J. (Eds.), Chapter 2 of Geology of the Cordilleran Orogen in Canada: Geological Survey of Canada, Geology of Canada, no.4, p. 15–28 (also Geological Society of America, The Geology of North America, v. G–2).

Gabrielse, H., Yorath, C.J., 1991. Tectonic synthesis. In: Gabrielse, H., Yorath, C.J. (Eds.), Geology of the Cordilleran Orogen in Canada. Geological Survey of Canada, 677–706.

Gao, S., Rudnick, R.L., Carlson, R. W., McDonough, W. F., Liu, Y.-S., 2002. Re–Os evidence for replacement of ancient mantle lithosphere beneath the north China craton. Earth and Planetary Science Letters 198, 307–322.

Gibson, H.D. Brown, R.L., Carr, S.D., 2008. Tectonic evolution of the Selkirk fan, southeastern Canadian Cordillera: A composite Middle Jurassic–Cretaceous orogenic structure. Tectonics 27, TC6007, doi:10.1029/2007TC002160.

Gill, R., 2010. Igneous Rocks and Processes: A Practical Guide. Wiley-Blackwell: Chichester, UK, pp. 428.

Gough, D.I., 1984. Mantle flow under North America and plate dynamics. Nature 311, 428-433.

Greenfield, A.M.R., Ghent, E.D., Russell, J.K., 2013. Geothermobarometry of spinel peridotites from southern British Columbia: implications for the thermal conditions in the upper mantle. Canadian Journal of Earth Sciences 50, 1019–1032.

Griffin, W.L., O'Reilly, S.Y., Abe, N., Aulbach, S. Davies, R.M. Pearson, N.J., Doyle, B.J., Kivi, K., 2003. The origin and evolution of Archean lithospheric mantle. Precambrian Research 127, 19–41.

Gu, Y. J., Zhang, Y., Sacchi, M.D., Chen, Y., Contenti, S., 2015. Sharp mantle transition from cratons to Cordillera in southwestern Canada, Journal of Geophysical Research Solid Earth, 120, doi:10.1002/ 2014JB011802.

Hammer, P.T.C., Clowes, R.M., 2004. Accreted terranes of northwestern British Columbia, Canada: Lithospheric velocity structure and tectonics. Journal of Geophysical Research 109, B06305, doi:10.1029/2003JB002749.

Hao, Y.T., Xia, Q.K., Dallai, L., Coltorti, M., 2015. Recycled oceanic crust-derived fluids in the lithospheric mantle of eastern China: Constraints from oxygen isotope compositions of peridotite xenoliths. Lithos 228–229, 55–61.

Hardebol, N.J., Pysklywec, R. N., Stephenson, R., 2012. Small-scale convection at a continental back-arc to craton transition: Application to the southern Canadian Cordillera. Journal of Geophysical Research 117, B01408, doi:10.1029/2011JB008431.

Harder, M., Russell, J.K., 2006. Thermal state of the upper mantle beneath the Northern Cordilleran Volcanic Province (NCVP), British Columbia, Canada. Lithos 87, 1–22.

Haeussler, P.J., Bradley, D.C., Wells, R.E., Miller, M.L., 2003. Life and death of the Resurrection plate: Evidence for its existence and subduction in the northeastern Pacific in Paleocene–Eocene time. GSA Bulletin 115, 867–880.

Herzberg, C., Rudnick, R., 2012. Formation of cratonic lithosphere: An integrated thermal and petrological model: Lithos 149, 4–15.

Hickson, C.J., Souther, J.G., 1984. Late Cenozoic volcanic rocks of the Clearwater - Wells Gray area, British Columbia. Canadian Journal Earth Sciences 21, 267-277.

Hofmann, A.W., 1997. Mantle geochemistry: the message from oceanic volcanism. Nature 385, 219–229.

Hoffman, P.F., 1989. Precambrian geology and tectonic history of North America. In: Bally, A.W., Palmer. A.R. (Eds.), The geology of North America — an overview, Geological Society of America, The Geology of North America, Vol. A, pp. 447–512.

Houseman, G.A., Molnar, P., 1997. Gravitational (Rayleigh-Taylor) instability of a viscosity and convective thinning of continental layer with non-linear Lithosphere. Geophysical Journal International 128, 125-150.

Hyndman, R. 2010. The consequences of Canadian Cordillera thermal regime in recent tectonics and elevation: a review. Canadian Journal of Earth Sciences 47: 621–632.

Hyndman, R., Currie, C.A. 2011. Why is the North American Cordillera high? Hot backarcs, thermal isostasy, and mountain belts. Geology 39: 783–786.

Hyndman, R.D., Currie, C.A., Mazzotti, S.P., 2005. Subduction zone backarcs, mobile belts, and orogenic heat. GSA Today 15, 4–10.

Hyndman, R.D., Currie, C.A., Mazzotti, S.P., Frederiksen, A., 2009. Temperature control of continental lithosphere elastic thickness, Te vs Vs: Earth and Planetary Science Letters 277, 539–548.

Hyndman, R.D., Lewis, T.J., 1999. Geophysical consequences of the Cordillera thermal transitions in southwestern Canada. Tectonophysics 306, 397–422.

Ickert, R.B., Thorkelson, D.J. Marshall, D.D., Ullrich, T.D., 2009. Eocene adakitic volcanism in southern British Columbia: Remelting of arc basalt above a slab window. Tectonophysics 464, 164–185.

Ionov, D.A. Chazot, G., Chauvel, C., Merlet, C., Bodinier, J.L., 2006. Trace element distribution in peridotite xenoliths from Tok, SE Siberian craton: A record of pervasive, multi-stage metasomatism in shallow refractory mantle. Geochimica et Cosmochimica Acta 70, 1231–1260.

Ionov, D.A., Gre´goire, M., Prikhodko, V.S., 1999. Feldspar–Ti-oxide metasomatism in off-cratonic continental and oceanic upper mantle. Earth and Planetary Science Letters 165, 37–44.

Ionov, D.A., O'Reilly, S.Y., Ashchepkov, I.V., 1995. Feldspar-bearing lherzolite xenoliths in alkali basalts from Hamar-Daban, southern Baikal region, Russia. Contributions to Mineralogy and Petrology 122, 174–190.

Ito, E., White, W.M., Gopel, C., 1987. The O, Sr, Nd, and Pb isotope geochemistry of MORB. Chemical Geology 62, 157–176.

Jones, C.H., Reeg, H., Zandt, G., Gilbert, H., Owens, T.J., Stachnik, J., 2014. P-wave tomography of potential convective downwellings and their source regions, Sierra Nevada, California. Geosphere 10, 505–533.

Karlstrom, K.E., Åhäll, K.I., Harlan, S.S., Williams, M.L., McLelland, J., Geissman, J.W., 2001. Long-lived (1.8–1.0 Ga) convergent orogen in southern Laurentia, its extensions to Australia and Baltica, and implications for refining Rodinia. Precambrian Research 111, 5–30.

King, S.D., Anderson, D.L., 1998. Edge-drive convection. Earth and Planetary Science Letters 160, 289–296.

Kopylova, M., Russell, J.K., 2000. Chemical stratification of cratonic lithosphere: constraints from the northern Slave craton, Canada. Earth and Planetary Science Letters 181, 71– 87.

Kuehn, C., Guest, B., Russel, J.K., Benowitz, J.A., 2015. The Satah Mountain and Baldface Mountain volcanic fields: Pleistocene hot spot volcanism in the Anahim Volcanic Belt, west-central British Columbia, Canada. Bulletin of Volcanology 77, 3–27.

Kusky, T.M., Bradley, D., Donley, D.T., Rowley, D., and Haeussler, P. 2003. Controls on intrusion of near-trench magmas of the Sanak-Baranof belt, Alaska, during Paleogene ridge subduction, and consequences for forearc evolution. In: Sisson, V.B., Roeske, S.M., Pavlis, T.L. (Eds.), Geology of a Transpressional Orogen Developed during Ridge-Trench interaction along the North Pacific Margin.. Geological Society of America Special Paper 371, 269–292.

Kyser, T.K., O'Neil, J.R., Carmichael, I.S.E., 1981. Oxygen isotope thermometry of basic lavas and mantle nodules. Contributions to Mineralogy and Petrology 77, 11–23.

Lemieux, S., Ross, G.M., Cook, F.A., 2000. Archean crystalline basement beneath the southern Alberta Plains, from new seismic reflection and potential-field studies. Canadian Journal of Earth Sciences 37, 1473–1491.

Lewis, T.J., Bentkowski, W.H., Hyndman, R.D., 1992. Crustal temperatures near the Lithoprobe Southern Canadian Cordillera transect. Canadian Journal of Earth Sciences 29, 1197–1214.

Lewis, T., Hyndman, R., Fluck, P., 2003. Heat flow, heat generation, and crustal temperatures in the northern Canadian Cordillera: thermal control of tectonics. Journal of Geophysical Research-Solid Earth 108: 2316. doi: 10.1029/2002JB002090.

Li, Z.X., Bogdanova, S.V., Collins, A.S., Davidson, A., De Waele, B., Ernst, R.E., Fitzsimons, I.C.W., Fuck, R.A., Gladkochub, D.P., Jacobs, J., Karlstrom, K.E, Lu, S., Natapov, L.M., Pease, V., Pisarevsky, S.A., Thrane, K., Vernikovsky, V., 2008. Assembly, configuration, and break-up history of Rodinia: A synthesis. Precambrian Research 160, 179–210.

Littlejohn, A.L., Greenwood, H.J., 1974. Lherzolite nodules in basalts from British Columbia, Canada. Canadian Journal of Earth Sciences 11, 1288– 1308.

Liu, J.G., Scott, J.M., Martin, C.E., Pearson, D.G., 2015. The longevity of Archean mantle residues in the convecting upper mantle and their role in young continent formation. Earth and Planetary Science Letters 424, 109–118.

Liu, C.Z., Yang, L.Y., Li, X.H., Tchouankoue, J.P., 2017. Age and Sr–Nd–Hf isotopes of the sub-continental lithospheric mantle beneath the Cameroon Volcanic Line: Constraints from the Nyos mantle xenoliths. Chemical Geology 455, 84–97.

Madsen, J.K., Thorkelson, D.J., Friedman, R.M., Marshall, D.D., 2006. Cenozoic to Recent plate configurations in the Pacific Basin: Ridge subduction and slab window magmatism in western North America. Geosphere 2, 11–34.

Martin, A.P., Cooper, A.F., Price, R.C., 2013. Petrogenesis of Cenozoic, alkalic volcanic lineages at Mount Morning, West Antarctica and their entrained lithospheric mantle xenoliths: Lithospheric versus asthenospheric mantle sources. Geochimica et Cosmochimica Acta 122, 127–152.

Mattey, D., Lowry, D., Macpherson, C., 1994. Oxygen isotope composition of mantle peridotite. Earth and Planetary Science Letters 128, 231–241.

Mazzotti, S., Hyndman, R.D., 2002. Yakutat collision and strain transfer across the northern Canadian Cordillera. Geology 30, 495–498.

McKenzie, D., Bickle, M.J., 1988. The volume and composition of melt generated by extension of the lithosphere. Journal of Petrology 29, 623-679.

Menzies, M.A., 1990. Petrology and geochemistry of the continental mantle: an historical perspective. In: Menzies, M.A. (Ed.), Continental Mantle. Oxford Monographs on Geology and Geophysics, Oxford University Press, Oxford, pp. 31–54.

Mercier, J.-P., Bostock, M.G., Cassidy, J.F., Dueker, K., Gaherty, J.B., Garnero, E.J., Revenaugh, J., Zandt, G., 2009. Body-wave tomography of western Canada. Tectonophysics 475, 480–492.

Milidragovic, D., Thorkelson, D.J., Davis, W.J., Marshall, D.D., Gibson, H.D., 2011. Evidence for late Mesoproterozoic tectonism in northern Yukon and the identification of a Grenville-age tectonothermal belt in western Laurentia. Terra Nova 23, 307–313.

Miller, M.F., Franchi, I.A., Sexton, A.S., Pillinger, C.T., 1999. High precision δ^{17}O isotope measurements of oxygen from silicates and other oxides: methods and applications. Rapid Communications in Mass Spectrometry 13, 1211–1217.

Monger, J., 2014. Seeking the suture: The Coast-Cascade conundrum. Geoscience Canada 41, 379–398.

Monger, J.W.H., Price, R.A., Tempelman-Kluit, D.J., 1982. Tectonic accretion and the origin of the two major metamorphic and plutonic welts in the Canadian Cordillera. Geology 10, 70-75.

Monger, J., Price, R., 2002. The Canadian Cordillera: Geology and tectonic evolution. CSEG Recorder, February: 17–36.

Moores, E.M., 1991. Southwest U.S.-East Antarctic (SWEAT) connection: A hypothesis. Geology 19, 425–428.

Morales, L.F.G., Tommasi, A., 2011. Composition, textures, seismic and thermal anisotropies of xenoliths from a thin and hot lithospheric mantle (Summit Lake, southern Canadian Cordillera). Tectonophysics 507, 1–15.

Moynihan, D.P. and Pattison, D.R.M., 2013. Barrovian metamorphism in the central Kootenay Arc, British Columbia: petrology and isograd geometry; Canadian Journal of Earth Sciences 50, 769–794.

Mullen, E.K., Weis, D., 2015. Evidence for trench-parallel mantle flow in the northern Cascade Arc from basalt geochemistry. Earth and Planetary Science Letters 414, 100–107.

Mundl, A., Ntaflos, T., Ackerman, L., Bizimis, M., Bjerg, E.A., Wegner, W., Hauzenberger, C.A., 2016. Geochemical and Os–Hf–Nd–Sr isotopic characterization of North Patagonian mantle xenoliths: Implications for extensive melt extraction and percolation processes. Journal of Petrology 57, 685–715.

Nicholls, J., Stout, M.Z., Fiesinger, D.W., 1982. Petrologic variations in Quaternary volcanic rocks, British Columbia, and the nature of the underlying mantle. Contributions to Mineralogy and Petrology 79, 201–218.

Ntaflos, T., Bizimis, M., Abart, R., 2017. Mantle xenoliths from Szentb´ek´alla, Balaton: Geochemical and petrological constraints on the evolution of the lithospheric mantle underneath Pannonian Basin, Hungary. Lithos 276, 30–44.

O'Reilly, S.Y., Griffin, W.L., 2013. Mantle metasomatism. In: Harlov, D.E., Austrheim, H. (Eds.), Metasomatism and the Chemical Transformation of Rock. Springer Verlag, Berlin Heidelberg, pp. 471–533.

Parrish, R.R., Carr, S.D., Parkinson, D.L., 1988. Eocene extensional tectonics and geochronology of the southern Omineca Belt, British Columbia and Washington. Tectonics 7, 181–212.

Pearson, D.G., Canil, D., Shirey, S.B., 2005. Mantle samples included in volcanic rocks: xenoliths and diamonds. In: Holland, H.D., Turekian, K.K., Carlson, R.W. (Eds.), Treatise on Geochemistry: the Mantle and the Core. Elsevier Pergamon Amsterdam, pp. 175–275.

Pearson, D.G., Wittig, N., 2008. Formation of Archaean continental lithosphere and its diamonds: the root of the problem. Journal of the Geological Society of London 165, 895–914.

Perkins, G.B., Sharp, Z.D., Selverstone, J., 2006. Oxygen isotope evidence for subduction and rift-related mantle metasomatism beneath the Colorado Plateau–Rio Grande rift transition. Contributions to Mineralogy and Petrology 151, 633–650.

Peslier, A.H., Reisberg, L., Ludden, J., Francis, D., 2000. Os isotopic systematics in mantle xenoliths; age constraints on the Canadian Cordillera lithosphere. Chemical Geology 166, 85–101.

Peslier, A., Francis, D., Ludden, J., 2002. The lithospheric mantle beneath continental margins: Melting and melt-rock reaction in Canadian Cordillera Xenoliths. Journal of Petrology 43, 2013–2048.

Pilet, S., Baker, M.B., Stolper, E.M., 2008. Metasomatized lithosphere and the origin of alkaline lavas. Science 320, 916–919.

Polat, A., Longstaffe, F.J., 2014. A juvenile oceanic island arc origin for the Archean (ca. 2.97 Ga) Fiskenæsset Anorthosite Complex, southwestern Greenland: Evidence from oxygen isotopes. Earth and Planetary Science Letters, 396, 252–266.

Price, M., 2012. The Genesis of PGE Mineralization in the River Valley Intrusion, Ontario, Canada. Electronic Theses and Dissertations. University of Windsor, Earth and Environmental Sciences. 5600. http://scholar.uwindsor.ca/etd/5600.

Riddihough, R. P., Currie, R.G., Hyndman, R.D., 1980. The Dellwood knolls and their role in triple junction tectonics off northern Vancouver Island. Canadian Journal of Earth Sciences 17, 577-593.

Rivers, T., Corrigan, D., 2000. Convergent margin on southeastern Laurentia during the Mesoproterozoic: tectonic implications. Canadian Journal of Earth Sciences 37, 359–383.

Rocco, I., Lustrino, M., Morra, V., Melluso, L., 2012. Petrological, geochemical and isotopic characteristics of the lithospheric mantle beneath Sardinia (Italy) as indicated by ultramafic xenoliths enclosed in alkaline lavas. International Journal of Earth Sciences 101, 1111–1125.

Rocco, I., Lustrino, M., Zanetti, A., Morra, V., Melluso, L., 2013. Petrology of ultramafic xenoliths in Cenozoic alkaline rocks of northern Madagascar (Nosy Be Archipelago). Journal of South American Earth Sciences 41, 122–139.

Rocco, I., Zanetti, A., Melluso, L., Morra, V., 2017. Ancient depleted and enriched mantle lithosphere domains in northern Madagascar: Geochemical and isotopic evidence from spinel-to-plagioclase-bearing ultramafic xenoliths. Chemical Geology 466, 70–85.

Ross, J.V., 1983. The nature and rheology of the Cordilleran upper mantle of British Columbia: inferences from peridotite xenoliths. Tectonophysics 100, 321–357.

Ross, G.M., 2002. Evolution of Precambrian continental lithosphere in Western Canada: results from Lithoprobe studies in Alberta and beyond. Canadian Journal of Earth Sciences 39, 413–437.

Ross, G.M., Parrish, R.R., Winston, D., 1992. Provenance and U-Pb geochronology of the Mesoproterozoic Belt Supergroup (northwestern United States): implications for age of deposition and pre-Panthalassa plate reconstructions. Earth and Planetary Science Letters, 113, 57-76.

Scott, J.M., Brenna, M., Crase, J.A., Waight, T.E., van der Meer, Q.H.A., Cooper, A.F., Palin, J.M., Le Roux, P., Münker, C., 2016. Peridotitic lithosphere metasomatized by volatile-bearing melts, and its association with intraplate alkaline HIMU-like magmatism. Journal of Petrology 57, 2053–2078.

Şengör, A.M.C, Lom, N., Sağdıç, N.G., 2018. Tectonic inheritance, structure reactivation and lithospheric strength: the relevance of geological history. In: Wilson, R.W., Houseman, G.A., McCaffrey, K.J.W., Doré, A.G., Buiter, S.J.H. (Eds), Fifty Years of the Wilson Cycle Concept in Plate Tectonics. Geological Society, London, Special Publications, 470, https://doi.org/ 10.1144/SP470.8.

Sharp, Z.D., 1990. A laser-based microanalytical method for the *in situ* determination of oxygen isotope ratios of silicates and oxides. Geochimica et Cosmochimica Acta 54, 1353–1357.

Sharp, Z.D., 1995. Oxygen isotope geochemistry of the Al_2SiO_5 polymorphs. American Journal of Science 295, 1058–1076.

Shaw, C.S.J., Heidelbach, F., Dingwell, D.B., 2006. The origin of reaction textures in mantle peridotite xenoliths from Sal Island, Cape Verde: the case for ‘‘metasomatism’’ by the host lava. Contributions to Mineralogy and Petrology 151, 681–697.

Shaw, C.S.J., Klügel, A., 2002. The pressure and temperature conditions and timing of glass formation in mantle-derived xenoliths from Baarley, West Eifel, Germany: the case for amphibole breakdown, lava infiltration and mineral-melt reaction. Mineralogy and Petrology 74, 163–187.

Shaw, C.S.J., Thibault, Y., Edgar, A.D., Lloyd, F.E., 1998. Mechanisms of orthopyroxene dissolution in silica-undersaturated melts at 1 atmosphere and implications for the origin of silica-rich glass in mantle xenoliths. Contributions to Mineralogy and Petrology, 132: 354-370.

Sigloch, K., Mihalynuk, M.G., 2013. Intra-oceanic subduction shaped the assembly of Cordilleran North America. Nature 496, 50–56.

Sigloch, K., Mihalynuk, M.G., 2017. Mantle and geological evidence for a Late Jurassic–Cretaceous suture spanning North America. Geological Society of America Bulletin. DOI: 10.1130/B31529.1

Simon, N.S.C., Carlson, R.W., Pearson, D.G., Davies, G.R., 2007. The origin and evolution of the Kaapvaal cratonic lithospheric mantle. Journal of Petrology 48, 589–625.

Snyder, D.B., Pilkington, M., Clowes, R.M., Cook, F.A., 2009. The underestimated Proterozoic component of the Canadian Cordillera accretionary margin. In: Cawood, P.A., Kroner, A. (Eds.), Earths Accretionary Systems in Space and Time. Geological Society, London, Special Publications 318, 257–271.

Souther, J.G., 1986. The western Anahim Belt: root zone of a peralkaline magma system. Canadian Journal of Earth Sciences 23, 895-908.

Souther, J.G., 1992. The late Cenozoic Mount Edziza Volcanic Complex, British Columbia. Geological Survey of Canada Memoir 420, 320 pp.

Stout, M. Z, Nicholls, J., 1983. Origin of the hawaiites from the Itcha Mountain Range, British Columbia. Canadian Mineralogist 21, 575-581.

Stracke, A., Hofmann, A.W., Hart, S.R., 2005. FOZO, HIMU, and the rest of the mantle zoo. Geochemistry, Geophysics, Geosystems 6, 1–20. Q05007, doi:10.1029/2004GC000824.

Su, B.X., Zhang, H.F., Sakyi, P.A., Yang, Y.H., Ying, J.F., Tang, Y.J., Qin, K.Z., Xiao, Y., Zhao, X.M., Mao, Q., Ma, Y.G., 2011. The origin of spongy texture in minerals of mantle xenoliths from the Western Qinling, central China. Contributions to Mineralogy and Petrology 161, 465–482.

Sun, M., Armstrong R.L., Maxwell, R.J., 1991. Proterozoic mantle under Quesnellia: variably reset Rb–Sr mineral isochrones in ultramafic nodules carried up in Cenozoic volcanic vents of the southern Omineca Belt. Canadian Journal of Earth Sciences 28, 1239–1253.

Sun, M., Kerrich, R., 1995. Rare earth element and high field strength element characteristics of whole rocks and mineral separates of ultramafic nodules in Cenozoic volcanic vents of southeastern British Columbia, Canada. Geochimica et Cosmochimica Acta 59, 4863–4879.

Sun, S.S., McDonough, W.F., 1989. Chemical and isotopic systematics of oceanic basalts: implications for mantle composition and processes. In: Saunders, A.D., Norry, M.J. (Eds.), Magmatism in the Ocean Basins, Society of London, Special Publications 42, 313–345.

Temdjim, R., 2012. Ultramafic xenoliths from Lake Nyos area, Cameroon volcanic line, West-central Africa: Petrography, mineral chemistry, equilibration conditions and metasomatic features. Chemie der Erde 72, 39–60.

Todt, W., Cliff, R.A., Hanser, A., Hofmann, A.W., 1993. Re-calibration of NBS lead standards using ^{202}Pb + ^{205}Pb double spike. Terra Abstract 5, 396.

Thorkelson, D.J., Laughton, J.R., 2016. Paleoproterozoic closure of an Australia–Laurentia seaway revealed by megaclasts of an obducted volcanic arc in Yukon, Canada. Gondwana Research 33, 115–133.

Thorkelson, D.J., Madsen, J.K., Sluggett, C.L., 2011. Mantle flow through the Northern Cordilleran slab window revealed by volcanic geochemistry. Geology 39, 267–270.

Thorkelson, D.J., Taylor, R.P., 1989. Cordilleran slab windows. Geology 17, 833–836.

Valley, J.W., Kitchen, N., Kohn M.J., Niendorf, C.R., Spicuzza, M.J., 1995. UWG-2, a garnet standard for oxygen isotope ratios: strategies for high precision and accuracy with laser heating. Geochimica et Cosmochimica Acta 59, 5223–5231.

Van der Lee and Frederiksen, 2005. Surface wave tomography applied to the North American upper mantle, in Seismic Earth: Array Analysis of Broadband Seismograms, American Geophysical Union, Geophysical Monograph 157, pp. 67-80.

Viljoen, K.S., Smith, C.B., Sharp, Z.D., 1996. Stable and radiogenic isotope study of eclogite xenoliths from the Orapa kimberlite, Botswana. Chemical Geology 13l, 235–255.

Wang, H., Hunen, J., Pearson, D.G., 2015. The thinning of subcontinental lithosphere: The roles of plume impact and metasomatic weakening, Geochemistry Geophysics Geosystems 16, 1156–1171, doi:10.1002/ 2015GC005784.

Wang, X., Zhu, P., Kusky, T.M., Zhao, N., Li, X., Wang, Z., 2016. Dynamic cause of marginal lithospheric thinning and implications for craton destruction: a comparison of the North China, Superior, and Yilgarn cratons. Canadian Journal of Earth Sciences 53, 1121–1141. dx.doi.org/10.1139/cjes-2015-0110.

White, R., McKenzie, D., 1989. Magmatism at Rift Zones: The Generation of Volcanic Continental Margins and Flood Basalts. Journal of Geophysical Research 94, B6, 7685-7729.

Wiechert, U., Ionov, D.A., Wedepohl, K.H., 1997. Spinel peridotite xenoliths from the Atsagin-Dush volcano, Dariganga lava plateau, Mongolia: a record of partial melting and cryptic metasomatism in the upper mantle. Contributions to Mineralogy and Petrology 126, 345–364.

Wu, T., Polat, A., Frei, R., Fryer, B.J., Yang, K., Kusky, T., 2016. Geochemistry, Nd, Pb and Sr isotope systematics, and U–Pb zircon ages of the Neoarchean Bad Vermilion Lake Greenstone Belt and spatially associated granitic rocks, Western Superior Province, Canada. Precambrian Research 258, 21–51.

Xue, X., Baadsgaard, H., Irving, A.J., Scarfe, C.M., 1990. Geochemical and isotopic characteristics of lithospheric mantle beneath West Kettle River, British Columbia: Evidence from ultramafic xenoliths. Journal of Geophysical Research 95, B10, 15,879–15,891.

Xu, W.L., Zhou, Q.J., Pei, F.P., Yang, D.B., Gao, S., Li, Q.L., Yang, Y.H., 2013. Destruction of the North China Craton: Delamination or thermal/chemical erosion? Mineral chemistry and oxygen isotope insights from websterite xenoliths. Gondwana Research 23, 119–129.

Young, H.P., Lee, C.T.A., 2009. Fluid-metasomatized mantle beneath the Ouachita belt of southern Laurentia: Fate of lithospheric mantle in a continental orogenic belt. Lithosphere 1, 370–383.

Zaporozan, T., Frederiksen, A.W., Bryksin, A., Darybshire, F., 2018. Surface-wave images of Western Canada: Lithospheric variations across the Cordillera/Craton Boundary. Canadian Journal of Earth Sciences (in press).

Zhao, G., Sun, M., Wilde, S.A., Li, S., 2004. A Paleo-Mesoproterozoic supercontinent: assembly, growth and breakup. Earth-Science Reviews 67, 91–123.

Zheng, Y., Wei, C., Zhou, G., Xu, B., 1998. Oxygen isotope fractionations in mantle minerals. Science in China (D Series) 41, 95–103.

Zhou, S., Polat, A., Longstaffe, F.J., Yang, K.G., Fryer, B.J., Weisener, C., 2016. Formation of the Neoarchean Bad Vermilion Lake Anorthosite Complex and spatially associated granitic rocks at a convergent plate margin, Superior Province, Western Ontario, Canada. Gondwana Research 33, 134–159.

Zhu, R., T. Zheng, 2009. Destruction geodynamics of the North China craton and its Paleoproterozoic plate tectonics, Chinese Science Bulletin 54, 3354–3366, doi:10.1007/s11434-009-0451-5.

FIGURE CAPTIONS

Fig. 1. (a) Map of North America showing location of Tasse volcanics and xenoliths within the Province of British Columbia (BC), Canada. (b) Map of the northwestern Cordillera showing Tasse locality in context of main tectonic features and Late Cenozoic volcanic belts. Present-day extent of intact subducted oceanic lithosphere of Pacific and Explorer/Juan de Fuca plates is separated by Northern Cordilleran slab window of Thorkelson et al. (2011). Edge of thick subcontinental lithospheric mantle (SCLM) based on shear-wave velocity maps of Frederiksen et al. (2001) and Bao et al. (2014). Cross section A-B is shown in Fig. 15. ABVB: Alert Bay volcanic belt; GVB: Garibaldi volcanic belt; QCF: Queen Charlotte fault.

Fig. 2. Field photographs of the mantle xenoliths. (a) Dunite; (b–e) Lherzolite; and (f) Pyroxenite. Lherzolite in photograph (e) includes pyroxene and spinel-rich bands. Photographs (b) and (e) are from Friedman et al. (2016). Length of the pen is 15 cm and diameter of the loonie is 2.65 cm.

Fig. 3. (a–f) Photomicrographs of the mantle xenoliths showing triple junctions (a–c), olivine deformation lamellae (dl) (b, d and e), melt pocket (f), and trails of melt/fluid inclusions. ol: olivine; opx: orthopyroxene; cpx: clinopyroxene; mp: melt pocket; ti: trail of melt/fluid inclusions.

Fig. 4. (a–f) Photomicrographs of the mantle xenoliths showing melt pockets (a, b), spongy cpx texture (c, d), and trails of melt/fluid inclusions (e, f). ol: olivine; opx: orthopyroxene; cpx: clinopyroxene; sp: spinel; mp: melt pocket; ti: trail of melt/fluid inclusions; s-cpx: spongy cpx.

Fig. 5. (a–f) SEM–BSE images of feldspar veins in the mantle xenoliths. Photographs (d) and (e) indicate that melts in the veins reacted mainly with opx to form melt pockets. ol: olivine; opx: orthopyroxene; cpx2: Type 2 clinopyroxene; sp: spinel; feld1: Type 1 feldspar; feld2: Type 2 feldspar; feld4: Type 4 feldspar. Melt pockets are outlined with red dashed lines.

Fig. 6. (a–f) SEM–BSE images of melt pockets in the mantle xenoliths. Olivine exhibits rounded (b) to skeletal (c) crystal shapes. Trails of melts in images (a–d) are consistent with their

migration to the melt pockets. Image (f) shows that a new melt pocket formed after an older melt pocket. ol: olivine; opx: orthopyroxene; cpx1: Type 1 clinopyroxene; cpx2: Type 2 clinopyroxene; sp: spinel; sk-ol: skeletal olivine; feld1: Type 1 feldspar; feld2: Type 2 feldspar; feld3: Type 3 feldspar; feld4: Type 4 feldspar. Melt pockets are outlined with red dashed lines.

Fig. 7. (a–f) SEM–BSE images of melt pockets in the mantle xenoliths. Image (a) shows that melt pockets are connected along grain boundaries. Olivine exhibits anhedral, skeletal crystal shapes and contains feldspar inclusions (b–c). Olivine and feldspar are replaced by cpx2 (a, f). Image (f) shows the preservation of a vug in the melt pocket. ol: olivine; opx: orthopyroxene; cpx1: Type 1 clinopyroxene; cpx2: sk-ol: skeletal olivine; Type 2 clinopyroxene; feld1: Type 1 feldspar; feld2: Type 2 feldspar; feld3: Type 3 feldspar; feld4: Type 4 feldspar.

Fig. 8. (a–f) SEM–BSE images of spongy cpx texture in the mantle xenoliths. Cpx grains in images (a–d) are characterized by a distinct "core and rim" structure; cpx grains in images (e and f) are totally overprinted by the spongy texture. ol: olivine; opx: orthopyroxene; cpx1: Type 1 clinopyroxene; cpx2: Type 2 clinopyroxene; feld1: Type 1 feldspar; feld2: Type 2 feldspar; feld3: Type 3 feldspar; feld4: Type 4 feldspar.

Fig. 9. (a–f) SEM–BSE images of spongy cpx texture and its spatial relationship with feldspar in the mantle xenoliths. Spongy cpx grains are connected by either vein or intergranular feldspar. Images (c, e, and d) show formation of olivine at the expense of opx, and the replacement of feldspar and olivine by cpx2. ol: olivine; opx: orthopyroxene; cpx1: Type 1 clinopyroxene; cpx2: Type 2 clinopyroxene; feld1: Type 1 feldspar; feld2: Type 2 feldspar; feld3: Type 3 feldspar; feld4: Type 4 feldspar.

Fig. 10. (a–f) SEM–BSE images of the contacts between the mantle xenoliths and host alkaline basalt. ol: olivine; opx: orthopyroxene; cpx: clinopyroxene; cpx1: Type 1 clinopyroxene; cpx2: Type 2 clinopyroxene; feld1: Type 1 feldspar; mp: melt pocket; plg: plagioclase; mg: Ti-rich magnetite. Blue dashed lines mark the possible limits of pyrometamorphism. Red lines show the boundaries of former melt pockets.

Fig. 11. (a) $^{87}Sr/^{86}Sr$ versus $^{143}Nd/^{144}Nd$, (b) $^{206}Pb/^{204}Pb$ versus $^{143}Nd/^{144}Nd$, and (c) $^{206}Pb/^{204}Pb$ versus $^{87}Sr/^{86}Sr$, and (d) $^{206}Pb/^{204}Pb$ versus $^{208}Pb/^{204}Pb$ plots for the mantle xenoliths and host alkaline basalts. Data for the basalts are from Friedman et al. (2016). DMM (Depleted MORB mantle), EM1 (Enriched mantle 1), EM2 (Enriched mantle 2) and HIMU (high-μ, with $\mu = {}^{238}U/^{204}Pb$) fields are from Hofmann (1997) and Starcke et al. (2005).

Fig. 12. (a) $\delta^{18}O$-olivine (‰) versus $\delta^{18}O$-cpx, (b) $\delta^{18}O$-cpx (‰) versus $\delta^{18}O$-opx, (c) $\delta^{18}O$-olivine (‰) versus $\delta^{18}O$-opx, and (d) $\delta^{18}O$-opx (‰) versus $\delta^{18}O$-spinel (modified from Perkins et al., 2006 and Hao et al., 2015). The equilibrium line in (a) and (b) represents results for spinel lherzolite xenoliths worldwide (Mattey et al., 1994).

Fig. 13. N-MORB-normalized trace element diagrams for Groups 1, 2 and 3 mantle xenoliths Data are from Friedman et al. (2016). Normalization values are from Sun and McDonough (1989).

Fig. 14. N-MORB-normalized trace element diagrams for the outlier mantle xenolith samples and host alkaline basalts. Data are from Friedman et al. (2016). Normalization values are from Sun and McDonough (1989).

Fig. 15. Schematic cross section of southern Canadian Cordillera showing Tasse volcanic locality in context of main tectonic features and possible processes contributing to Late Cenozoic magmatism. Explorer plate is stagnant and thermally eroding. Decompressional melting of asthenosphere and affected lithospheric mantle drives majority of magmatism. Transient tension facilitates magma ascent. Thinning of lithospheric mantle by thermal erosion, convective removal and delamination likely contribute to absence of thick lithospheric mantle beneath most of the Cordillera. Archean source regions for some Tasse mantle xenoliths may include in-situ Archean SCLM and asthenosphere-transported rafts from more easterly locations. Cross section line is shown on Fig. 1b. Some volcanic fields shown in Fig. 1b have been projected onto cross section. ABVB: Alert Bay volcanic belt; AVB : Anahim volcanic belt; GVB: Garibaldi volcanic belt; CG: Chilcotin Group; WGVB: Wells Gray volcanic belt; SCLM: sub-continental lithospheric mantle.

Figure 1

Click here to download high resolution image

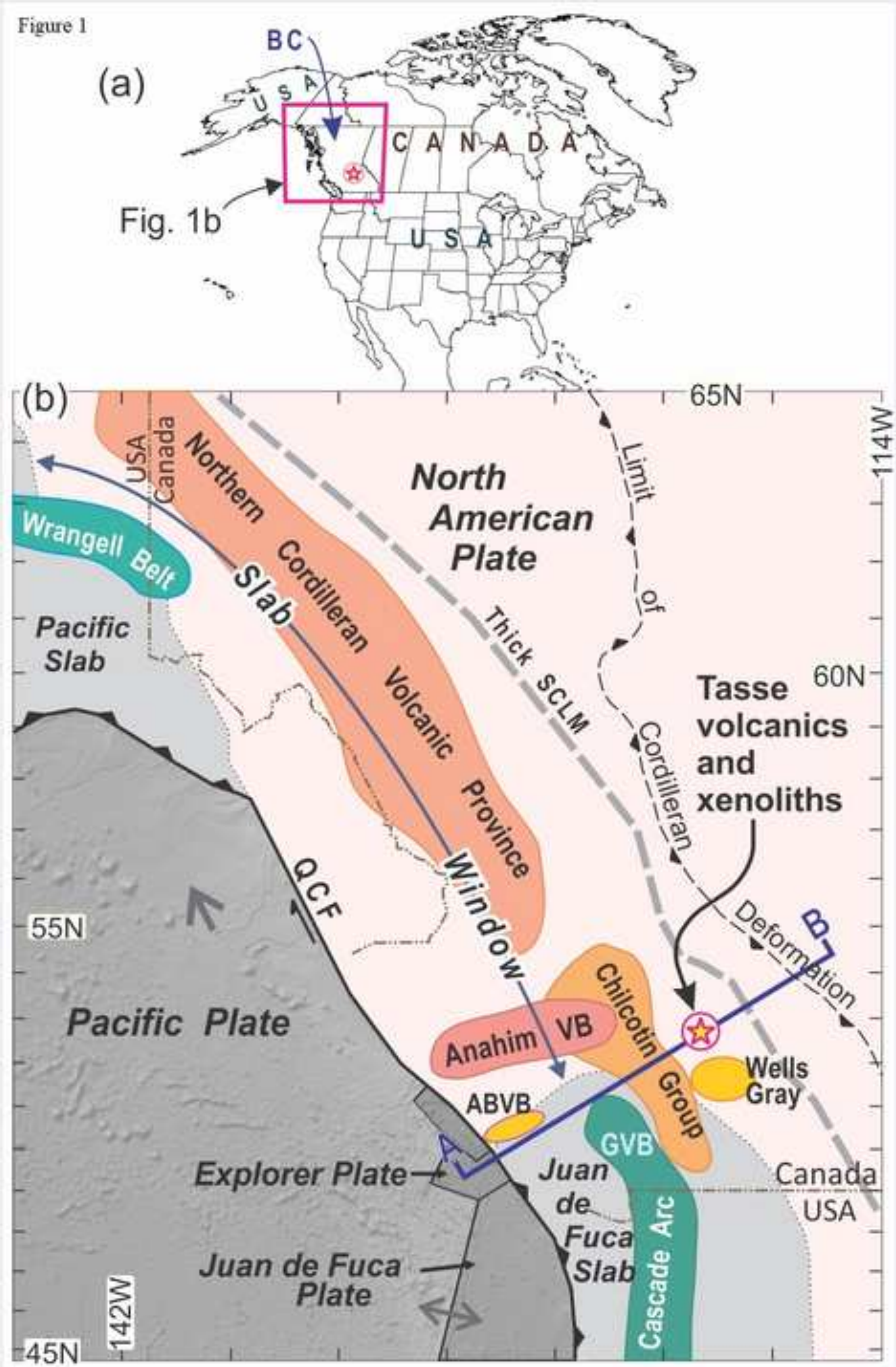

Figure 2

Figure 2

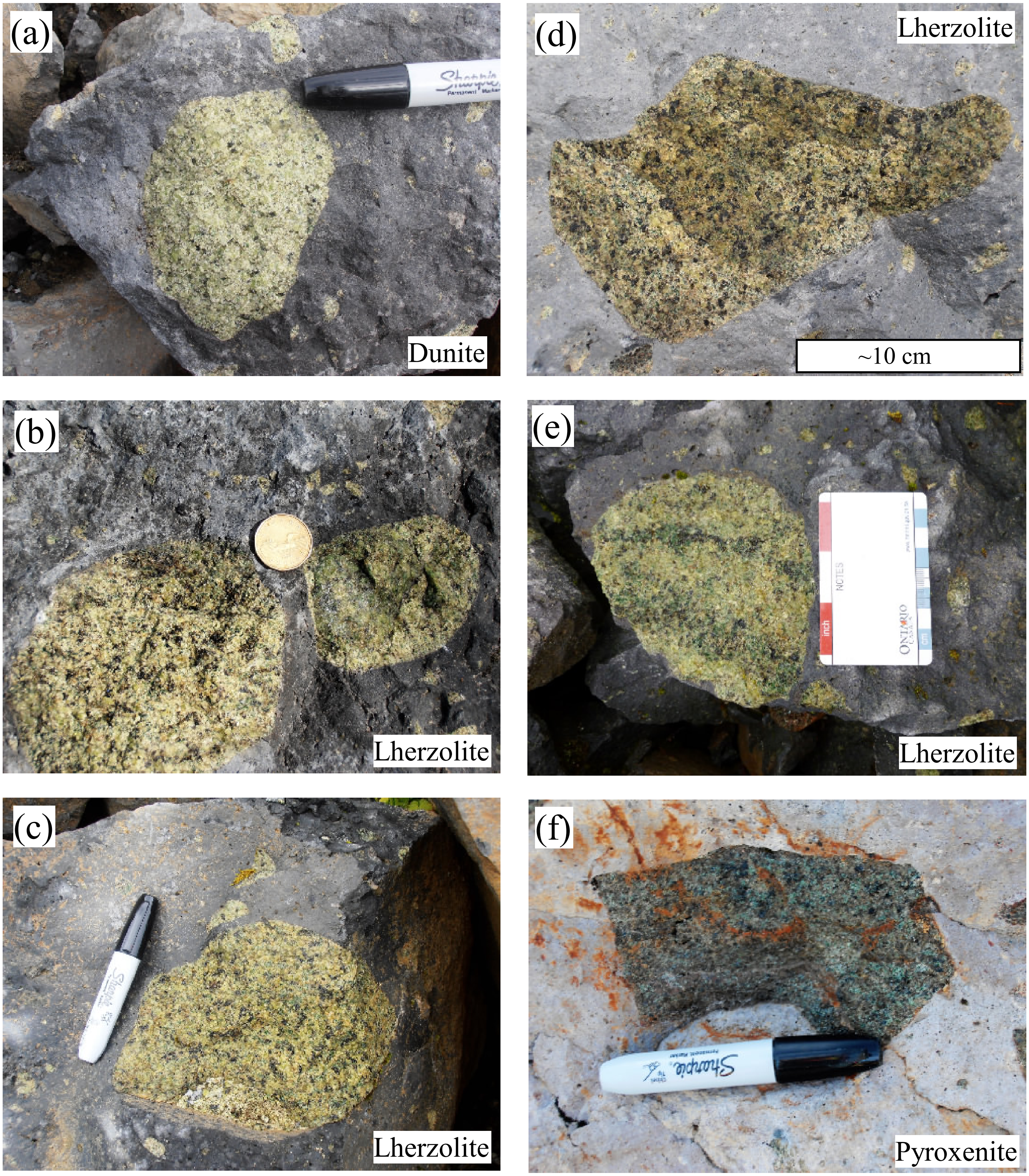

Figure 3

Figure 3

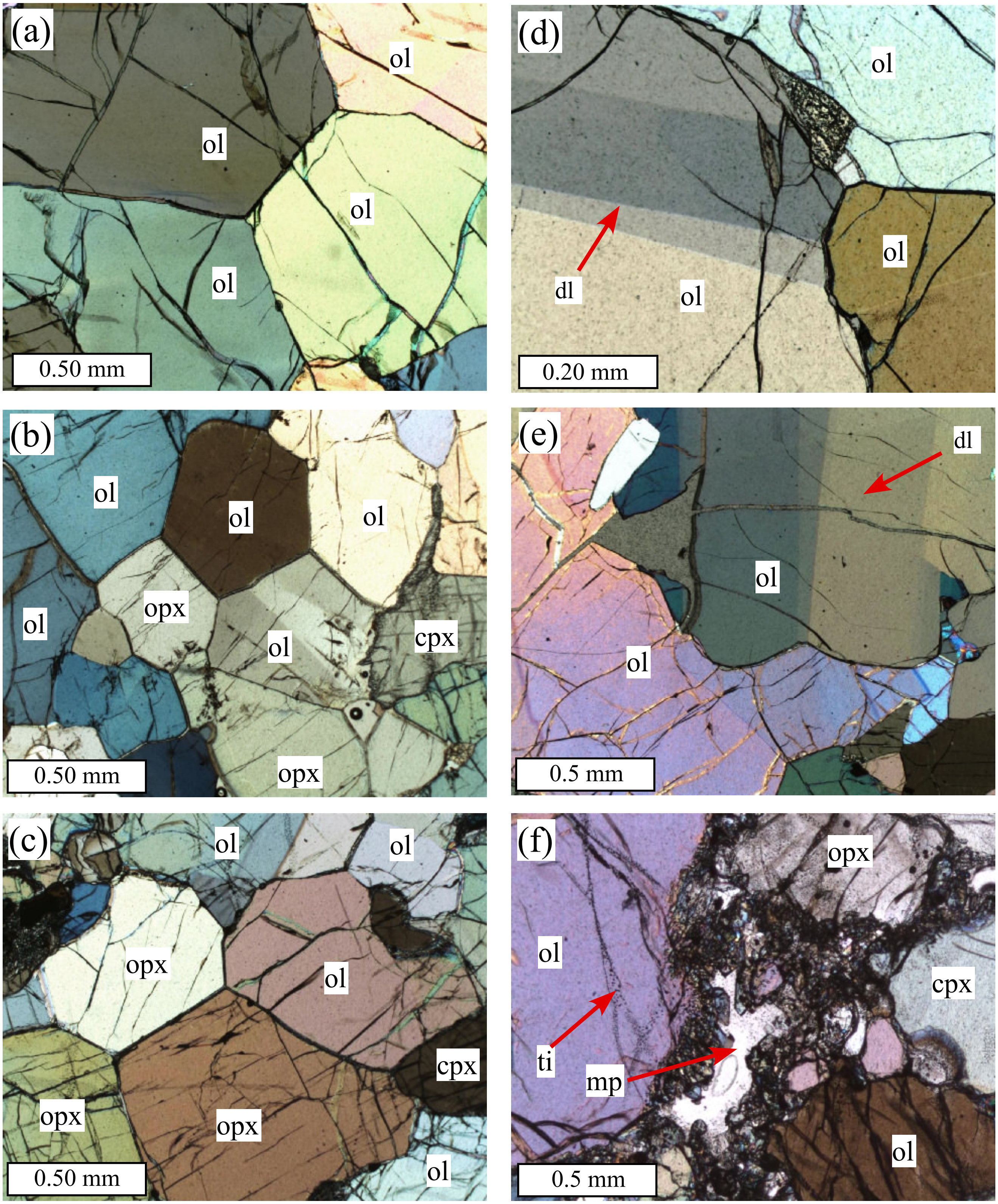

Figure 4

Figure 4

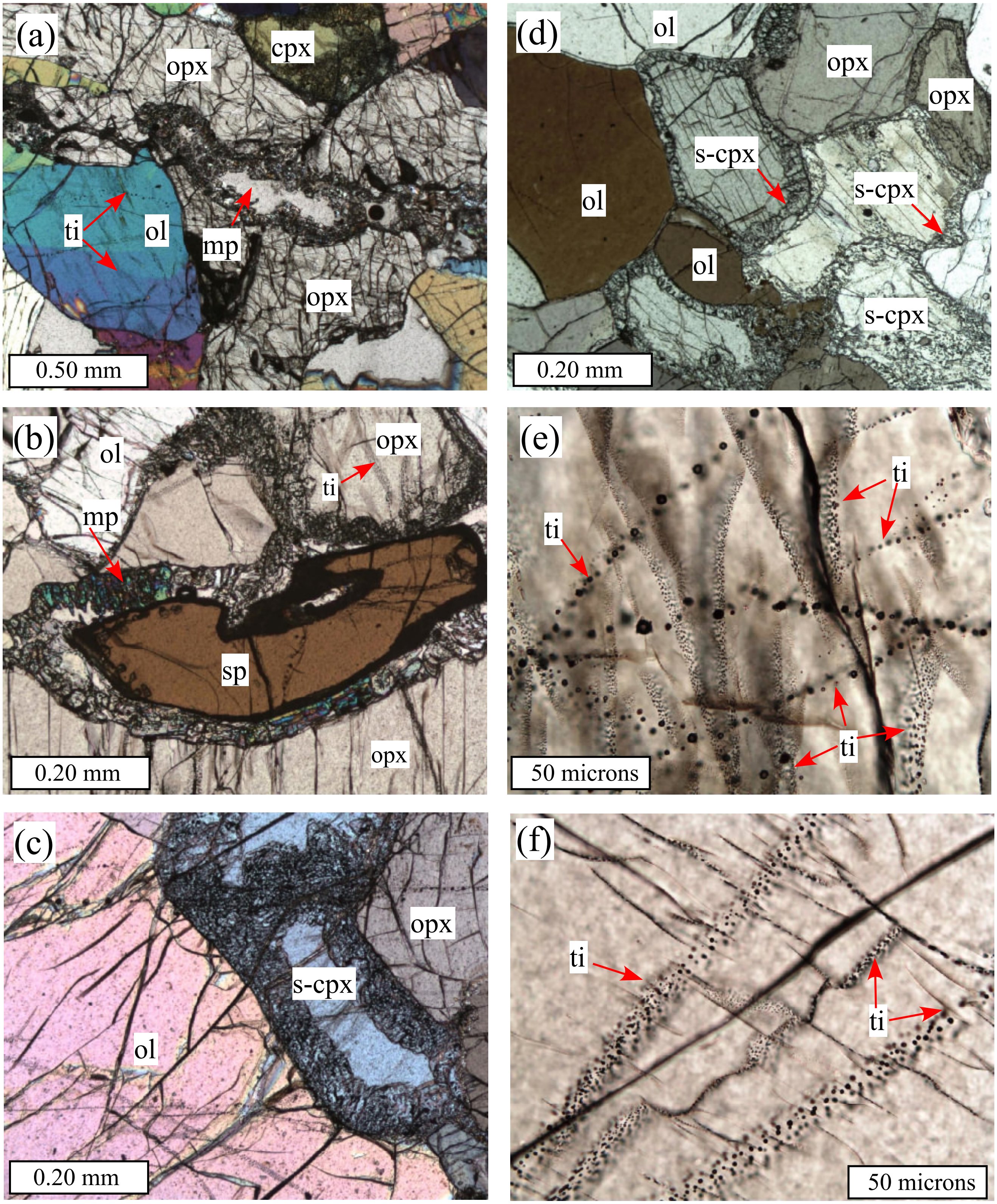

Figure 5

Figure 5

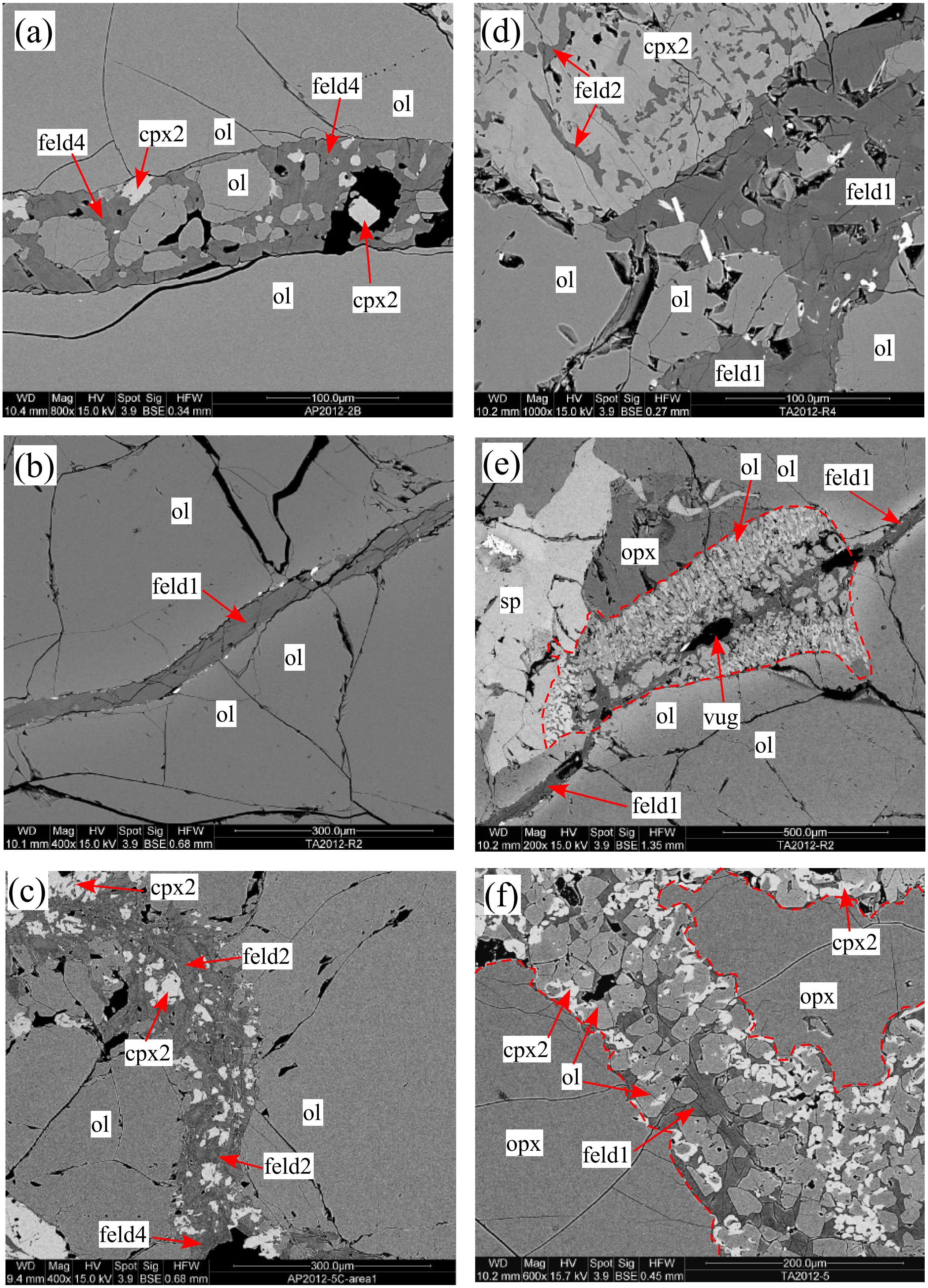

Figure 6

Figure 6

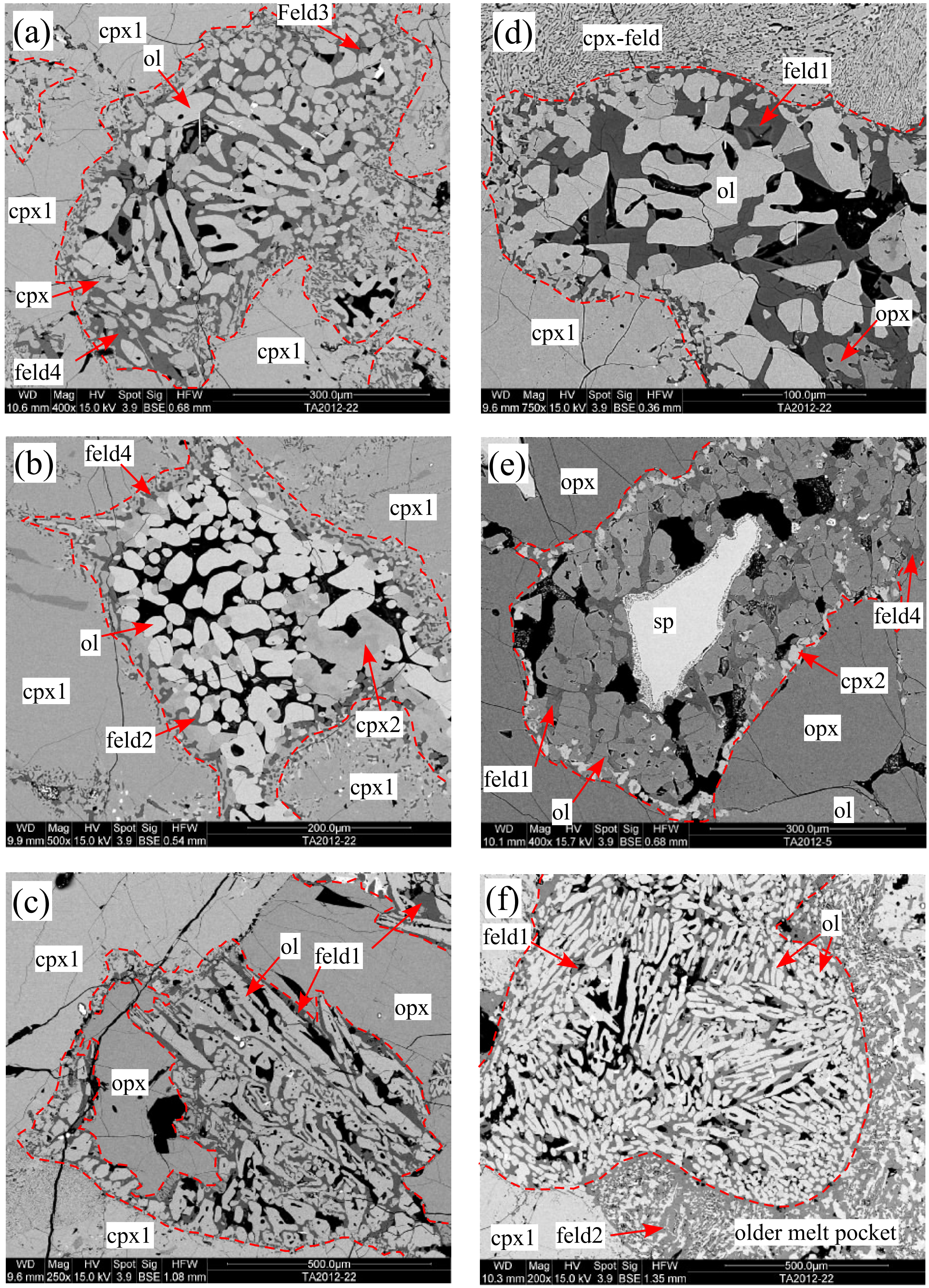

Figure 7

Figure 7

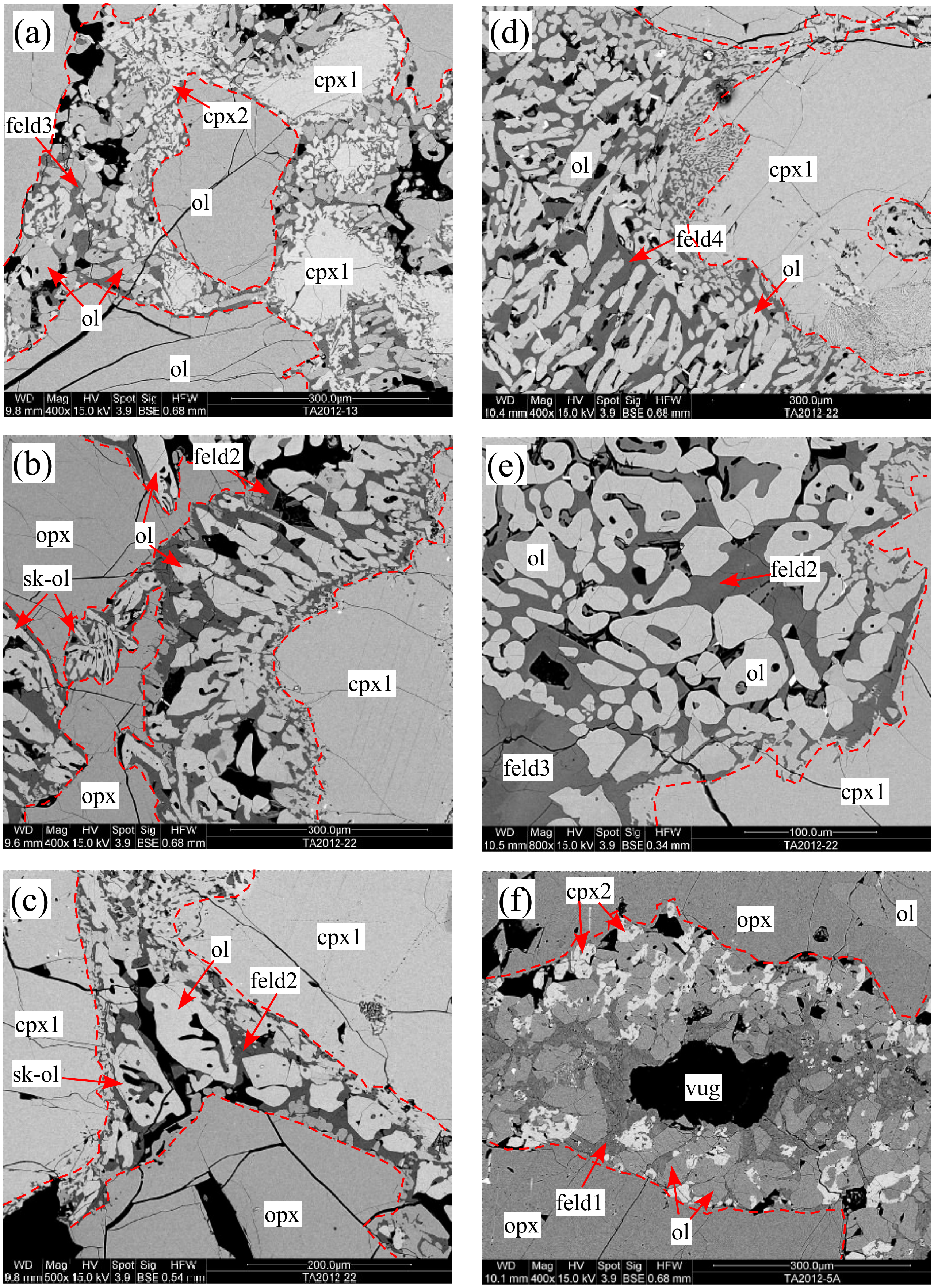

Figure 8

Figure 8

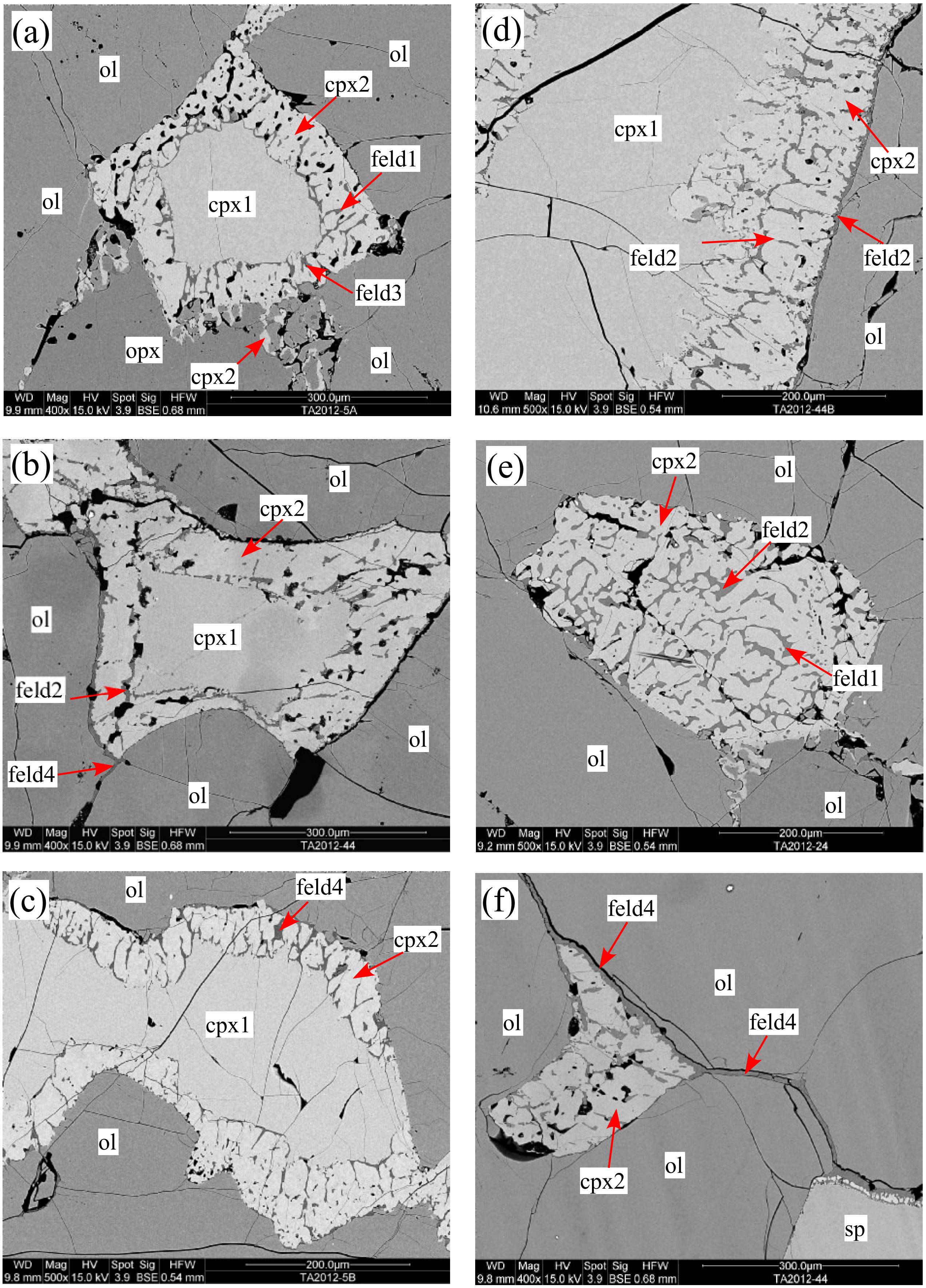

Figure 9

Figure 9

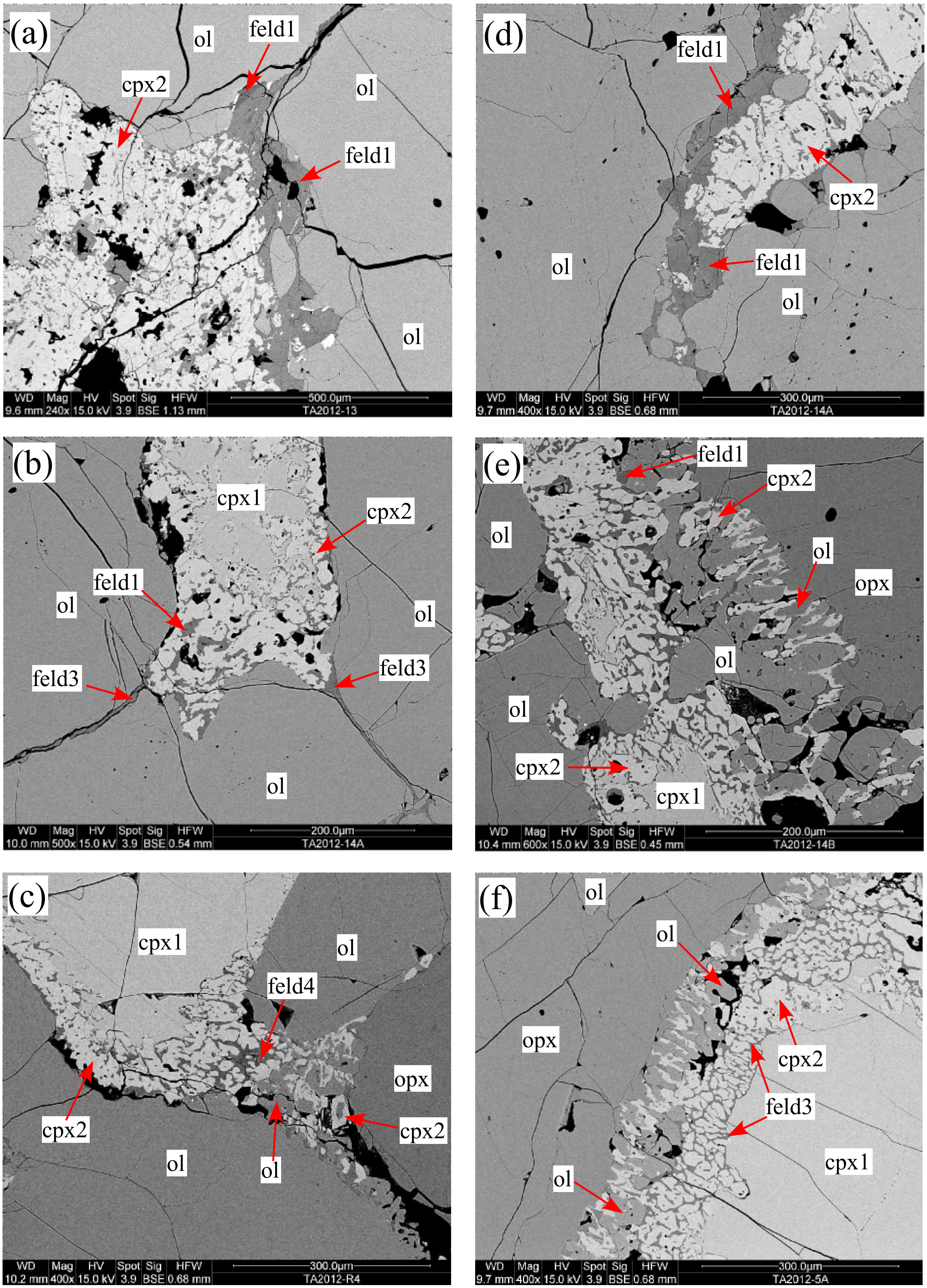

Figure 10

Figure 10

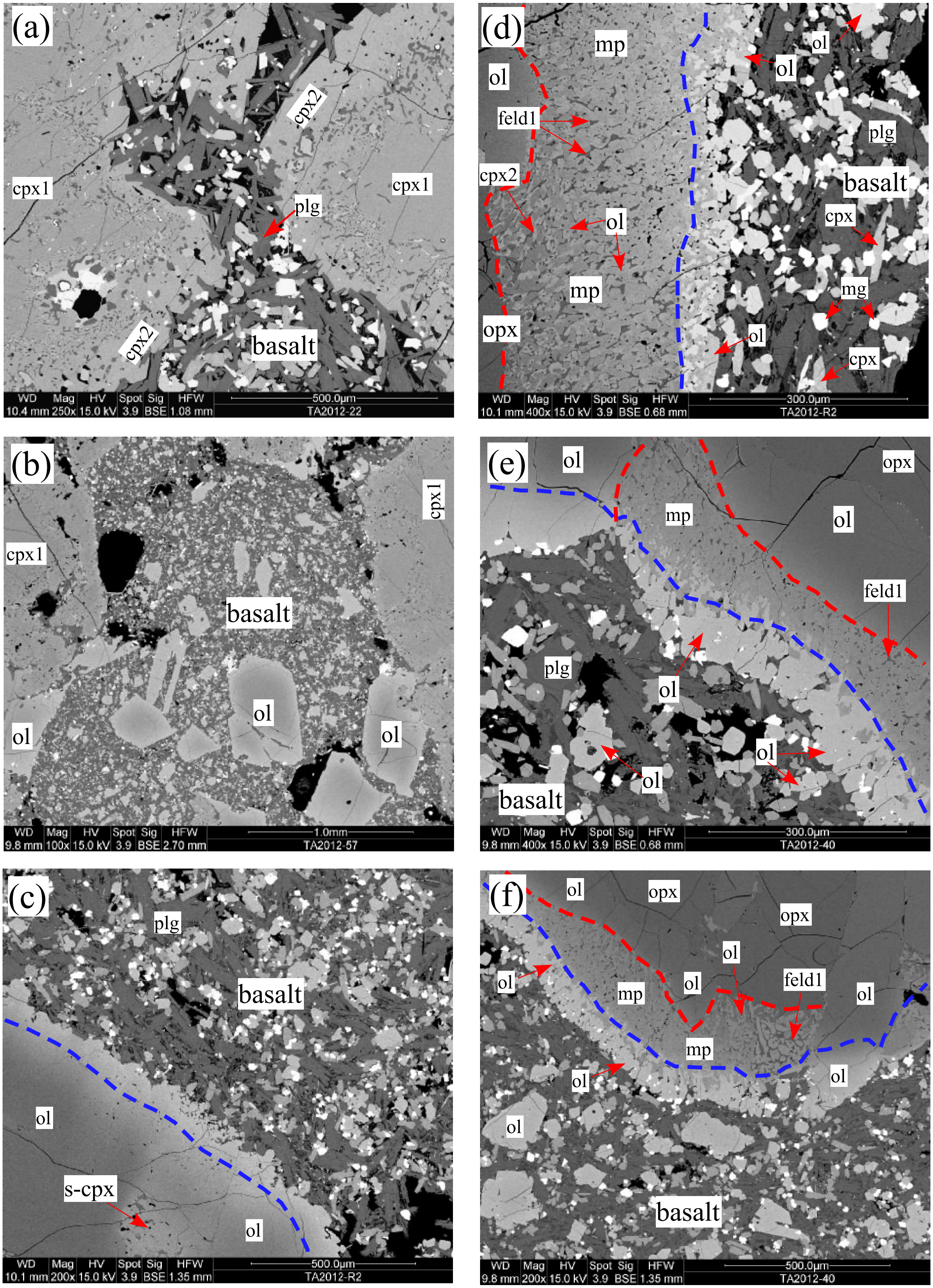

Figure 11

Figure 11

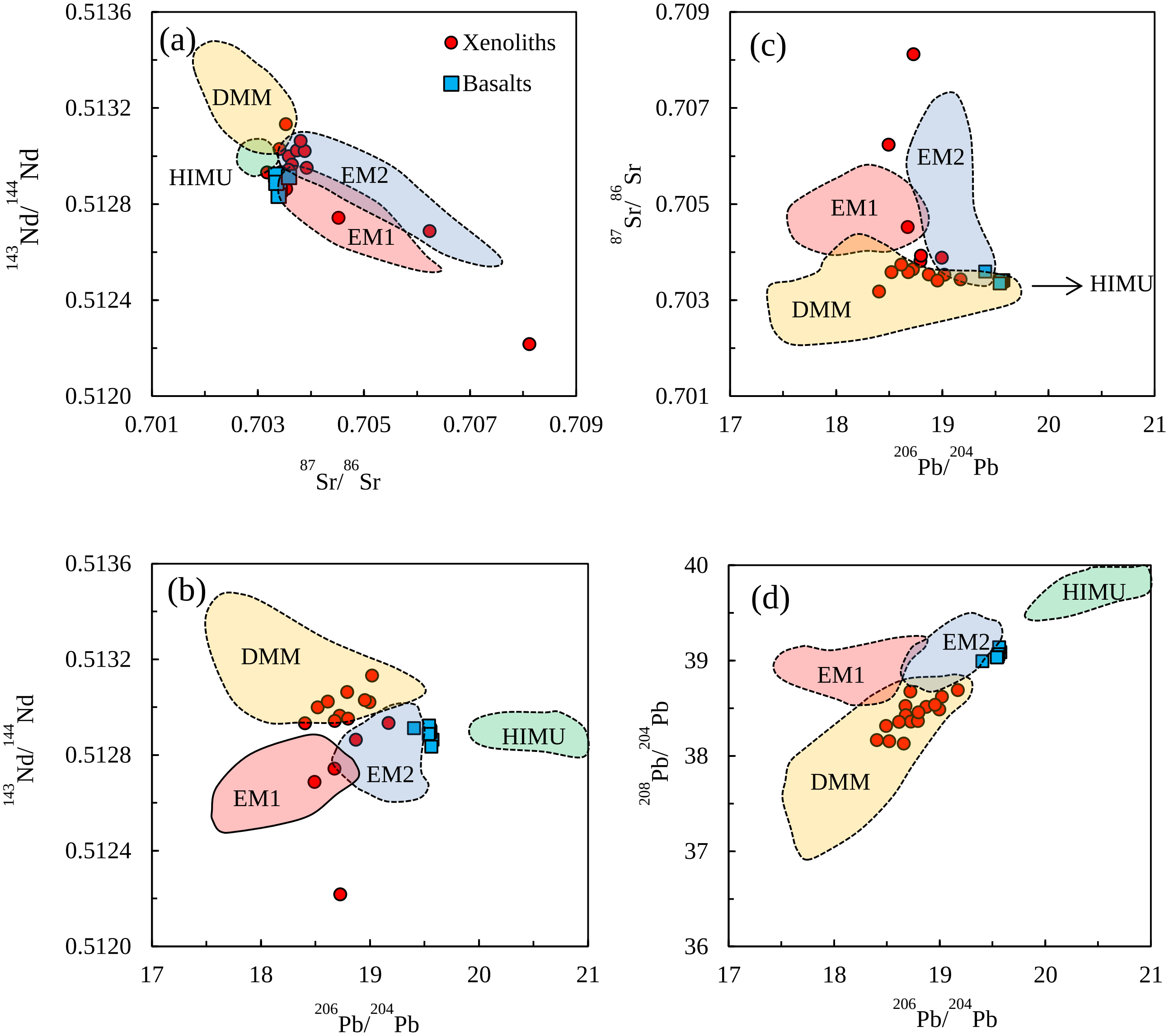

Figure 12

Figure 12

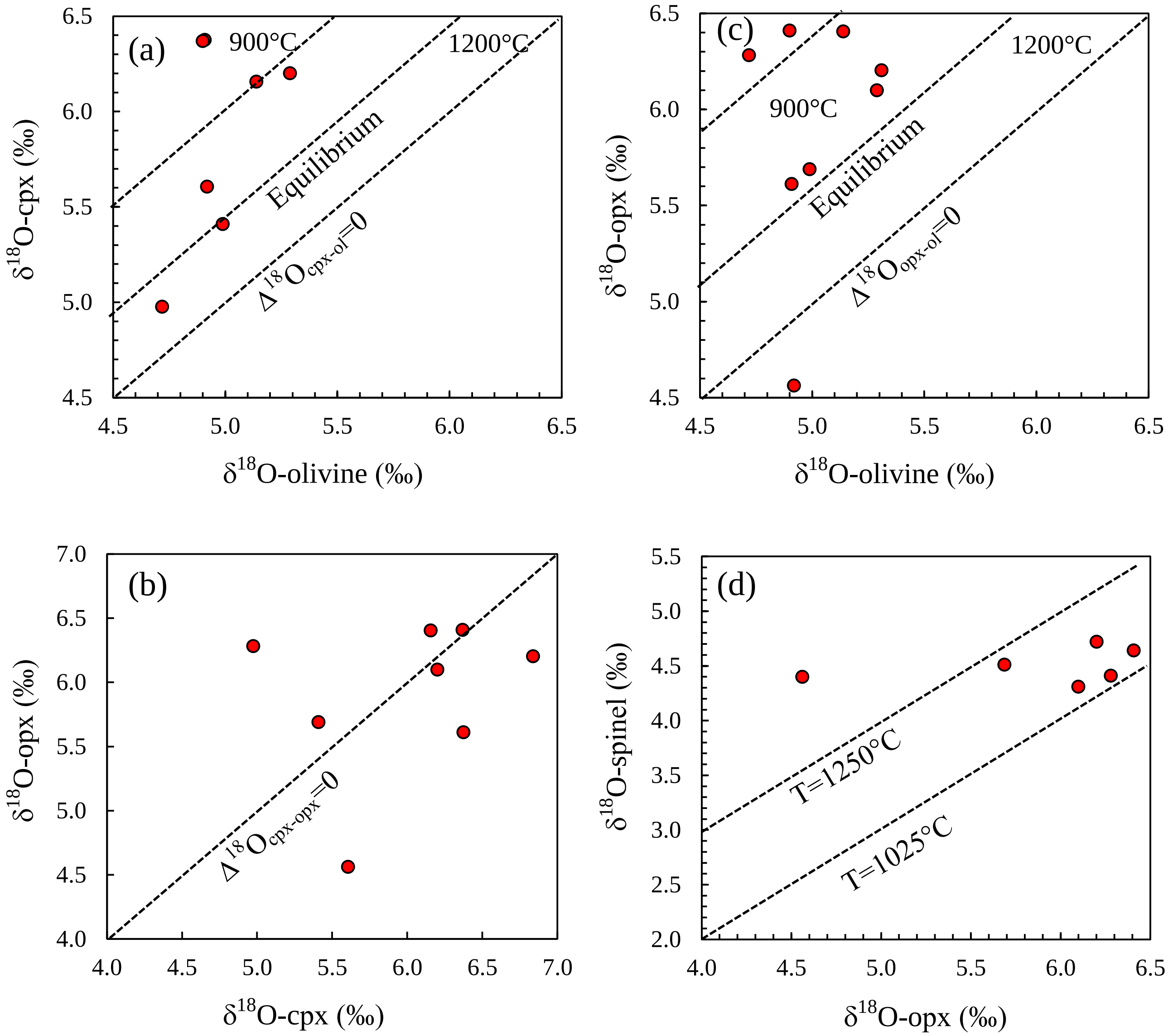

Figure 13

Figure 13

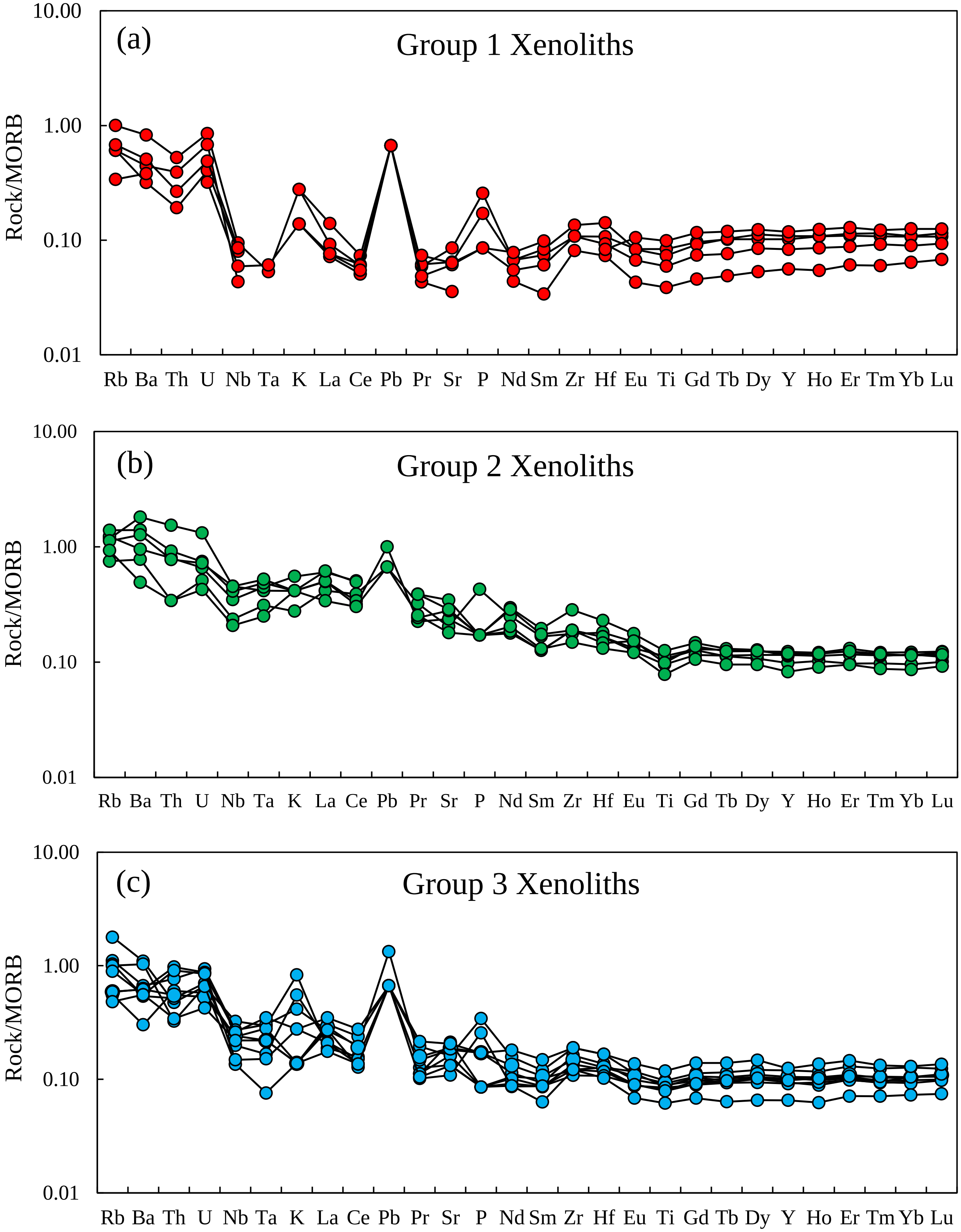

Figure 14

Figure 14

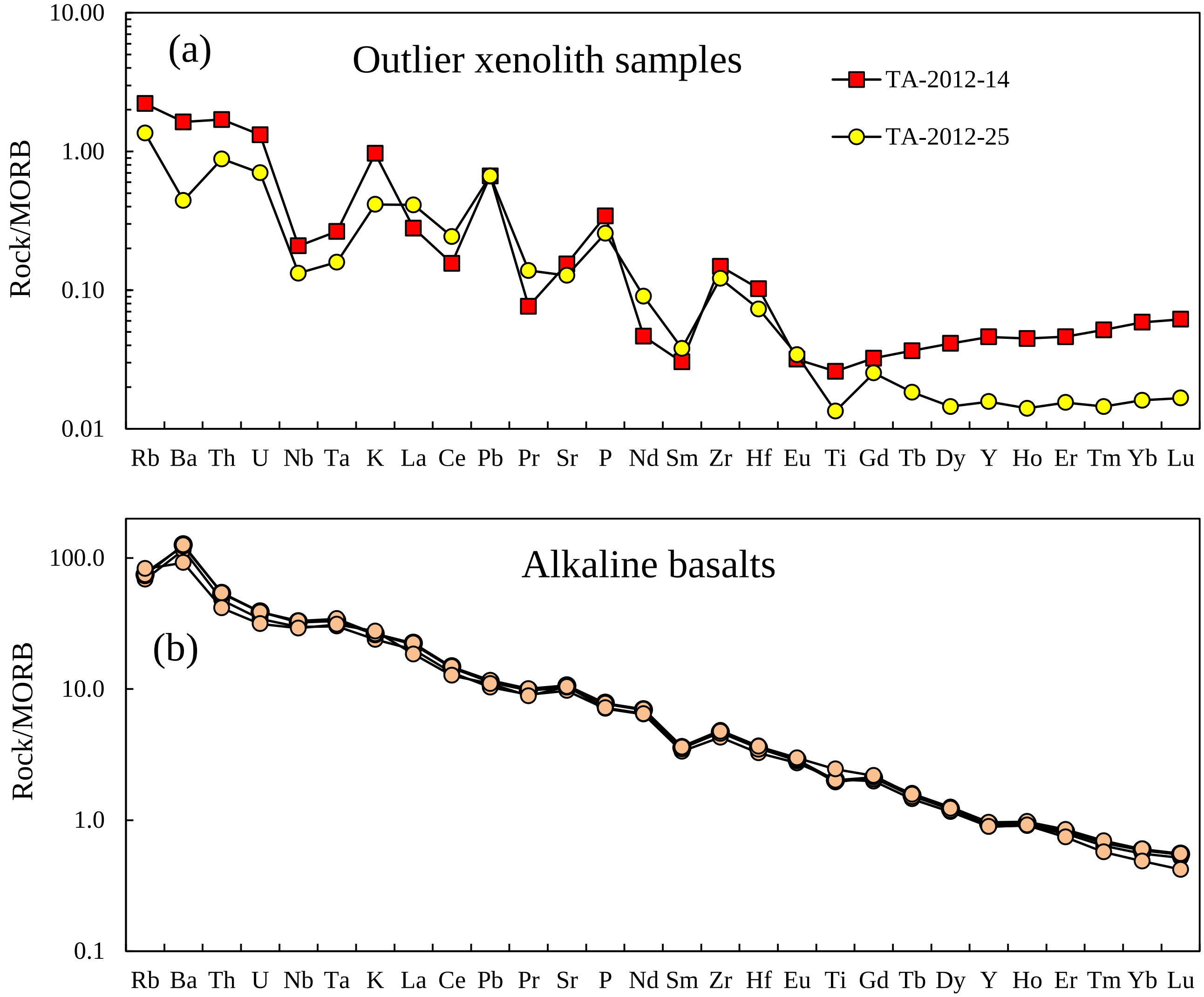

Figure 15

Click here to download high resolution image

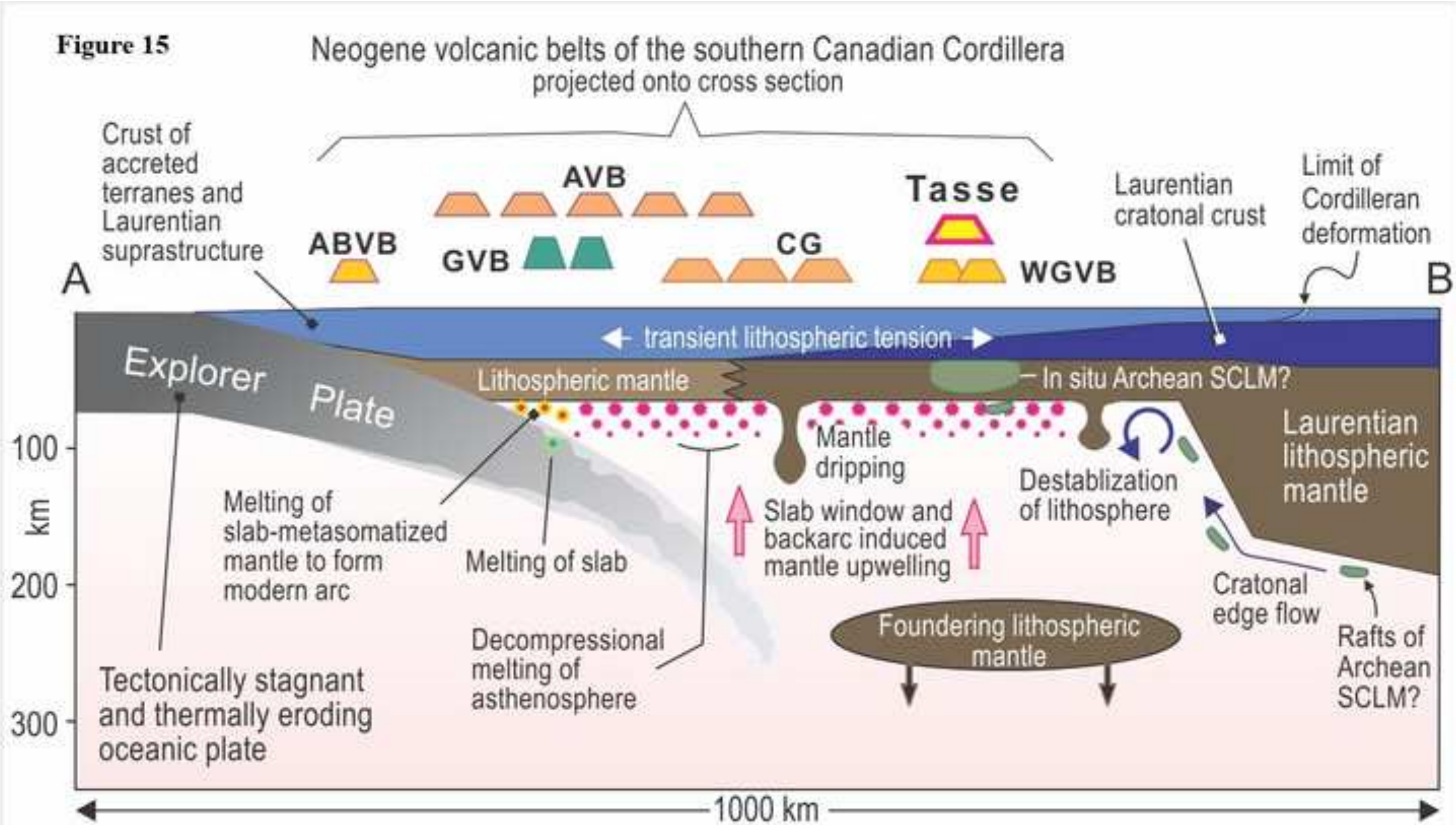

Appendix A: Scanning Electron Microscope - Energy Dispersive Spectroscopy (SEM-EDS) analyses of olivine (n=219) in the Tasse mantle xenoliths.

	Type 1 olivine (n=205)			
Sample-spot	MgO (wt.%)	SiO_2 (wt.%)	FeO (wt.%)	Mg-number
TA2012-1-1	49.8	39.7	10.5	93.4
TA2012-1-2	49.8	39.9	10.2	93.7
TA2012-1-3	50.2	40.2	9.6	94.4
TA2012-2-1	49.2	40.5	10.3	93.5
TA2012-2-2	49.7	40.0	10.2	93.7
TA2012-2-3	49.5	39.9	10.6	93.3
TA2012-3-4	49.9	40.2	10.0	93.9
TA2012-4-1	50.5	40.0	9.5	94.5
TA2012-5-1	50.5	40.0	9.6	94.4
TA2012-5-2	50.8	39.4	9.8	94.2
TA2012-5-3	50.4	40.1	9.5	94.5
TA2012-5-4	50.4	40.0	9.6	94.4
TA2012-5-5	50.5	39.5	10.0	94.0
TA2012-5-6	50.5	39.9	9.6	94.4
TA2012-5-7	50.3	39.3	10.4	93.6
TA2012-5-8	50.3	39.6	10.1	93.9
TA2012-5-9	50.5	40.1	9.5	94.5
TA2012-5-10	50.0	40.2	9.8	94.1
TA2012-5-11	50.1	40.4	9.5	94.4
TA2012-5-12	50.4	39.9	9.7	94.3
TA2012-5-13	49.7	40.0	10.3	93.6
TA2012-5-14	50.1	40.5	9.4	94.5
TA2012-5-15	49.9	40.4	9.7	94.2
TA2012-5-16	50.0	40.6	9.4	94.5
TA2012-5-17	50.1	39.8	10.1	93.9

TA2012-5-18	49.9	40.1	10.0	93.9
TA2012-5-19	50.2	40.1	9.7	94.3
TA2012-5-20	50.3	40.1	9.6	94.4
TA2012-5-21	50.1	40.3	9.6	94.3
TA2012-5-22	50.3	40.2	9.5	94.5
TA2012-5-23	50.4	40.1	9.5	94.5
TA2012-13-1	50.1	39.9	10.0	93.9
TA2012-13-2	50.1	40.1	9.9	94.1
TA2012-14-1	50.4	40.1	9.4	94.5
TA2012-15-1	49.9	40.1	10.0	94.0
TA2012-15-2	49.9	40.0	10.1	93.9
TA2012-15-3	49.8	39.9	10.3	93.6
TA2012-15-4	49.4	40.0	10.7	93.2
TA2012-15-5	49.9	40.3	9.8	94.1
TA2012-15-6	49.9	39.7	10.5	93.5
TA2012-15-7	49.7	39.9	10.4	93.5
TA2012-15-8	49.6	40.1	10.4	93.5
TA2012-15-9	50.0	40.1	10.0	93.9
TA2012-15-10	49.6	40.2	10.2	93.7
TA2012-15-11	49.6	40.2	10.2	93.7
TA2012-16-1	50.2	40.1	9.7	94.3
TA2012-16-2	49.8	39.9	10.3	93.6
TA2012-16-3	50.0	40.0	10.0	94.0
TA2012-16-4	48.7	40.7	10.5	93.2
TA2012-16-5	49.9	40.1	10.0	93.9
TA2012-16-6	50.2	40.0	9.8	94.1
TA2012-16-7	49.5	40.4	10.2	93.7
TA2012-16-7	49.9	40.2	9.9	94.0
TA2012-17-1	50.1	40.2	9.7	94.2

TA2012-17-2	49.6	39.8	10.6	93.3
TA2012-17-3	50.1	40.2	9.7	94.2
TA2012-17-4	50.2	39.9	10.0	94.0
TA2012-17-5	50.4	40.2	9.5	94.5
TA2012-17-6	49.8	40.4	9.4	94.4
TA2012-18-1	50.2	40.2	9.6	94.4
TA2012-18-1	50.3	40.1	9.5	94.4
TA2012-18-2	50.4	40.2	9.5	94.5
TA2012-21-1	49.9	40.2	10.0	93.9
TA2012-44-1	50.3	40.2	9.4	94.5
TA2012-44-2	50.4	40.0	9.6	94.4
TA2012-44-3	49.8	40.4	9.9	94.0
TA2012-44-4	49.8	40.5	9.7	94.2
TA2012-44-5	50.3	40.1	9.7	94.3
TA2012-44-6	49.6	40.1	10.2	93.6
TA2012-44-7	50.2	40.1	9.7	94.3
TA2012-44-8	50.3	40.2	9.5	94.5
TA2012-44-9	50.1	40.0	9.9	94.0
TA2012-44-10	50.2	40.2	9.6	94.4
TA2012-44-11	50.1	40.2	9.7	94.2
TA2012-44-12	50.2	40.3	9.6	94.4
TA2012-44-13	50.3	40.0	9.7	94.3
TA2012-44-14	50.0	40.1	10.0	93.9
TA2012-44-15	50.5	40.0	9.6	94.4
TA2012-44-16	50.1	40.4	9.5	94.5
TA2012-44-17	50.1	40.3	9.5	94.4
TA2012-44-18	50.7	39.8	9.6	94.5
TA2012-44-19	49.7	39.9	10.5	93.4
TA2012-44-20	49.7	40.2	10.1	93.8

TA2012-44-21	50.3	40.2	9.6	94.4
TA2012-44-22	50.3	40.1	9.6	94.3
TA2012-44-23	50.2	40.0	9.7	94.2
TA2012-44-24	50.5	40.0	9.6	94.5
TA2012-44-25	50.2	40.4	9.5	94.5
TA2012-44-26	50.4	40.0	9.6	94.4
TA2012-44-27	49.8	40.1	10.0	93.9
TA2012-44-28	49.6	40.2	10.3	93.6
TA2012-44-29	49.6	40.6	9.8	94.0
TA2012-44-30	49.8	40.4	9.8	94.1
TA2012-44-31	49.8	40.4	9.8	94.1
TA2012-44-32	50.0	40.0	10.1	93.9
TA2012-44-33	49.8	40.2	10.0	93.9
TA2012-44-34	49.4	40.0	10.6	93.3
TA2012-44-35	49.8	40.0	10.2	93.7
TA2012-44-36	49.4	40.3	10.3	93.6
TA2012-44-37	49.5	40.2	10.4	93.5
TA2012-44-38	49.6	40.2	10.1	93.7
TA2012-46-1	49.8	40.2	10.1	93.8
TA2012-46-2	49.8	40.3	9.9	94.0
TA2012-46-3	50.0	39.8	10.2	93.8
TA2012-46-4	50.1	40.0	9.9	94.0
TA2012-46-5	50.1	39.8	10.2	93.8
TA2012-55-1	50.1	40.2	9.8	94.2
TA2012-55-2	49.9	40.4	9.7	94.2
TA2012-55-3	50.0	40.2	9.9	94.1
TA2012-55-4	50.0	39.8	10.2	93.7
TA2012-55-5	50.0	40.1	10.0	94.0
TA2012-R2-1	48.6	39.9	11.5	92.2

TA2012-R2-2	49.7	40.1	10.3	93.6
TA2012-R2-3	47.9	39.5	12.6	91.1
TA2012-R2-4	47.0	39.4	13.6	89.9
TA2012-R2-5	47.7	39.4	13.0	90.6
TA2012-R2-6	48.8	39.9	11.3	92.5
TA2012-R2-7	49.8	40.0	10.3	93.6
TA2012-R2-8	49.5	40.3	10.2	93.7
TA2012-R2-9	47.2	39.8	13.0	90.5
TA2012-R2-10	50.0	39.8	10.2	93.8
TA2012-R2-11	49.5	40.0	10.5	93.3
TA2012-R2-12	49.5	40.3	10.2	93.6
TA2012-R2-13	50.1	39.9	10.1	93.9
TA2012-R2-14	49.8	39.9	10.3	93.6
TA2012-R2-15	50.1	39.9	10.0	93.9
TA2012-R2-16	49.8	39.9	10.3	93.6
TA2012-R2-17	49.2	39.8	11.0	92.8
TA2012-R2-18	50.0	39.9	10.1	93.8
TA2012-R2-19	50.3	40.2	9.6	94.4
TA2012-R2-20	49.9	40.4	9.7	94.2
TA2012-R2-21	50.2	40.2	9.6	94.4
TA2012-R2-22	48.5	40.3	11.3	92.4
TA2012-R2-23	46.7	39.8	13.5	89.9
TA2012-R2-24	47.4	39.4	13.2	90.4
TA2012-R2-25	47.2	39.6	13.3	90.3
TA2012-R2-26	47.2	39.1	13.7	89.9
TA2012-R2-27	50.6	39.9	9.6	94.5
TA2012-R2-28	50.1	40.5	9.4	94.5
TA2012-R4-1	49.9	39.9	10.2	93.7
TA2012-R4-2	49.7	39.9	10.5	93.4

TA2012-R4-3	49.6	39.9	10.5	93.4
TA2012-R4-4	49.5	40.1	10.5	93.4
TA2012-R4-5	49.7	40.4	9.9	94.0
TA2012-R4-6	49.6	40.0	10.4	93.5
TA2012-R4-7	49.9	39.8	10.3	93.7
AP2012-2B-1	50.6	39.7	9.7	94.3
AP2012-2B-2	50.3	40.2	9.5	94.4
AP2012-2B-3	50.4	39.9	9.7	94.3
AP2012-2B-4	50.4	39.7	9.9	94.1
AP2012-4-1	49.1	39.4	11.5	92.3
AP2012-4-2	49.3	39.2	11.5	92.4
AP2012-4-3	49.9	39.6	10.4	93.5
AP2012-4-4	49.8	39.6	10.6	93.3
AP2012-4-5	49.5	39.5	11.0	92.9
AP2012-4-6	49.8	39.2	11.1	92.9
AP2012-5A-1	49.9	39.6	10.5	93.5
AP2012-5A-2	49.4	39.9	10.0	93.8
AP2012-5A-3	50.3	39.5	10.2	93.8
TA2012-5B-4	47.7	39.0	13.3	90.3
TA2012-5B-5	46.0	38.8	15.3	88.1
TA2012-5B-6	47.9	38.7	13.3	90.4
TA2012-5B-7	48.1	38.7	13.2	90.5
TA2012-5B-8	47.7	38.8	13.5	90.2
TA2012-5B-9	48.0	39.4	12.7	91.0
TA2012-5B-10	47.9	39.1	13.0	90.7
TA2012-5B-11	48.2	39.4	12.4	91.3
TA2012-14A-1	50.5	39.8	9.7	94.3
TA2012-14A-2	50.1	40.0	10.0	94.0
TA2012-14A-3	50.7	39.6	9.7	94.4

TA2012-15-1	50.6	39.6	9.7	94.3
TA2012-15-2	50.1	39.4	9.9	94.0
TA2012-15-3	48.8	40.7	10.0	93.7
TA2012-15-4	50.6	39.6	9.9	94.2
TA2012-15-5	50.6	39.7	9.6	94.4
TA2012-24-1	49.5	40.6	9.6	94.2
TA2012-44A-1	50.8	39.7	9.5	94.5
TA2012-44B-1	50.6	39.9	9.5	94.5
TA2012-44B-2	50.6	39.6	9.8	94.3
TA2012-44B-3	50.6	39.9	9.5	94.5
TA2012-44B-4	50.4	40.0	9.6	94.4
TA2012-44B-5	49.6	39.6	10.8	93.1
TA2012-44B-6	49.9	39.9	10.2	93.7
TA2012-44B-7	49.9	39.6	10.5	93.4
TA2012-44B-8	49.6	39.6	10.8	93.1
TA2012-48-1	47.9	39.3	12.8	90.8
TA2012-48-2	48.0	39.3	12.7	91.0
TA2012-48-3	48.2	39.5	12.3	91.4
TA2012-48-4	47.7	39.0	12.9	90.7
TA2012-48-5	48.5	39.5	12.0	91.8
TA2012-48-6	48.5	39.3	12.1	91.6
TA2012-48-7	48.4	39.2	12.3	91.4
TA2012-48-8	48.2	39.6	12.2	91.5
TA2012-48-9	48.5	39.4	12.2	91.6
TA2012-48-10	48.5	39.6	11.8	91.9
TA2012-48-11	48.5	39.4	12.1	91.6
TA2012-48-12	48.3	39.6	12.1	91.6
TA2012-48-13	48.6	39.3	12.1	91.7
TA2012-48-14	48.8	40.3	10.1	93.6

TA2012-48-15	50.2	40.0	9.8	94.2
TA2012-48-16	50.4	39.9	9.7	94.3
TA2012-48-17	50.6	39.9	9.6	94.5
TA2012-48-18	49.1	40.5	9.9	93.8
TA2012-48-19	50.6	39.7	9.6	94.4
TA2012-48-20	50.5	40.0	9.5	94.5
Minumum	46.0	38.7	9.4	88.1
Maximum	50.8	40.7	15.3	94.5
Average	49.7	39.9	10.4	93.5

	Type 2 olivine (n=14)			
Sample-spot	MgO (wt.%)	SiO_2 (wt.%)	FeO (wt.%)	Mg-number
TA2012-22 -1	41.5	37.8	20.8	81.6
TA2012-22 -2	41.1	37.9	21.0	81.2
TA2012-22-3	41.3	38.1	20.6	81.6
TA2012-22-4	41.1	38.2	20.7	81.5
TA2012-22-5	41.6	38.3	20.2	82.1
TA2012-22-6	41.3	38.1	20.6	81.6
TA2012-22-7	39.3	38.1	22.7	78.9
TA2012-22-8	40.3	37.9	21.8	80.1
TA2012-22-9	41.1	37.9	21.1	81.1
TA2012-22-10	40.9	37.9	21.2	80.9
TA2012-22-10	41.2	38.2	20.6	81.6
TA2012-22-11	40.3	38.0	21.7	80.2
TA2012-22-12	41.0	38.4	20.6	81.5
TA2012-22-13	41.5	38.4	20.1	82.2
Minimum	39.3	37.8	20.1	78.9
Maximum	41.6	38.4	22.7	82.2
Average	40.9	38.1	21.0	81.1

Appendix B: Scanning Electron Microscope - Energy Dispersive Spectroscopy (SEM-EDS) analyses of orthopyroxene (n=77) in the Tasse mantle xenoliths.

Sample-spot	MgO (wt.%)	Al_2O_3 (wt.%)	SiO_2 (wt.%)	FeO (wt.%)
TA2012-1-1	33.9	5.3	54.1	6.0
TA2012-1-2	34.1	4.9	54.7	6.4
TA2012-3-1	33.8	4.9	55.0	6.3
TA2012-3-2	34.1	4.9	55.3	5.8
TA2012-4-1	34.0	4.9	55.0	6.1
TA2012-5-1	34.4	4.0	55.7	5.9
TA2012-5-2	34.2	4.3	54.9	6.6
TA2012-5-3	34.0	4.8	54.7	6.5
TA2012-5-4	33.8	4.6	55.1	6.5
TA2012-15-1	34.0	5.1	54.6	6.4
TA2012-16-1	34.2	4.6	54.5	6.7
TA2012-16-2	34.1	4.3	54.8	6.8
TA2012-16-3	34.3	4.7	54.6	6.4
TA2012-17-1	34.9	4.6	54.4	6.1
TA2012-17-2	34.4	4.5	55.4	5.7
TA2012-17-3	34.3	4.6	55.4	5.7
TA2012-17-4	34.6	4.4	55.1	5.9
TA2012-22-1	27.7	7.2	52.3	12.7
TA2012-22-2	27.4	7.2	51.6	13.7
TA2012-44-1	34.3	4.9	54.8	6.0
TA2012-44-2	34.4	4.9	54.7	6.0
TA2012-44-3	33.9	5.2	54.6	6.4
TA2012-46-1	34.0	4.3	54.7	7.0
TA2012-R2-1	33.9	4.9	55.2	6.1
TA2012-R2-2	34.0	4.8	55.1	6.1
TA2012-R2-3	34.4	4.6	54.7	6.2

TA2012-R4-1	33.7	4.8	54.6	6.9
TA2012-R4-2	33.7	5.5	54.1	6.7
TA2012-R4-3	33.7	4.9	54.8	6.7
TA2012-R4-4	33.9	5.1	54.6	6.4
TA2012-R4-5	33.7	4.8	54.6	6.9
TA2012-R4-6	34.1	5.0	54.3	6.7
AP2012-2A-1	35.0	4.1	55.3	5.6
AP2012-2A-2	35.0	4.3	54.9	5.9
AP2012-2B-1	34.6	4.5	55.2	5.7
AP2012-5A-1	32.9	6.2	55.4	5.5
AP2012-5A-2	34.7	4.8	54.5	6.1
AP2012-5A-3	34.6	5.0	54.3	6.2
AP2012-5A-4	34.8	4.9	54.5	5.8
AP2012-5B-1	35.0	4.9	54.4	5.7
AP2012-5C-1	35.0	4.2	55.3	5.6
AP2012-5C-2	35.1	4.2	55.2	5.5
TA2012-5A-1	35.2	4.4	55.0	5.4
TA2012-5A-2	35.1	4.4	55.0	5.6
TA2012-5A-3	34.8	4.6	54.6	5.9
TA2012-5A-4	35.3	4.4	54.7	5.6
TA2012-5B-1	34.5	5.1	54.2	6.2
TA2012-13-1	33.0	5.3	53.8	7.9
TA2012-14A-1	34.4	4.6	55.2	5.8
TA2012-14A-2	34.4	4.6	55.0	6.1
TA2012-14A-3	34.6	4.6	54.7	6.1
TA2012-14A-4	34.9	4.3	54.9	5.9
TA2012-14A-5	34.7	4.9	54.2	6.2
TA2012-14B-1	34.4	4.5	55.2	5.9
TA2012-14B-2	34.3	5.0	54.7	6.1

TA2012-14B-3	34.2	4.5	54.7	5.9
TA2012-14B-4	34.9	4.5	54.5	6.1
TA2012-14B-5	35.0	4.1	54.8	6.1
TA2012-14B-6	34.6	4.4	54.5	6.4
TA2012-24-1	35.4	3.7	54.9	5.9
TA2012-24-2	35.4	3.7	55.4	5.5
TA2012-24-3	35.4	3.6	55.6	5.5
TA2012-24-4	35.1	3.5	55.8	5.5
TA2012-24-5	35.2	3.6	55.7	5.5
TA2012-24-6	35.3	3.9	55.2	5.5
TA2012-44A-1	34.5	5.2	54.5	5.8
TA2012-44A-2	32.7	5.0	55.6	6.0
TA2012-44A-3	34.3	5.2	53.9	5.8
TA2012-44B-1	34.6	5.2	54.1	6.1
TA2012-44B-2	34.2	5.1	54.1	6.7
TA2012-48-1	32.7	5.8	53.8	7.7
TA2012-48-2	32.9	5.0	53.3	7.8
TA2012-55-1	33.9	5.2	54.0	5.9
TA2012-55-2	33.7	5.3	53.9	6.1
TA2012-55-3	34.5	4.8	54.1	5.8
TA2012-55-4	33.8	5.4	54.0	5.8
TA2012-55-5	34.3	5.1	54.5	6.1
Minimum	27.4	3.5	51.6	5.4
Maximum	35.4	7.2	55.8	13.7
Average	34.2	4.8	54.7	6.3

Appendix C: Scanning Electron Microscope - Energy Dispersive Spectroscopy (SEM-EDS) analyses of clinopyroxene (n=95) in the Tasse mantle xenoliths.

	Type 1 Clinopyroxne (cpx1; n=65)				
Sample-spot	Na_2O (wt.%)	MgO (wt.%)	Al_2O_3 (wt.%)	SiO_2 (wt.%)	CaO (wt.%)
TA2012-1-1	2.0	16.3	7.1	52.7	21.8
TA2012-1-2	2.2	15.4	7.3	52.8	22.4
TA2012-1-3	1.9	15.5	7.4	52.4	22.8
TA2012-4-1	2.1	15.9	7.1	53.6	21.3
TA2012-4-2	2.1	16.0	6.8	52.8	22.4
TA2012-4-3	2.2	16.5	7.3	52.6	21.5
TA2012-4-4	2.3	16.5	7.2	52.8	21.3
TA2012-4-5	1.8	15.5	6.6	52.6	23.5
TA2012-4-6	2.1	16.1	6.7	52.8	22.3
TA2012-4-7	1.9	16.2	6.5	53.1	22.3
TA2012-4-8	2.0	15.8	6.8	52.4	23.0
TA2012-4-9	1.8	15.8	6.5	52.2	23.7
TA2012-5-1	1.7	17.4	4.8	53.3	22.9
TA2012-5-2	3.4	15.5	6.7	53.7	20.7
TA2012-5-3	3.3	15.6	6.4	54.2	20.5
TA2012-5-4	3.2	15.4	6.7	53.7	20.9
TA2012-15-1	2.2	15.7	7.2	52.5	22.4
TA2012-15-2	2.3	16.8	7.5	52.4	21.0
TA2012-15-3	2.2	16.5	7.5	52.8	20.9
TA2012-15-4	2.3	16.5	8.4	52.5	20.3
TA2012-16-1	2.4	15.5	7.0	52.5	22.6
TA2012-17-1	1.6	16.5	5.9	52.4	23.6
TA2012-17-2	1.8	16.4	6.2	52.5	23.3
TA2012-18-1	2.7	16.1	6.9	53.0	21.4
TA2012-18-2	2.9	15.4	7.5	52.8	21.4
TA2012-21-1	1.5	16.8	6.6	52.8	22.3
TA2012-22-2	1.2	14.5	9.7	52.8	21.8

TA2012-44-1	2.4	15.8	7.3	52.7	21.8
TA2012-44-2	2.2	15.9	7.2	52.7	21.9
TA2012-44-3	2.3	15.9	7.2	52.6	22.0
TA2012-R2-1	2.1	15.8	7.2	52.2	22.7
TA2012-R2-2	3.0	13.6	9.3	54.0	20.2
TA2012-R2-3	2.2	15.6	7.1	52.1	23.0
TA2012-R2-4	2.2	15.6	7.0	52.4	22.9
TA2012-R2-5	1.8	15.6	7.0	52.7	22.8
TA2012-R2-6	2.1	15.6	7.3	52.6	22.5
TA2012-R4-1	2.0	15.5	7.5	52.5	22.6
TA2012-R4-1	1.7	16.1	7.2	52.1	22.9
TA2012-R4-2	1.7	16.1	7.0	52.4	22.8
AP2012-2B-1	2.7	15.7	6.9	52.6	22.1
AP2012-2B-2	1.4	17.2	5.0	52.7	23.7
AP2012-2B-3	3.0	15.7	6.8	53.2	21.4
AP2012-2B-4	3.4	16.3	7.0	53.4	20.0
AP2012-2B-5	3.1	16.1	7.0	53.6	20.3
AP2012-2B-6	3.4	15.9	6.9	53.6	20.1
AP2012-2B-7	3.3	15.9	7.0	53.8	20.1
AP2012-5A-1	2.9	15.9	6.8	53.0	21.4
AP2012-5C-1	2.7	16.1	7.1	52.4	21.7
AP2012-5C-2	2.7	15.7	7.0	52.5	22.1
TA2012-4D-1	2.4	16.9	7.1	52.9	20.8
TA2012-4D-2	2.2	17.1	7.3	52.6	21.0
TA2012-5A-1	2.5	16.0	6.9	53.1	21.6
TA2012-5A-2	2.6	16.1	6.9	52.7	21.7
TA2012-5B-1	2.2	16.3	7.0	52.6	22.0
TA2012-5B-2	2.0	16.2	6.8	51.5	22.6
TA2012-14A-1	3.4	15.7	7.6	53.1	20.2
TA2012-14A-2	2.5	16.0	7.9	52.7	20.8
TA2012-14B-1	0.8	18.4	3.7	53.1	24.0

TA2012-15-1	2.5	17.2	7.8	52.6	19.9
TA2012-44B-1	2.6	16.1	8.0	52.4	21.0
TA2012-44B-2	1.2	17.8	6.3	52.3	22.5
TA2012-44B-3	2.6	16.0	8.6	52.9	19.9
TA2012-44B-4	2.6	16.5	7.5	52.9	20.6
TA2012-44B-5	2.3	16.0	7.3	51.9	22.4
TA2012-55-1	2.3	17.0	7.6	52.6	20.5
Minimum	0.8	13.6	3.7	51.5	19.9
Maximum	3.4	18.4	9.7	54.2	24.0
Average	2.3	16.1	7.0	52.8	21.8

	Type 2 Clinopyroxne (cpx2; n=30)			
Sample	MgO (wt.%)	Al_2O_3 (wt.%)	SiO_2 (wt.%)	CaO (wt.%)
TA2012-1-1	17.7	6.6	51.8	23.9
TA2012-1-2	17.7	6.6	51.9	23.9
TA2012-4-1	17.6	3.5	53.3	25.6
TA2012-4-2	17.4	4.0	53.5	25.2
TA2012-4-3	17.7	3.5	53.1	25.7
TA2012-4-4	17.3	4.3	52.6	25.7
TA2012-4-5	17.0	5.3	52.5	25.2
TA2012-5	17.9	3.7	54.3	24.1
TA2012-5-1	19.0	2.8	54.1	24.1
TA2012-5-2	19.3	3.3	54.9	22.4
TA2012-5-3	18.5	3.3	54.4	23.9
TA2012-5-4	18.0	4.0	53.5	24.5
TA2012-5-5	17.4	5.1	53.0	24.6
TA2012-5-6	18.1	4.3	53.8	23.8
TA2012-5-7	17.5	4.0	53.8	24.7
TA2012-5-8	17.5	4.6	53.5	24.4
TA2012-5-9	17.9	4.3	53.7	24.1
TA2012-13-1	17.7	8.7	51.7	21.9

TA2012-15-1	18.6	3.1	53.9	24.4
TA2012-15-2	17.0	6.7	52.3	24.0
TA2012-15-3	17.5	6.6	53.6	22.4
TA2012-17-1	16.4	6.1	52.2	25.3
TA2012-17-2	18.1	3.1	53.7	25.1
TA2012-17-3	18.4	3.5	53.5	24.6
TA2012-18-1	17.6	5.2	53.0	24.3
TA2012-22-1	19.5	2.2	55.9	22.4
TA2012-44-1	17.3	5.9	52.8	24.0
TA2012-44-2	17.6	6.0	53.2	23.3
TA2012-44-3	17.4	5.6	52.7	24.4
TA2012-44-4	19.6	1.3	55.9	23.3
Minimum	14.7	1.3	49.6	21.9
Maximum	19.6	8.7	55.9	25.7
Average	17.9	4.6	53.4	24.2

Appendix D: Scanning Electron Microscope - Energy Dispersive Spectroscopy (SEM-EDS) analyses of spinel (n=34) in the Tasse mantle xenoliths.

	MgO (wt.%)	Al_2O_3 (wt.%)	Cr_2O_3 (wt.%)	FeO (wt.%)
TA2012-2-1	21.7	54.5	11.2	12.7
TA2012-2-2	21.6	55.7	10.6	12.2
TA2012-5-1	19.9	48.5	20.0	11.6
TA2012-5-2	20.3	47.2	20.9	11.7
TA2012-13-1	21.8	57.4	9.6	11.2
TA2012-14-1	20.8	53.3	15.9	10.0
TA2012-16-1	21.4	58.1	10.6	10.0
TA2012-16-2	21.7	58.8	10.1	9.5
TA2012-16-3	21.4	58.6	10.1	10.0
TA2012-16-4	21.5	58.1	9.8	10.6
TA2012-16-5	21.4	57.7	10.2	10.7
TA2012-17-1	21.4	57.7	11.2	9.7
TA2012-17-2	21.6	56.5	11.4	10.5
TA2012-44-1	21.7	58.3	8.7	11.3
TA2012-44-2	21.9	59.7	8.4	10.0
TA2012-44-3	21.9	59.6	8.5	10.1
TA2012-44-4	21.9	58.7	8.7	10.8
TA2012-44-5	20.9	52.4	15.0	11.7
TA2012-44-6	21.5	59.2	8.7	10.6
TA2012-44-7	21.8	58.6	8.7	10.8
TA2012-44-8	21.8	59.2	8.9	10.1
TA2012-R2-1	21.5	57.9	10.0	10.6
TA2012-R4-1	21.9	58.3	8.4	11.3
TA2012-R4-2	21.6	58.7	9.1	10.6
TA2012-R4-3	21.1	58.8	9.1	10.9
TA2012-R4-4	21.8	57.7	9.1	11.4

AP2012-2A-1	21.1	50.1	17.1	11.6
AP2012-4-1	22.5	58.5	6.6	12.4
AP2012-5A-1	22.1	53.6	13.6	10.7
AP2012-5A-2	21.7	50.9	16.5	10.9
AP2012-5A-3	22.1	51.8	15.8	10.4
TA2012-55-1	21.9	57.8	10.3	9.9
TA2012-55-2	21.9	57.0	10.4	10.7
TA2012-55-3	20.7	57.6	10.5	10.8
Minimum	19.9	47.2	6.6	9.5
Maximum	22.5	59.7	20.9	12.7
Average	21.5	56.4	11.3	10.8

Table 1. Sm-Nd isotope compositions of the mantle xenoliths and host alkaline basalts.

Mantle xenoith	Rock type[a]	Sm (ppm)	Nd (ppm)	$^{147}Sm/^{144}Nd$	$^{143}Nd/^{144}Nd$	T_{DM} (Ma)[b]	εNd(0)
TA-2012-1	Spinel lherzolite	0.152	0.342	0.1927	0.512687±14	3377	0.9
TA-2012-2	Spinel lherzolite	0.232	1.401	0.1006	0.512999±09	204	7.1
TA-2012-3	Spinel lherzolite	0.157	0.370	0.1837	0.512742±13	2075	2.0
TA 2012-6	Spinel lherzolite	0.227	0.672	0.1462	0.512964±07	422	6.4
TA-2012-10	Spinel lherzolite	0.300	1.123	0.1617	0.512863±09	845	4.4
TA-2012-13	Spinel lherzolite	0.228	0.763	0.1805	0.512942±09	957	5.9
TA-2012-15	Spinel lherzolite	0.579	2.175	0.1615	0.512933±10	634	5.8
TA-2012-16-1	Spinel lherzolite	0.171	0.557	0.1660	0.512217±11	2995	-8.2
TA-2012-16-2	Spinel lherzolite	0.154	0.359	0.1691	0.512292±19	2944	-6.7
TA-2012-18	Spinel lherzolite	0.195	0.653	0.1555	0.512932±11	574	5.7
TA-2012-19	Spinel lherzolite	0.307	1.082	0.1720	0.513023±06	466	7.5
TA-2012-44	Spinel lherzolite	0.315	1.183	0.1610	0.51302±08	377	7.4
TA-2012-45	Spinel lherzolite	0.284	0.870	0.1646	0.513063±10	269	8.3
TA-2012-48	Spinel lherzolite	0.477	2.068	0.1396	0.512951±06	411	6.1
TA-2012-49	Spinel lherzolite	0.199	0.498	0.1729	0.513132±05	66	9.6
TA-2012-55	Spinel lherzolite	0.281	1.178	0.1448	0.513029±06	267	7.6
TA-2012-27	Alkaline basalt	8.752	47.8	0.1108	0.512863 ±06	426	4.4
TA-2012-31	Alkaline basalt	9.257	50.9	0.1100	0.512902±05	366	5.1
TA-2012-35	Alkaline basalt	9.107	49.3	0.1117	0.512834±09	474	3.8
TA-2012-37	Alkaline basalt	8.770	48.3	0.1099	0.512896±04	374	5.0
TA-2012-41	Alkaline basalt	9.076	49.8	0.1104	0.512922±06	338	5.5
TA-2012-43	Alkaline basalt	8.724	48.3	0.1093	0.512888±04	384	4.9
TA-2012-60	Alkaline basalt	8.251	44.9	0.1111	0.512912±05	355	5.3

[a]Alkaline basalt data from Friedman et al. (2016). [b]See DePaolo (1981)

Table 2. Pb isotope compositions of the mantle xenoliths and host alkaline basalts.

	Rock type[a]	$^{206}Pb/^{204}Pb$	± 2σ	$^{207}Pb/^{204}Pb$	± 2σ	$^{208}Pb/^{204}Pb$	± 2σ
TA-2012-1	Spinel lherzolite	18.493	0.0804	15.624	0.0683	38.315	0.1691
TA-2012-2	Spinel lherzolite	18.523	0.0572	15.571	0.0487	38.153	0.1211
TA-2012-3	Spinel lherzolite	18.675	0.0903	15.637	0.0765	38.524	0.1899
TA-2012-6	Spinel lherzolite	18.724	0.0828	15.659	0.0697	38.674	0.1746
TA-2012-10	Spinel lherzolite	18.872	0.0690	15.622	0.0579	38.514	0.1450
TA-2012-13	Spinel lherzolite	18.679	0.0610	15.604	0.0518	38.427	0.1288
TA-2012-14	Spinel lherzolite	18.661	0.0609	15.495	0.0547	38.128	0.1266
TA-2012-15	Spinel lherzolite	19.172	0.0476	15.590	0.0395	38.690	0.0995
TA-2012-16	Spinel lherzolite	18.728	0.0762	15.566	0.0640	38.359	0.1587
TA-2012-18	Spinel lherzolite	18.405	0.0353	15.605	0.0308	38.164	0.0778
TA-2012-19	Spinel lherzolite	18.616	0.0743	15.626	0.0630	38.357	0.1553
TA-2012-44	Spinel lherzolite	18.996	0.0792	15.561	0.0655	38.485	0.1627
TA-2012-45	Spinel lherzolite	18.793	0.0754	15.593	0.0631	38.364	0.1566
TA-2012-48	Spinel lherzolite	18.800	0.0658	15.604	0.0562	38.456	0.1400
TA-2012-49	Spinel lherzolite	19.020	0.0439	15.594	0.0368	38.621	0.0943
TA-2012-55	Spinel lherzolite	18.955	0.0426	15.578	0.0359	38.535	0.0921
TA-2012-27	Alkaline basalt	19.575	0.012	15.586	0.011	39.088	0.033
TA-2012-31	Alkaline basalt	19.551	0.018	15.572	0.016	39.045	0.042
TA-2012-35	Alkaline basalt	19.564	0.026	15.599	0.022	39.139	0.057
TA-2012-37	Alkaline basalt	19.557	0.009	15.578	0.009	39.064	0.029
TA-2012-41	Alkaline basalt	19.544	0.026	15.569	0.022	39.035	0.058
TA-2012-43	Alkaline basalt	19.542	0.013	15.568	0.012	39.032	0.035
TA-2012-60	Alkaline basalt	19.404	0.014	15.581	0.013	38.994	0.037

[a]Alkaline basalt data from Friedman et al. (2016).

Table 3. Rb-Sr isotope compositions of the mantle xenoliths and host alkaline basalts

	Rock type[a]	Rb (ppm)	Sr (ppm)	$^{87}Sr/^{86}Sr$
TA-2012-1	Spinel peridotite	0.56	7.7	0.706237±17
TA-2012-2	Spinel peridotite	0.42	18.3	0.703582±30
TA-2012-3	Spinel peridotite	0.34	5.8	0.704522±25
TA-2012-6	Spinel peridotite	1.00	12.0	0.703644±24
TA-2012-10	Spinel peridotite	0.66	21.3	0.703534±17
TA-2012-13	Spinel peridotite	0.62	16.4	0.703581±15
TA-2012-15	Spinel peridotite	0.69	31.1	0.703429±27
TA-2012-16	Spinel peridotite	0.38	5.5	0.708121±20
TA-2012-18	Spinel peridotite	0.58	14.6	0.703177±18
TA-2012-19	Spinel peridotite	0.31	14.5	0.703735±17
TA-2012-44	Spinel peridotite	0.78	25.2	0.703884±14
TA-2012-45	Spinel peridotite	0.33	17	0.703809±13
TA-2012-48	Spinel peridotite	0.63	25.8	0.703924±15
TA-2012-49	Spinel peridotite	0.33	9.8	0.703527±23
TA-2012-55	Spinel peridotite	0.52	16.2	0.703407±37
TA-2012-27	Alkaline basalt	38	907	0.703416±11
TA-2012-31	Alkaline basalt	36	881	0.703382±12
TA-2012-35	Alkaline basalt	37	886	0.703393±11
TA-2012-37	Alkaline basalt	40	965	0.703409±09
TA-2012-41	Alkaline basalt	38	876	0.703346±12
TA-2012-43	Alkaline basalt	42	948	0.703347±11
TA-2012-60	Alkaline basalt	39	923	0.703591±11

[a]From Friedman et al. (2016).

$^{87}Rb/^{86}Sr$
0.210
0.066
0.169
0.241
0.090
0.109
0.064
0.200
0.115
0.062
0.089
0.056
0.071
0.097
0.093
0.123
0.118
0.120
0.119
0.127
0.127
0.123

Table 4. Whole-rock oxygen isotope compositions of the mantle xenoliths and host alkaline basalts.

Sample	Rock type	δ^{18}O VSMOW	n
TA-2012-3	Spinel lherzolite	+4.50	
TA-2012-8	Spinel lherzolite	+6.04	
TA-2012-10	Spinel lherzolite	+4.68	
TA-2012-10-dup	Spinel lherzolite	+5.42	
TA-2012-13	Spinel lherzolite	+4.89	
TA-2012-19	Spinel lherzolite	+5.19	
TA-2012-48	Spinel lherzolite	+5.24	
TA-2012-49	Spinel lherzolite	+5.65	
TA-2012-56	Spinel lherzolite	+4.50	
TA-2012-62	Spinel lherzolite	+4.69±0.02	2
TA-2012-R4	Spinel lherzolite	+5.22	
Average (n=11)		*+5.09±0.49*	
TA-2012-50	Alkaline basalt	+6.76	
TA-2012-52	Alkaline basalt	+6.10	
TA-2012-59	Alkaline basalt	+6.016	
TA-2012-60	Alkaline basalt	+6.32	
Average (n=4)		*+6.30 ± 0.33*	

Table 5. Oxygen isotope compositions for olivine, clinopyroxene, orthopyroxene and spinel in the mantle xenoliths

Sample	Mineral	$\delta^{18}O$ VSMOW	n
TA-2012-3	Olivine	+4.72	
TA-2012-4	Olivine	+5.30±0.02	2
TA-2012-8	Olivine	+4.91	
TA-2012-9	Olivine	+5.14	
TA-2012-19	Olivine	+4.92	
TA-2012-48	Olivine	+4.88±0.03	2
TA-2012-56	Olivine	+4.99	
TA-2012-62	Olivine	+5.29	
Average (n = 8)		*+5.02±0.21*	
TA-2012-3	Clinopyroxene	+4.98	
TA-2012-4	Clinopyroxene	+6.84	
TA-2012-8	Clinopyroxene	+6.38	
TA-2012-9	Clinopyroxene	+6.16	
TA-2012-19	Clinopyroxene	+5.61	
TA-2012-48	Clinopyroxene	+6.37	
TA-2012-56	Clinopyroxene	+5.41	
TA-2012-62	Clinopyroxene	+6.20	
Average (n = 8)		*5.99±0.61*	
TA-2012-3	Orthopyroxene	+6.28	
TA-2012-4	Orthopyroxene	+6.20	
TA-2012-8	Orthopyroxene	+5.61	
TA-2012-9	Orthopyroxene	+6.40	
TA-2012-19	Orthopyroxene	+4.56	
TA-2012-48	Orthopyroxene	+6.41	
TA-2012-56	Orthopyroxene	+5.69	
TA-2012-62	Orthopyroxene	+6.10	
Average (n = 8)		*5.91±0.62*	
TA-2012-3	Spinel	+4.41	
TA-2012-4	Spinel	+4.72	
TA-2012-19	Spinel	+4.4	
TA-2012-48	Spinel	+4.63±0.01	2
TA-2012-56	Spinel	+4.51	
TA-2012-62	Spinel	+4.34±0.01	2
Average (n = 6)		*+4.50±0.15*	